Nuclear Science and Techniques (2024) 35:214
https://doi.org/10.1007/s41365-024-01591-2

Properties of the QCD matter: review of selected results from the relativistic heavy ion collider beam energy scan (RHIC BES) program

Jin-Hui Chen[1] · Xin Dong[2] · Xiong-Hong He[3] · Huan-Zhong Huang[4] · Feng Liu[5] · Xiao-Feng Luo[5] · Yu-Gang Ma[1] · Li-Juan Ruan[6] · Ming Shao[7] · Shu-Su Shi[5] · Xu Sun[3] · Ai-Hong Tang[6] · Ze-Bo Tang[7] · Fu-Qiang Wang[8] · Hai Wang[1] · Yi Wang[9] · Zhi-Gang Xiao[10] · Guan-Nan Xie[11] · Nu Xu[2] · Qing-Hua Xu[12] · Zhang-Bu Xu[13] · Chi Yang[12] · Shuai Yang[14] · Wang-Mei Zha[7] · Ya-Peng Zhang[3] · Yi-Fei Zhang[7] · Jie Zhao[1] · Xiang-Lei Zhu[9]

Received: 3 July 2024 / Revised: 23 July 2024 / Accepted: 6 August 2024 / Published online: 25 November 2024

Abstract
In the paper, we discuss the development of the multigap resistive plate chamber time-of-flight (TOF) technology and the production of the solenoidal tracker at RHIC (STAR) TOF detector in China at the beginning of the twenty-first century. Subsequently, recent experimental results from the first beam energy scan program (BES-I) at the Relativistic Heavy Ion Collider (RHIC) pertaining to measurements of collectivity, chirality, criticality, global polarization, strangeness, heavy flavor, dilepton and light nuclei productions are reviewed.

Keywords Heavy ion collision · Quark–gluon plasma · QCD phase diagram · Collectivity · Chirality · Criticality

1 Introduction

Quantum chromodynamics (QCD), the theory of the strong force, is the cornerstone for understanding the fundamental nature of matter under the most extreme conditions [1, 2]. Among the myriad of phenomena it encompasses, perhaps one of the most fascinating is the behavior of QCD matter at extreme temperatures and densities, where the

Dedicated to Professor Wenqing Shen in honour of his 80th birthday.

This work was supported in part by the National Key Research and Development Program of China (No. 2022YFA1604900), the National Natural Science Foundation of China (No. 12025501), and Strategic Priority Research Program of Chinese Academy of Sciences (No. XDB34000000).

✉ Jin-Hui Chen
chenjinhui@fudan.edu.cn

1 Key Laboratory of Nuclear Physics and Ion-Beam Application (MOE), Institute of Modern Physics, Fudan University, Shanghai 200433, China

2 Nuclear Science Division, Lawrence Berkeley National Laboratory, Berkeley, CA 94720, USA

3 QMRC, Institute of Modern Physics, Chinese Academy of Sciences, Lanzhou, China

4 Department of Physics and Astrophysics, University of California, Los Angeles, CA 90095, USA

5 Key Laboratory of Quark and Lepton Physics (MOE) and Institute of Particle Physics, Central China Normal University, Wuhan 430079, China

6 Department of Physics, Brookhaven National Laboratory, Upton, NY 11973, USA

7 Department of Modern Physics, University of Science and Technology of China, Hefei, China

8 Department of Physics, Purdue University, West Lafayette, IN 47907, USA

9 Department of Engineering Physics, Tsinghua University, Beijing, China

10 Department of Physics, Tsinghua University, Beijing, China

11 School of Nuclear Science and Technology, University of Chinese Academy of Sciences, Beijing 100049, China

12 Key Laboratory of Particle Physics and Particle Irradiation (MOE), Institute of Frontier and Interdisciplinary Science, Shandong University, Qingdao 266237, China

13 Department of Physics, Kent State University, Kent, OH 44242, USA

14 Institute of Quantum Matter, South China Normal University, Guangzhou 510006, China

fundamental constituents of matter, quarks and gluons undergo phase transition to become a hadronic matter through hadronization. The experiments at the Relativistic Heavy Ion Collider (RHIC) have provided unique experimental evidence for the transition [3]; however, at exactly what temperature and/or densities this phase transition occurs and the nature of the phase transition are far from being clear. Thus, we are still mystified about the true nature of QCD, especially at extreme temperatures and densities. In the fiery furnaces of the early universe or in the cores of neutron stars, matter undergoes epic transformations, transitioning between different phases as dictated by the intricate dynamics of QCD. It is in these extreme environments that the search for the properties of QCD matter has faced its greatest challenges and most profound revelations [4, 5].

The RHIC at Brookhaven National Laboratory stands as a beacon in the quest to unravel the mysteries of QCD matter. Through its beam energy scan (BES) program [6], RHIC has probed the properties of QCD matter across a wide range of collision energies in various aspects, providing a comprehensive experimental landscape to explore the phases and transitions of this extreme form of matter.

In this review, we start with a brief description of the early development and production of STAR multigap resistive plate chamber (MRPC) TOF detector in China, which was the first significant detector to contribute to an international experiment from the Chinese nuclear physics community. Subsequently, we embark on a journey through the rich tapestry of experimental results gleaned from the RHIC BES program, delving into the intricate interplay of phenomena such as the quark–gluon plasma (QGP), hadronization, and the evolution of collective behavior in heavy ion collisions. The key findings from selected topics which have reshaped our understanding of the QCD matter and its manifestations in the laboratory are highlighted. The topics cover basic observables including collectivity, chirality, criticality, global polarization, strangeness, heavy flavor, dilepton, and light nuclei.

From the onset of RHIC's operation to its latest experimental endeavors, this review attempts to encapsulate the progress made in deciphering the properties of QCD matter. Through precision measurements and innovative analysis techniques, RHIC has made strides to unravel the phase diagram of QCD matter, revealing its intricate structure and elucidating the fundamental forces that govern the Universe.

This review article is organized as follows. Section 2 describes the development of the TOF detector. Section 3 presents selective STAR measurements of identified particles enabled by the TOF detector. A brief summary and outlook is provided in Sect. 4.

2 Development and construction of the STAR MRPC TOF detector

The multigap resistive plate chamber (MRPC) technology was first realized in the mid-1990s by a large ion collider experiment (ALICE) TOF group [7]. The MRPC technology enabled the construction of a cost-effective TOF detector for the identification of the charged particles copiously produced in relativistic heavy ion collisions. The basic structure of MRPC features a stack of parallel resistive plates, usually with gaps of $\sim 0.2-0.3$ mm. High voltages are applied to the stack through the outermost plates by resistive conductive graphite while the inner plates are electrically floating. When a charged particle passes through the MRPC, primary electrons are produced by ionization in the gaps (filled with Freon-rich gas mixture), which triggers gas avalanche amplification in the strong electric field (usually $\sim 100\,\mathrm{kV/cm}$ or more). Fast signals are induced on the outer readout strips. In general, differential-input preamplifiers are used to reduce noise. Multiple narrow gaps are beneficial in reducing the time fluctuation of an avalanche, thus improving the timing performance. The potential across inner electrically floating plates arises from the gain-feedback in different gaps and guarantees gain uniformity. This striking feature greatly simplifies the manufacturing and operation of MRPC. In short, MRPC is a new type of cost-effective gas detector with excellent timing performance.

The China-US cooperation in heavy ion physics started in 2000 by developing an MRPC-based barrel TOF for the solenoidal tracker at RHIC (STAR) experiment. The first MRPC prototype was soon developed by the University of Science and Technology of China (USTC) [8], as illustrated in Fig. 1. In May 2001 the Chinese STAR team was officially established, led by Prof. Wenqing Shen. The team decided to build a TOF tray (TOFr) demonstrator with 28 MRPCs. One

Fig. 1 (Color online) First MRPC prototype produced by USTC, with an active area of $4\,\mathrm{cm} \times 4\,\mathrm{cm}$ and single-channel readout

month later, the STAR collaboration accepted all six institutions of the Chinese team, including Shanghai Institute of Applied Physics, Chinese Academy of Sciences (SINAP-CAS), Institute of High Energy Physics (IHEP-CAS), Institute of Modern Physics (IMP-CAS), Central China Normal University (CCNU), Tsinghua University (THU), and USTC, as institutional members of the collaboration.

In 2002, the TOFr demonstrator was successfully developed jointly by Chinese and American teams. The Chinese side developed 24 MRPCs, and the US side developed four MRPCs and the entire electronics. Through this effort, Chinese researchers acquired a deep understanding of the MRPC technology, in both detector physics and module production. In 2003, the TOFr had all the features suitable for installation and operation in STAR, thereby joining the physics run of STAR in 2003. The physics and experimental results from TOFr were so fruitful [9–14] that Dr. Hallman, the spokesperson of STAR, wrote a special letter to Prof. Wenqing Shen to express his congratulations. The major technical progress from the Chinese STAR team ultimately led STAR to decide to produce all the MRPC modules for the barrel TOF in China.

In 2006, the project "Research of relativistic nuclear collision physics at STAR and development of time-of-flight detector" was jointly funded by the National Natural Science Foundation of China (NSFC), CAS, and the Ministry of Science and Technology (MOST) of China. The cooperations of the Chinese STAR team led to the development of the STAR TOF and RHIC physics research. By 2009, all 4000 MRPC modules were produced by THU and USTC. The understanding of MRPC technology and strict quality control resulted in a final yield of up to 95%, with very good stability and consistency [15, 16]. Since the initial TOFr demonstration, STAR TOF has maintained a systematic time resolution of ~ 80 ps (MRPC intrinsic resolution ~ 60 ps) [17], which has been highly evaluated by experts of the US Department of Energy (DOE) and the STAR collaboration.

The TOF detector significantly extended the STAR particle identification capabilities. In Fig. 2, with $2\,\sigma$ separation, protons/(pions + kaons) and kaons/pions are identified up to 3 GeV/c and 1.6 GeV/c, respectively. Without TOF, these two groups can only be identified up to 1.0 GeV/c and 0.7 GeV/c. The successful construction and smooth operation of the TOF system also contributed to the observation of the heaviest antimatter helium-4 nucleus [18]. Measuring the mean energy loss per unit track length in the time projection chamber (TPC) [19] helps distinguish particles with different masses or charges, whereby through the time of flight of particles arriving at the surrounding TPC, anti-helium nuclei can be identified unambiguously (Fig. 3).

The successful development and operation of STAR TOF, which has been significantly promoted in STAR physics research, have greatly boosted the application of MRPC

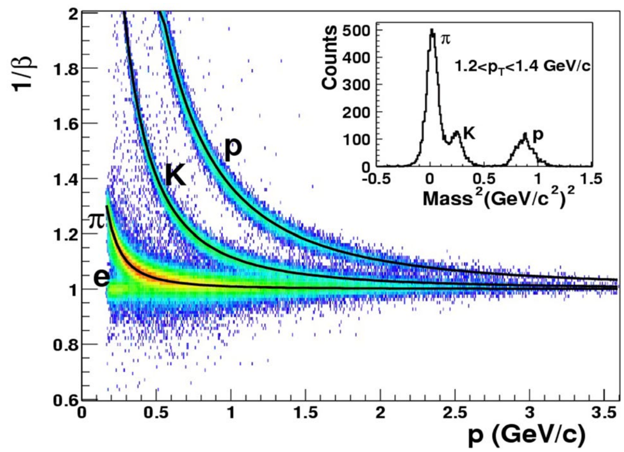

Fig. 2 (Color online) Particle velocity, $1/\beta$, as a function of particle momentum

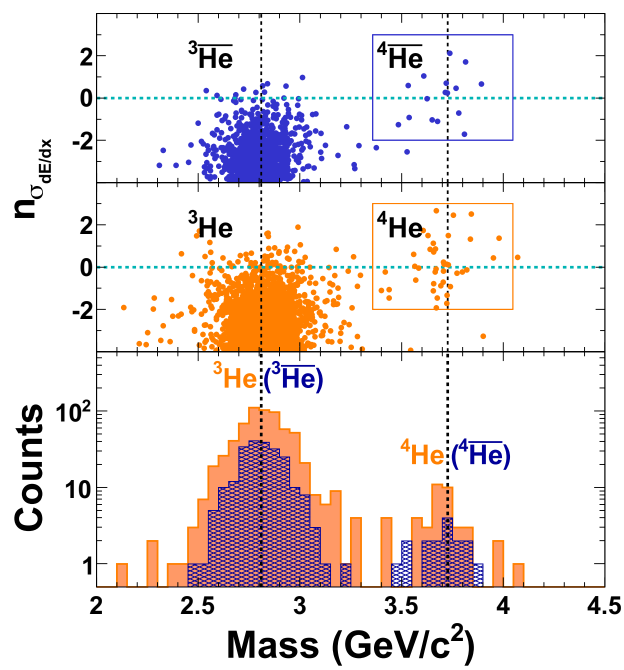

Fig. 3 (Color online) Top two panels show the $\langle dE/dx\rangle$ in units of multiples of $\sigma_{dE/dx}$, $n\sigma_{dE/dx}$, of negatively charged particles (first panel) and positively charged particles (second panel) as a function of mass measured by the TOF system. Rectangular boxes highlight areas for $^4\overline{\mathrm{He}}$ (^{4}He) selections. Bottom panel shows a projection of the entries in the upper two panels onto the mass axis for particles in the selected window. A total of 16 candidates of $^4\overline{\mathrm{He}}$ were identified using the combined measurements of energy loss and time of flight (see [18] for more details)

technology. In 2008, the long-strip (length: 87 cm) MRPC (LMRPC) was developed in USTC [20]. With the strong support of NSFC, the Chinese STAR team completed the development and construction of LMRPC-based muon telescope detector (MTD) [21], the successful performance [22] of which further improved the research of lepton physics in STAR. In China, the successful operation of STAR TOF also triggered the endcap TOF (eTOF) upgrade of Beijing Spectrometer Experiment (BESIII) using MRPC technology [23].

With the success of the RHIC BES program (phase-I), high-luminosity heavy ion collision experiments at lower center-of-mass energies became an important frontier to explore in determining the phase boundary and critical end point of the quark–gluon plasma phase transition. To adapt to the high-luminosity physics, STAR TOF is required to have a higher magnitude counting rate capability, especially in the endcap region. STAR and compressed baryonic matter (CBM) research and development collaboration was conducted for this purpose. USTC adopted ultra-thin float glass to increase the MRPC counting rate from a few hundred $\mathrm{Hz/cm^2}$ to $\mathrm{kHz/cm^2}$, while THU successfully developed MRPC to operate at a counting rate of tens of $\mathrm{kHz/cm^2}$, using special low-resistivity glass plates (bulk resistivity $\sim 10^{10}\ \Omega \cdot \mathrm{cm}$) [24, 25]. Both MRPCs were installed into the STAR endcap TOF and satisfied the required performance.

Another important application is the development of MRPC TOF for the cooler-storage-ring external-target experiment (CEE), located at Lanzhou. This is the first spectrometer in China, operating in the GeV level energy regime, for heavy ion collision studies. It is dedicated to the phase structure studies of the nuclear matter, nuclear equation of state, symmetry energy, and production of hypernucleus, among others. To improve the gas exchange speed and significantly reduce gas consumption, a new style sealed MRPC has been developed [26]. The structure is shown in Fig. 4. The time resolution of this MRPC is better than 60 ps and the efficiency is higher than 97%. In the cosmic test, this sealed MRPC can work at gas flushes of lower than 10 sccm per square meter detector and has been applied to the CEE-eTOF wall with a 70% reduction in the necessary gas flow rate while maintaining performance and stability.

The MRPC TOF experiences in STAR, CBM and CEE not only significantly promote particle detection technology but also provide a powerful tool for many physics programs. In the next-generation nuclear and particle physics experiments based on high-luminosity accelerators, MRPC will continue to provide reliable technical options for particle identification and trigger owing to the new developments in low-resistivity glass plates and high-speed waveform sampling technology [27, 28] that provide MRPC with a time resolution better than 20 ps (Fig. 5 [29]) with high counting rate. In the interim, modern technology such as machine learning and neural networks are also being studied to reconstruct the timing of MRPC [30]. Research never stops to improve the performance of MRPC, to meet the requirements of future experiments such as new detector material,

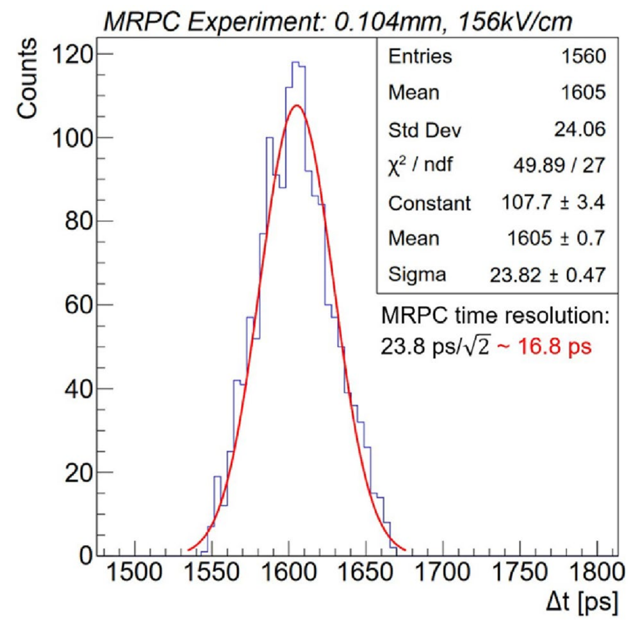

Fig. 5 (Color online) The intrinsic time resolution of MRPC has reached 16.8 ps, as indicated. It has 32 gas gaps with a gap width of 0.104 mm

Fig. 4 (Color online) The latest design of sealed MRPC structure

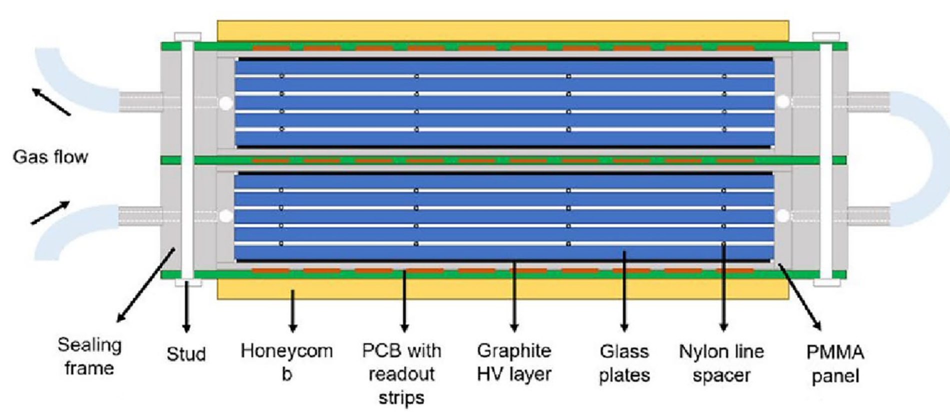

new fast electronics, new analysis methods, and eco-friendly working gas.

3 Experimental results and discussions

3.1 Charged particle spectra and yields

Relativistic heavy ion collision experiments are designed for the search and study of the QGP. In head-on relativistic heavy ion collisions, two nuclei can be represented as two thin disks approaching each other at high speed because of the Lorentz contraction effect in the moving direction. During the initial stage of collisions, the energy density is higher than the critical energy density obtained from lattice QCD calculations, whereby quarks and gluons are deconfined from nucleons and form QGP. The large cross section of interaction may lead to the thermalization of the QGP. At this stage, high transverse momentum jets and heavy flavor pair are produced because of the large momentum transfer. Subsequently, the QGP expands and cools down, entering into the mixed-phase expansion. The chemical freeze-out point is formed after the inelastic interaction stops, which means that thereafter particle yields and ratios do not change. After chemical freeze-out, the elastic interaction between hadrons and resonance decays [31] change the p_T distribution of particles. The particles finally freeze out of the system after the elastic interaction stops, at the so-called kinetic freeze-out point. Studying the bulk properties of the system, such as the spectra, the yields (dN/dy), particle ratios, and freeze-out properties, can provide insight into the particle production mechanisms and evolution of QCD matter.

In experimental observations, first invariant yields of various particles are presented as a function of transverse momentum p_T. Figure 6 shows the invariant yields of pions ($\pi^{\pm}$), kaons ($K^{\pm}$), protons (p), anti-protons ($\bar{p}$), phi-mesons (ϕ), lambda baryons (Λ), anti-lambda baryons ($\bar{\Lambda}$), cascades (Ξ^-), anti-cascades ($\overline{\Xi}^+$), Omegas (Ω^-), anti-Omegas ($\overline{\Omega}^+$), deuterium (d), and anti-deuterium ($\bar{d}$). The results are shown for Au+Au collisions at $\sqrt{s_{NN}} = 19.6$ GeV in four collision centralities: 0–10%, 20–40%, 40–60%, and 60–80% [32–35]. The invariant yields show a decrease with increasing p_T, moving from central to peripheral collisions. The curves represent the blast wave fits to the spectra [36].

The yields, dN/dy, are obtained by integrating these measured spectra and interpolating through fitting functions where the measurements are not available. Figure 7 shows the energy dependence of particle yields for $\pi^{\pm}$, $K^{\pm}$, p, $\bar{p}$, ϕ, Λ, $\bar{\Lambda}$, Ξ^-, $\overline{\Xi}^+$, Ω^-, $\overline{\Omega}^+$, d, and $\bar{d}$. Results from STAR BES-I [32–35] are compared with previously published STAR results at higher energies and those of other world experiments. The reader is referred to the topical review in [6] on data collection. The yields of anti-baryons increase

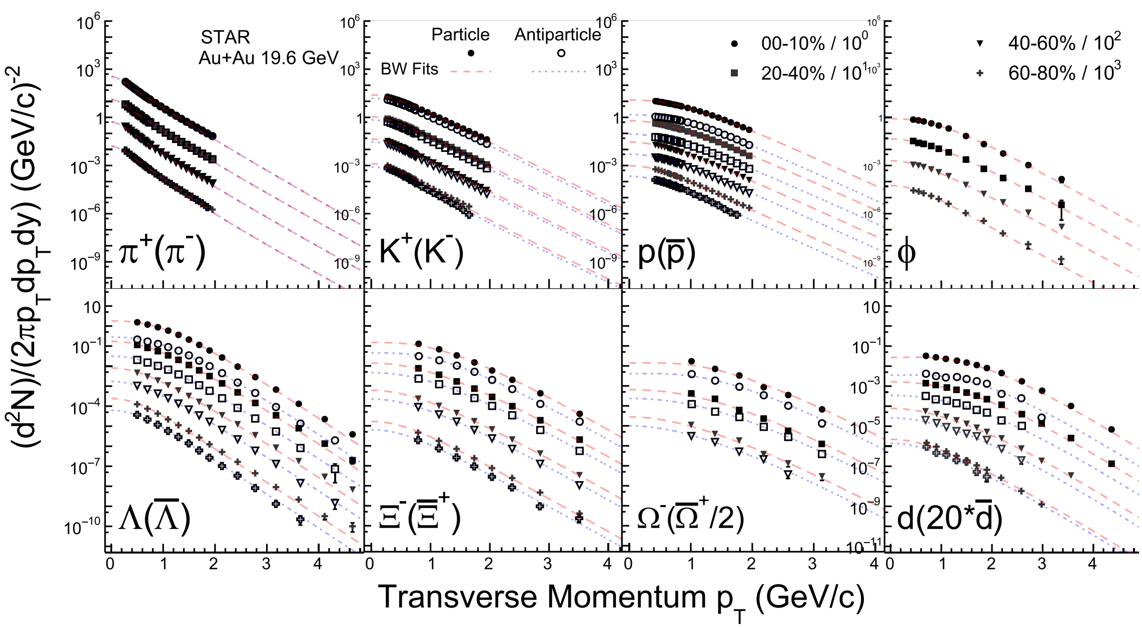

Fig. 6 (Color online) Invariant yields of identified particles measured as a function of transverse momentum in various collision centralities in Au+Au collisions at $\sqrt{s_{NN}} = 19.6$ GeV [32–35]. Filled points represent particles and open points are antiparticles. The curves are fits to the data points based on the thermal blast wave distribution [36]

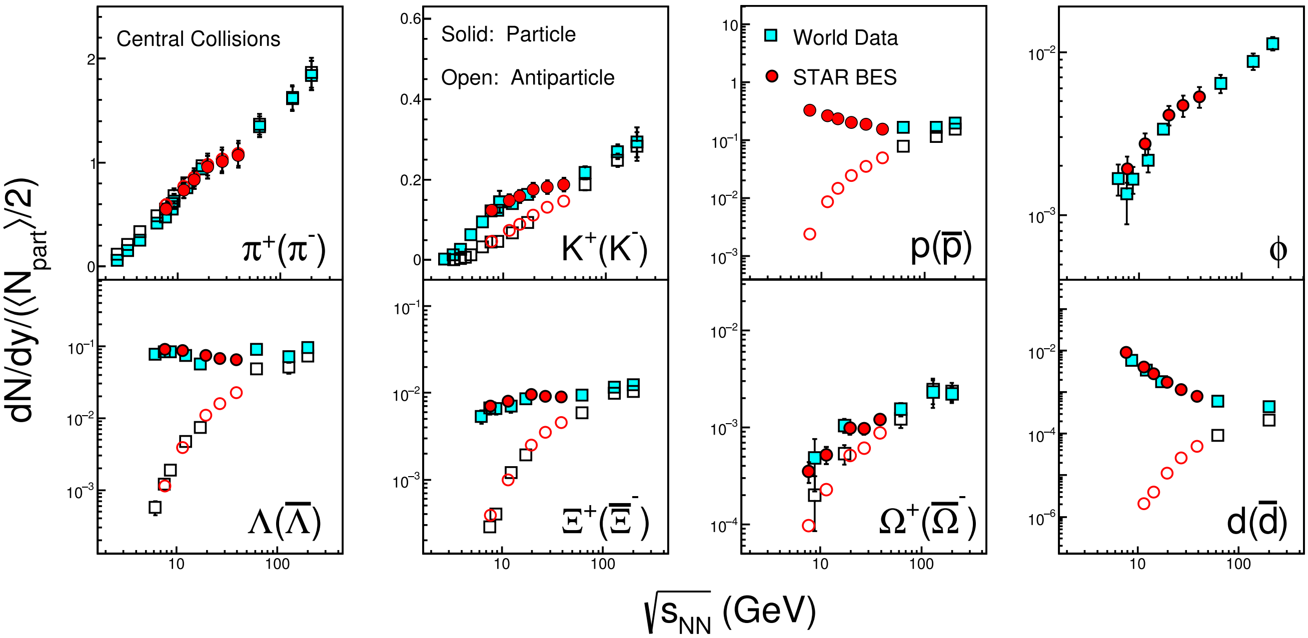

Fig. 7 (Color online) Energy dependence of particle yields $\mathrm{d}N/\mathrm{d}y$ in central collisions [6]. Solid points represent particles, and open points are the antiparticles. The data are normalized by the number of participants

rapidly with increasing collision energy, demonstrating the increasing contribution of pair production. However, the yields of baryons and K^+ show a non-trivial energy dependence in the BES energy range, indicating the interplay of baryon stopping/association and pair production.

The hadron yields retain the footprint of the hot and dense hadronic matter during the evolution of the collision system, presumably because the system undergoes a crossover at phase transition [32]. As observed experimentally, the relative abundances of hadrons follow the thermal distribution at common temperatures and baryonic chemical potentials, such that the thermal fit can fix the temperature and baryonic chemical potential [32]. The temperatures of chemical freeze-out (T_{ch} for central Au+Au collisions at different collision energies are shown in Fig. 8. With increasing energy, the T_{ch} increases and becomes constant at $\sim 160\,\mathrm{MeV}$ after $\sqrt{s_{\mathrm{NN}}} = 11.5\,\mathrm{GeV}$. The parameters extracted from net-proton higher moments [38] are also presented in the figure. They are consistent with the results from the hadron yield fit. The extracted parameters from BES data are also consistent with the results from the lattice QCD calculations and thermal fit to the global hadron yield data [37]. In covering the RHIC BES program, STAR fixed-target program, and future experimental facilities shown in the figure, a more precise description of the QCD phase diagram is presented.

One of the foundations of the BES program is the promise of a sweeping variation of the chemical potential across the QCD phase diagram through changes in the beam energy of heavy ion collisions, whereby the chemical potential is

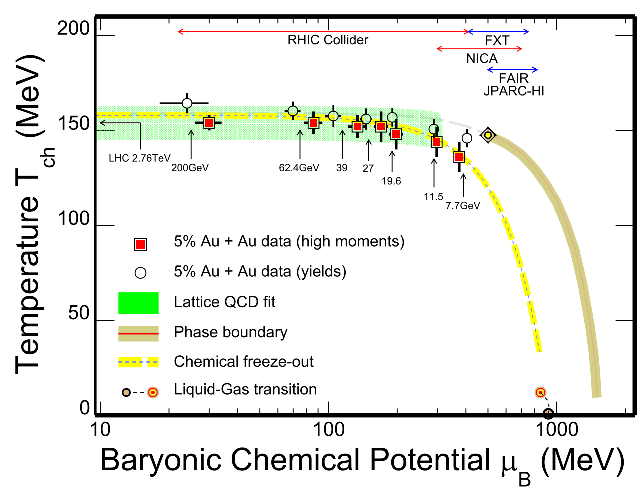

Fig. 8 (Color online) A summary of the chemical freeze-out temperature $T_{\mathrm{ch}}(\mu_{\mathrm{B}})$ distribution [37]. Data points are from the 0–5% central Au+Au collisions at STAR BES [32, 38]

extracted empirically from the final-state particle distributions. An important subject in itself is how the baryons are shifted from target and projectile rapidity to midrapidity. A puzzling feature of ultra-relativistic nucleus-nucleus collisions is the experimental observation of substantial baryon asymmetry in the central rapidity (midrapidity) region both at the energies of RHIC [32, 39, 40] and large hadron collider (LHC) ($\sqrt{s_{\mathrm{NN}}} = 900\,\mathrm{GeV}$) [41, 42]. Such a phenomenon is impressive, as the baryon number is strictly conserved; therefore, net-baryon number cannot be created in the system and must come from the colliding targets and projectile. In the conventional picture, the valence quarks carry the baryon quantum number in the nucleus. At sufficiently high energies, these valence quarks are expected to pass through, ending up far from midrapidity in the fragmentation regions [43]. The RHIC BES program covers a wide range of baryon stopping, over an order of magnitude of net-proton yields at midrapidity [32, 40].

Figure 9 presents the net-proton yields at midrapidity in Au+Au collisions at $\sqrt{s_{\mathrm{NN}}} = 7.7$ GeV to 200 GeV [44]. For all centralities in heavy ion collisions, the midrapidity net-baryon density follows an exponential distribution with the variable $\delta y = y_{\mathrm{b}} - y_{\mathrm{cm}}$, where y_{b} is the beam rapidity, and y_{cm} is the center-of-mass rapidity. This variable δy is referred to as the "rapidity loss" which for the midrapidity protons produced in a collider experiment is equal to beam rapidity: $\delta y = y_{\mathrm{b}}$ as $y_{\mathrm{cm}} = 0$. A single collision energy therefore gives rise to a single point in Fig. 9. The data points at each centrality can be fitted with an exponential function $A\exp(-\alpha_B \delta y)$. The baryon stopping is often characterized by average rapidity loss [45], which is characterized by a complicated beam energy dependence and is usually skewed by the large proton yields close to beam rapidity, leading to the conclusion [45] that the "rapidity loss" of projectile baryons at RHIC breaks the linear scaling observed at lower energies. Another way of characterizing the baryon stopping is to use the $\bar{\mathrm{p}}/\mathrm{p}$ ratio [41, 42, 46]. Both pair production and baryon stopping contribute to this ratio. Most of the dynamic models of heavy ion collisions parametrize the baryon stopping to reproduce the experimental data although at a fundamental level, a lack of understanding on how baryons are

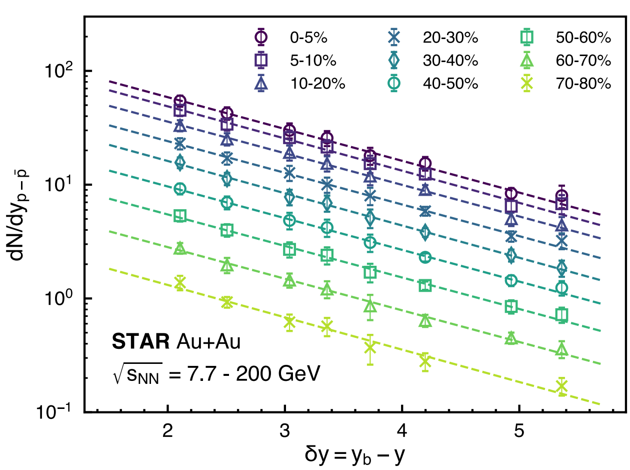

Fig. 9 (Color online) Exponential dependence of midrapidity ($y \approx 0$) baryon density per participant pair in heavy ion collisions with y_{b} equal to the rapidity difference between beam and detector midrapidity (δy) [44]. An exponential fit function of $A \times \exp(-\alpha_B \delta y)$ is also included. The figure is taken from [44]

stopped prevails. A recent modeling of heavy ion collisions indicates that the inclusion of the baryon junction is essential for describing net-proton density at RHIC [47]. Clearly some of the earlier implementations of baryon junctions [48, 49], which attempted to match the earlier experimental data with certain parameter tunes, do not reproduce the experimental results presented in Fig. 9.

3.2 Strangeness production

Strange hadrons serve as excellent probes for the physics of QCD phase boundary and search for the onset of deconfinement. Strangeness enhancement in heavy ion hadron collisions has long been suggested as a signature of the quark–gluon plasma [50–52], motivating its measurement in many experiments at different accelerator facilities. In general, the yields of strange hadrons in nuclear collisions are close to those expected from statistical models [53–55]. The precise measurement of these yields in phase-I of RHIC BES experiments has led to a better understanding of the strange quark production mechanisms in nuclear collisions and a more reliable extraction of the chemical freeze-out parameters [32], as shown in Fig. 8. In the higher beam energies, formation of a thermalized system is expected and strangeness is abundantly produced. However, at lower beam energies, strangeness production is less, requiring special attention and local treatment of the canonical ensemble. This part is further discussed in relation to Fig. 11, with the $\phi(1020)$ meson with zero net strangeness number ($S = 0$) offering a unique opportunity to scrutinize the thermodynamic properties of strange quarks in the hot and dense QCD environment [56].

The precise measurement of strange hadron production at different p_{T} ranges and centralities in heavy ion collisions are also crucial for a better understanding of the production mechanism and medium properties created in the system. At high p_{T}, the nuclear modification factor R_{CP} of various particles at top RHIC energy is observed to be much less than unity [57–59], indicating a significant energy loss of the scattered partons in the dense nuclear matter, known as "jet quenching" [60]. At intermediate p_{T}, the baryon-to-meson ratios, p/π and Λ/K^0_s are found to be larger than unity and much higher than those observed in the peripheral A+A and elementary collisions. This baryon-to-meson ratio enhancement can be explained by the recombination/coalescence models which require constituent quarks in the partonic medium to coalesce into hadrons, or soft and hard partons to recombine into hadrons [61–63]. Thus, measurements of R_{CP} and baryon-to-meson ratios of strange hadrons are one of the corner stone pieces of evidence for the formation of the strongly interacting QGP medium. The precise measurement of these variables in heavy ion collisions at lower beam energies can potentially reveal the medium properties at finite μ_B and help locate the collision energy for the onset of deconfinement.

Apart from light hadrons, Fig. 7 also shows the energy dependence of strange particle yields at midrapidity for $K^{\pm}$, ϕ, $\Lambda(\bar{\Lambda})$, $\Xi^-(\overline{\Xi}^+)$ and $\Omega^-(\overline{\Omega}^+)$ from central heavy ion collisions. Results from STAR BES-I [33, 34] are compared with previously published STAR results at higher energies and other corresponding world data including experiments at the alternating gradient synchrotron (AGS) and Conseil Européen pour la Recherche Nucléaire (CERN) [58, 64–73]. The yields $\mathrm{d}N/\mathrm{d}y/\langle N_{\mathrm{part}}/2\rangle$ of the anti-hyperons $(\bar{\Lambda}, \overline{\Xi}^+, \overline{\Omega}^+)$ and ϕ meson increase rapidly with increasing energy, with a non-trivial energy dependence on Λ, Ξ^- and Ω^- yields. The Ξ^- and Ω^- yield first increases with energy from 7.7 to 19.6 GeV and then remains almost constant up to energies around 39 GeV, then rising again toward higher energies. The Λ yield first decreases from 7.7 to 39 GeV and then increases toward higher energies. The Λ behavior is similar to the trend displayed by proton in these measured energy regions [32], reflecting a significant increase in baryon density at lower collision energies. The observed Λ behavior can be the result of the interplay of the pair production of Λ-$\bar{\Lambda}$ and associated Λ production along with a kaon, with the former increasing strongly with an increase in collision energy and the latter increasing strongly with an increase in net-baryon density.

Figure 10 shows the energy dependence of $\Lambda(\bar{\Lambda})$ and $\Xi^-(\overline{\Xi}^+)$ midrapidity yield ratio to that of pions in central Au+Au collisions from RHIC STAR BES, and the existing data from various experiments [33, 64–67, 73–75] as well as the calculations from hadronic transport models (UrQMD 1.3, hadron-string dynamics (HSD)) and statistical hadron gas model (SHM) [55, 76, 77]. The STAR BES data are in good agreement with the trend displayed by the existing experimental data. The hadronic models (UrQMD 1.3 and HSD) seem to reproduce the Λ/π data, indicating that hadronic rescatterings might play an important role in hyperon production in heavy ion collisions at this energy range. However the default UrQMD (v1.3) fails to reproduce the Ξ/π ratio due to a smaller Ξ yield in the model [77]. On the other hand, the SHM model predictions agree well with data across the entire energy range from AGS to top RHIC. The SHM model used here is based on a grand canonical ensemble and assumes chemical equilibrium. The energy dependence of the parameters T_{ch} and μ_B in the model are obtained by a smooth parametrization of the original fitting parameters to the midrapidity particle ratios from heavy ion experiments at super proton synchrotron (SPS) and RHIC. Both Λ/π and Ξ^-/π ratios show a maximum at ~ 8 GeV,

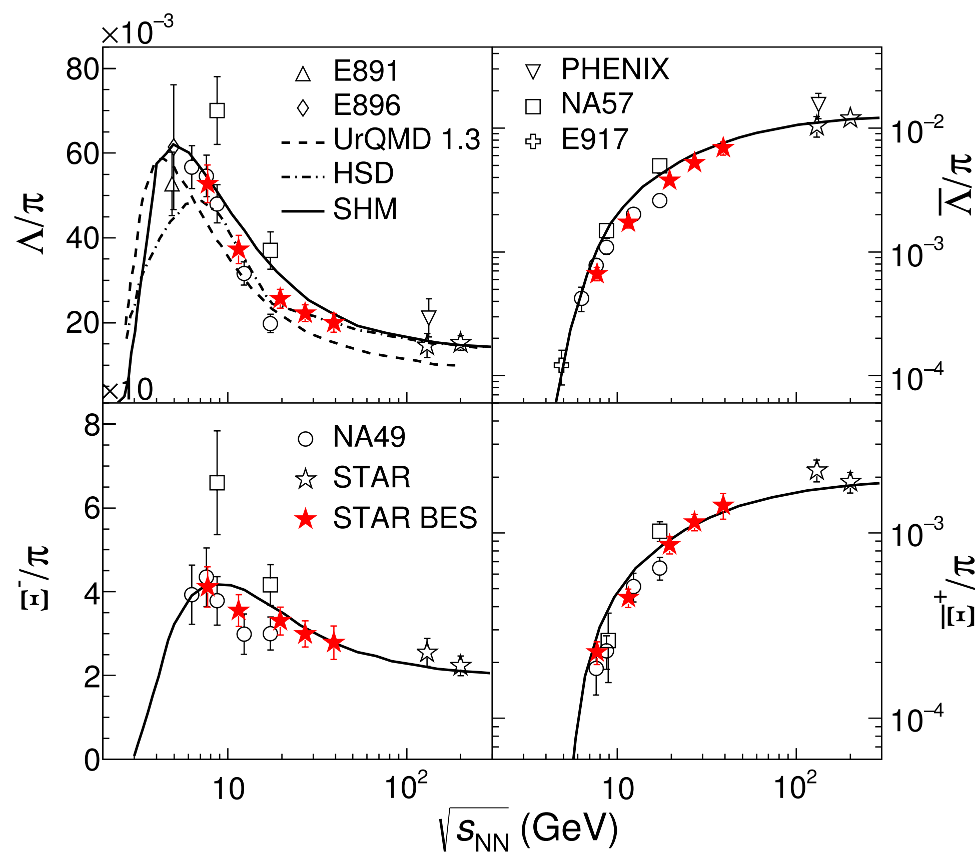

Fig. 10 (Color online) Energy dependence of Λ, $\bar{\Lambda}$, Ξ^-, and $\overline{\Xi}^+$ midrapidity yield ratio to that of pions ($1.5\ (\pi^+ + \pi^-)$) in central Au+Au collisions from STAR BES, compared with the existing data from various other experiments [33]

which seems to be consistent with the maximum net-baryon density at freeze-out at this collision energy.

Thermodynamic properties of strange quarks play an important role in understanding the QCD matter equation of state (EOS) in high-density regions. In statistical thermal models, grand canonical ensemble (GCE) and canonical ensemble (CE) statistical descriptions are applied differently to conserve the strangeness number in computing the final-state particle yields. It has been argued that at lower energies, strangeness number should be conserved locally on an event-by-event basis as described by CE, which leads to a reduction in the yields of hadrons with non-zero strangeness number ("Canonical Suppression") but not for the $\phi(1020)$ meson with zero net strangeness number ($S = 0$) [79]. Figure 11 shows the measurements of ϕ/K^- and ϕ/Ξ^- ratio in the central heavy ion collisions as a function of collision energy [33, 78, 80, 81] compared with various thermal and transport model calculations [76, 77, 82]. As shown in the plot, both GCE and CE models describe the measured ratios $\sqrt{s_{\mathrm{NN}}}$ at greater than 7.7 GeV, whereas clearly GCE fails when the collision energies approach the production threshold (2.89 GeV for ϕ and 3.25 GeV for Ξ^-). The measurements favor CE calculations with a small strangeness correlation length (r_c), necessitating more detailed investigation for precise and differential data.

In addition to the thermal model, transport model calculations from modified UrQMD with high mass strange resonances can reasonably reproduce the data in Fig. 11, implying that the feed-down effect is relevant [82, 83]. In heavy ion collisions, the near/sub-threshold production of multi-strange hadrons can be achieved from the multiple collisions of nucleons, produced particles, and short-lived resonances. However, particle production below the free nucleon–nucleon (NN) threshold is expected to be sensitive to the stiffness of the nuclear EoS at high density [84].

Figure 12 panel (a) shows the nuclear modification factor, R_{CP}, of K^0_S, in Au+Au collisions at STAR BES from 7.7 to 39 GeV [33]. For $p_{\mathrm{T}} \approx 4$ GeV/c, the K^0_S R_{CP} is below unity at $\sqrt{s_{\mathrm{NN}}} = 39$ GeV, which is similar to the observation at top RHIC energy although the lowest R_{CP} value is larger here. The K^0_S R_{CP} at $p_{\mathrm{T}} > 2$ GeV/c keeps increasing with decreasing collision energies, indicating that the partonic energy loss effect becomes less important. Eventually, the value of K^0_S R_{CP} tends to increase at large p_{T} at $\sqrt{s_{\mathrm{NN}}} = 11.5$ GeV and 7.7 GeV although the maximum accessible p_{T} is smaller at these two energies. This suggests that the cold nuclear matter effect (Cronin effect) starts to take over at these energies and enhances all the hadron yields at intermediate p_{T} (to ≈ 3.5 GeV/c). Similar to the observation for identified charged hadrons, the energy evolution of strange hadron R_{CP} reflects the decreasing partonic effect with decreasing beam energies [60].

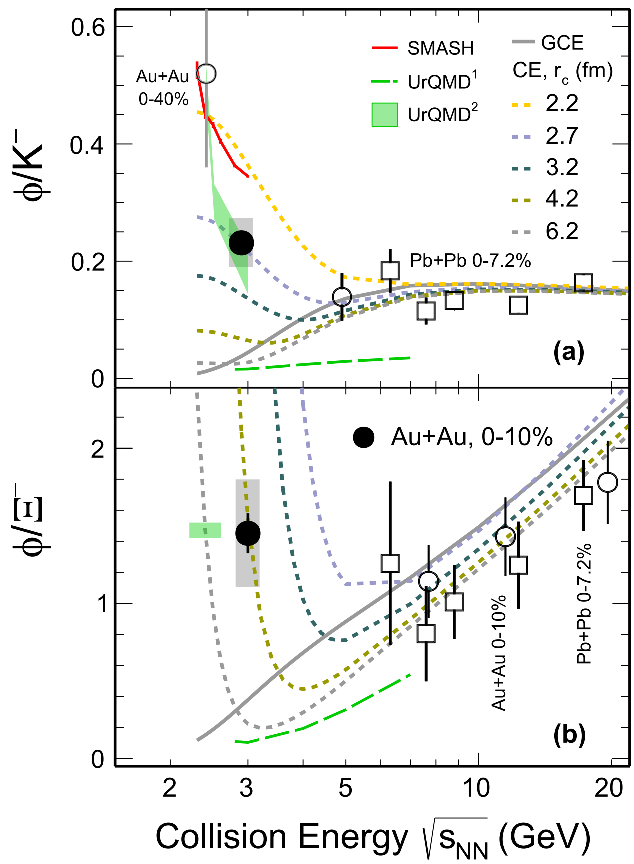

Fig. 11 (Color online) **a** ϕ/K^- and **b** ϕ/Ξ^- ratios in central heavy ion collisions as a function of collision energy, $\sqrt{s_{\mathrm{NN}}}$, compared with various thermal and transport model calculations. Figure taken from [78]

Figure 12 panel (b) shows the $\bar{\Lambda}/\mathrm{K}^0_S$ ratios as a function of p_{T} in central Au+Au collisions at STAR BES from $\sqrt{s_{\mathrm{NN}}} = 7.7$ GeV to 39 GeV [33]. The $\bar{\Lambda}$ is chosen because it is a newly produced baryon in the baryon-rich medium created by the lower BES energies. An enhancement of baryon-to-meson ratios is observed at intermediate p_{T} in central A+A collisions compared to peripheral A+A or p+p collisions at the same energy for energies $\sqrt{s_{\mathrm{NN}}} \geq 19.6$ GeV. The maximum value of $\bar{\Lambda}/\mathrm{K}^0_S$ reaches the maximum value of unity at $p_{\mathrm{T}} \approx 2.5$ GeV/c for most central collisions, whereas in peripheral collisions, the maximum value is significantly lower, only about 0.3–0.5 which is not shown in the plot. The enhancement of baryon-to-meson ratio in central collisions in these energies is interpreted as being a consequence of hadron formation through parton recombination and parton collectivity. Therefore, the baryon-to-meson ratios are expected to be sensitive to the parton dynamics of the collision system. Unfortunately, for $\sqrt{s_{\mathrm{NN}}} \leq 11.5$ GeV, the statistics on different centralities and maximum p_{T} are limited. Hence, whether the baryon-to-meson enhancement

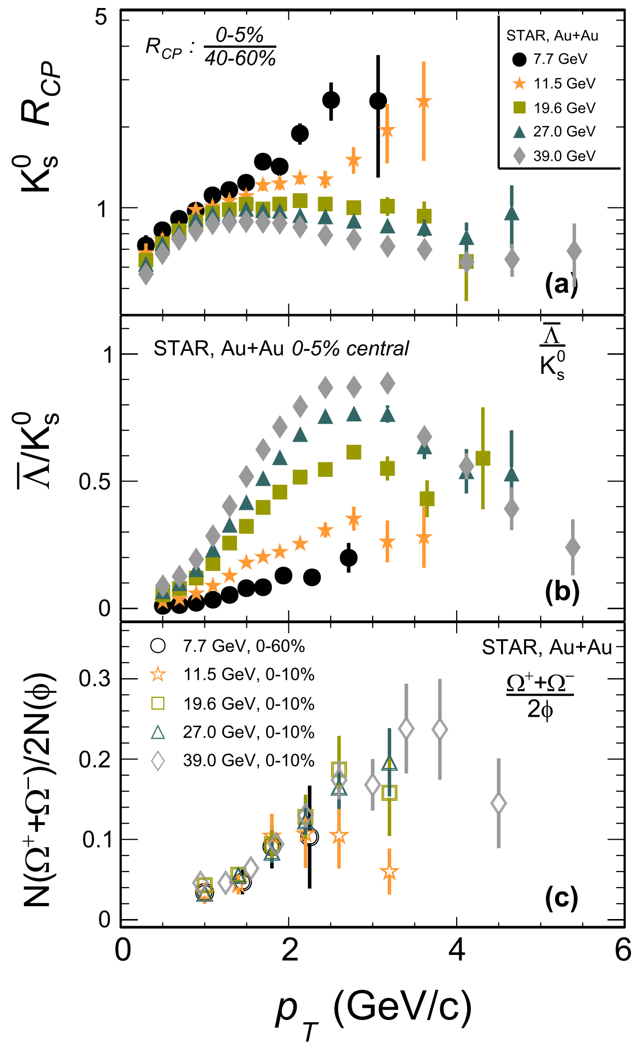

Fig. 12 (Color online) **a** K_S^0 nuclear modification factor, R_{CP}, at midrapidity in Au+Au collisions at STAR BES from 7.7 to 39 GeV [33]. **b** $\bar{\Lambda}/K_S^0$ ratio as a function of p_T in central Au+Au collisions at STAR BES [33]. **c** baryon-to-meson ratio, Ω/ϕ, as a function of p_T in central Au+Au collisions from STAR BES [33]

still persists at these low energies remains unclear with the current data.

Figure 12 panel (c) shows the baryon-to-meson ratio, Ω/ϕ, as a function of p_T in central Au+Au collisions from $\sqrt{s_{NN}}$ = 11.5 GeV to 39 GeV and $\sqrt{s_{NN}}$ = 7.7 GeV 0–60% centrality [33]. For energies $\sqrt{s_{NN}} \geq 19.6$ GeV, the measured data follow each other closely and also the previous measurement from 200 GeV, which is consistent with coalescence and recombination dynamics over a broad p_T range of 1–4 GeV/c [34]. The ratios at $\sqrt{s_{NN}} \leq 11.5$ GeV seem to deviate from the trend observed at higher beam energies. In particular, the ratios at 11.5 GeV appear to take a downward turn around p_T of 2 GeV/c, whereas those at higher beam energies such as 39 GeV, peak at p_T of 3 GeV/c or above. Since the Ω and ϕ particles have small hadronic rescattering cross sections, the change in these Ω/ϕ ratios may indicate a significant change in the hadron formation dynamics and/or the strange quark p_T distribution at the lower energies.

3.3 Collectivity

Collective observables, including radial and anisotropic flow, are powerful tools for extracting parameters of the EOS and understanding the properties of the medium created by high-energy nuclear collisions [4, 85, 86]. In this section, the energy dependence of v_1, v_2, their scaling, and EOS parameters are discussed.

The elliptic flow scaled by the number of constituent quarks (NCQ), v_2/n_q, for the copiously produced hadrons $\pi^{\pm}$ (squares), $K^{\pm}$ (crosses), p and $\bar{p}$ (circles), is shown as a function of the scaled transverse kinetic energy $(m_T - m_0)/n_q$ in Fig. 13. The data are from 10–40% mid-central Au+Au collisions at RHIC. Data points from collisions at 27 GeV and 54.4 GeV are shown as open and closed symbols, respectively. The colored dashed lines, also displayed in the figure, represent the scaling fit to the data from pions, kaons, and protons in Au+Au collisions at 7.7 GeV, 14.5 GeV, 27 GeV, 54.4 GeV, and 200 GeV for both positively and negatively charged particles [90, 91]. Although the overall quark number scaling is evident, the best scaling is reached by the RHIC top energy $\sqrt{s_{NN}}$ = 200 GeV collisions [92]. As collision energy decreases, the scaling deteriorates. Particles and antiparticles are no longer consistent with the single-particle NCQ scaling due to the mixture of transported and produced quarks [91]. More detailed discussions on the effects of transported quarks on collectivity can be found in [93, 94]. An important evidence for QGP formation in high-energy collisions at RHIC, is the observed NCQ scaling that originates from partonic collectivity [92, 95, 96]. Interestingly, in the analysis of the elliptic flow of light nuclei in low- and intermediate-energy nuclear reactions, a similar scaling law exists, i.e., the elliptic flow of light nuclei is scaled according to the number of constituent nucleons [97]. Inspired by [97], the STAR experiment of relativistic heavy ion collisions [98] also confirms the nucleon-number scaling of the elliptic flow of light nuclei, that is, it fulfills the theoretical prediction of [97]. The similarity between NCQ scaling of elliptic flows and nucleon-number scaling of light nuclei lies in the merger mechanism of hadron formation or nucleosynthesis, whereas the difference lies in whether the merger is at the quark or nucleon level. Notably, the LHC-ALICE collaboration reported measurements of higher-order anisotropic flows [99], providing for the first time experimental measurements of triangular flow v_3. The NCQ scaling of higher

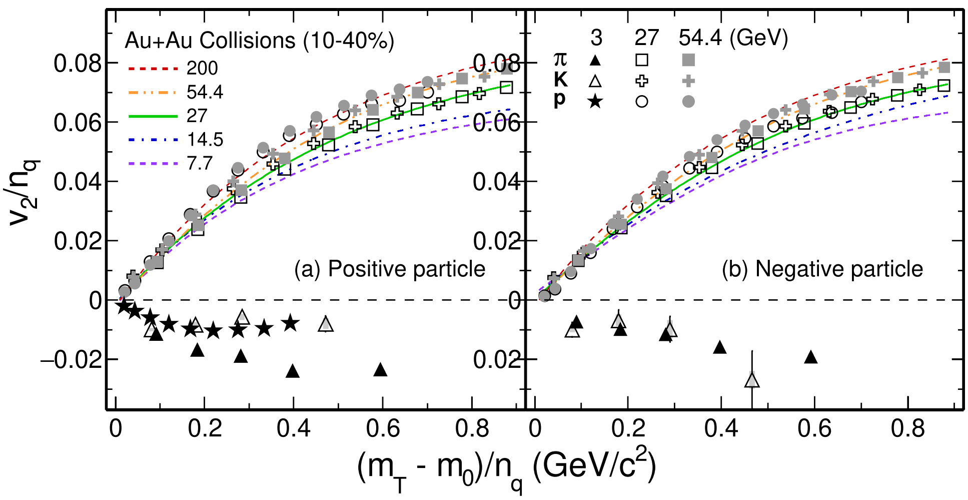

Fig. 13 (Color online) Elliptic flow (v_2) scaled by number of constituent quarks (n_q); (v_2/n_q) is shown as a function of scaled transverse kinetic energy $(m_T - m_0)/n_q$ for pions, kaons, and protons from Au+Au collisions in 10–40% centrality at $\sqrt{s_{NN}} = 3$ GeV, 27 GeV, and 54.4 GeV for positively charged particles (left panel) and negatively charged particles (right panel). Colored dashed lines represent the scaling fit to data from Au+Au collisions at 7.7 GeV, 14.5 GeV, 27 GeV, 54.4 GeV, and 200 GeV from the STAR experiment at RHIC [87–89]. Statistical and systematic uncertainties are shown as bars and gray bands, respectively

order collective flows is theoretically discussed in [100] and confirmed in experimental measurements [101], which can also be regarded as a further probe of QGP. Experimental efforts on the measurement of v_3 in BES energies have also been conducted [102]. Based on the data [102], detailed tests on NCQ scaling seem promising.

At low energies of $\sqrt{s_{NN}} = 3.0$ GeV Au+Au collisions, a totally different scaling behavior emerges, as shown in Fig. 13. Unlike that observed in high-energy collisions, all v_2 values are negative, which is a characteristic of nuclear shadowing in such non-central collisions. There is no sign of NCQ scaling at this low energy [103]. These results clearly indicate different properties for the matter produced. With the baryonic mean field, hadronic transport model calculations from jet AA microscopic transport model (JAM) [104] and UrQMD [76, 77] reproduce the observed negative values of v_2 for protons as well as Λs. In other words, in Au+Au collisions at $\sqrt{s_{NN}} = 3.0$ GeV, partonic interactions no longer dominate, and baryonic scatterings take over, indicating that predominantly hadronic matter is created in such low-energy collisions.

Now, focusing on the p_T-integrated results, we jointly examine v_1 and v_2. The collision energy dependence of directed and elliptic flow is summarized in Fig. 14, where panel (a) shows the slope of the p_T-integrated directed flow at midrapidity, $dv_1/dy|y = 0$, for π, K, p, Λ, and multi-strange hadrons ϕ and Ξ^- from Au+Au collisions in the 10–40% centrality interval. Here, K and π represent the combined results of $K^\pm$ and K^0_S, and $\pi^\pm$, respectively. Panel (b) displays the p_T-integrated v_2 at midrapidity for π, K, p, and Λ as open squares, filled triangles, filled circles, and open circles, respectively. Due to partonic collectivity in Au+Au collisions at high energy [106], all observed v_1 slopes and v_2 at midrapidity are found to be negative and positive, respectively, which is opposite to what is observed at low energy. This can be seen in the 3.0 GeV Au+Au collision results shown in Fig. 14. The early strong partonic expansion leads to positive v_2 with NCQ scaling in high-energy collisions, whereas at 3.0 GeV, both weaker pressure gradients and shadowing of the spectators result in negative v_2 values without scaling. The results from calculations using the hadronic transport models JAM and UrQMD are also shown as colored bands in the figure. By including the baryonic mean field, both the JAM and UrQMD models reproduce the trends for both $dv_1/dy|_{y=0}$ and v_2 for baryons, including protons and Λ. The consistency of the transport models (JAM and UrQMD) with the baryonic mean field for all measured baryons implies that the dominant degrees of freedom at a collision energy of 3.0 GeV are from the interacting baryons. The signatures for the transition from partonic dominance to hadronic and then to baryonic dominance regions have been discussed in [4, 32, 93, 105] for the ratios of K^+/π^+ and net-particle v_1 slopes, respectively. The data from 3.0 GeV Au+Au collisions clearly reveal that baryonic interactions dictate the collision dynamics.

The results of collectivity, EOS, and phase structure are closely connected. By comparing measurements with calculations, the parameters of the EOS for each collision can be readily extracted [108, 109]. As an example, Fig. 15 shows

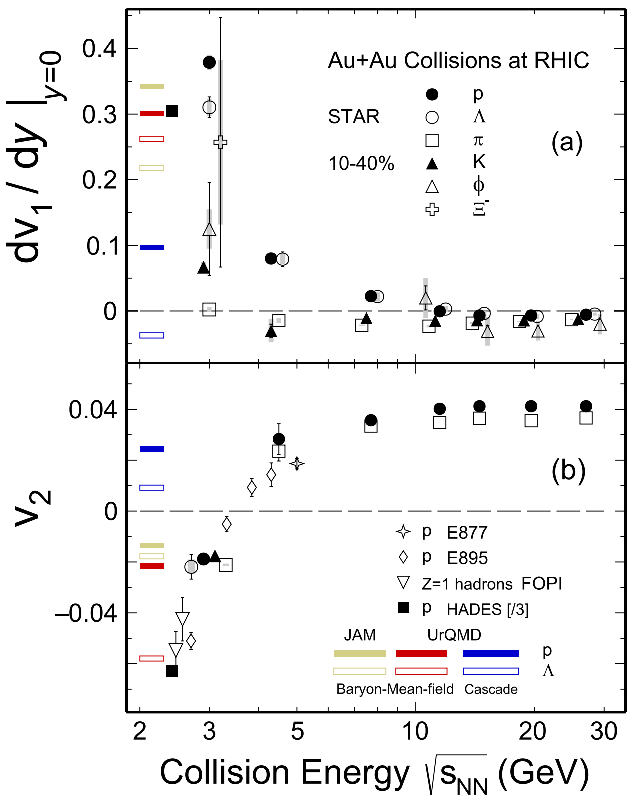

Fig. 14 (Color online) Collision energy dependence of the directed flow slope $dv_1/dy|_{y=0}$ for p, Λ, charged πs, and kaons (including $K^{\pm}$ and K^0_S), ϕ, and Ξ^- (top panel) [93, 105]. The bottom panel shows the elliptic flow v_2 for protons and πs from heavy ion collisions [91, 92]. Statistical and systematic uncertainties are shown as bars and gray bands, respectively. The JAM and UrQMD results are displayed as colored bands: golden, red, and blue bands represent the JAM mean field, UrQMD mean field, and cascade mode, respectively

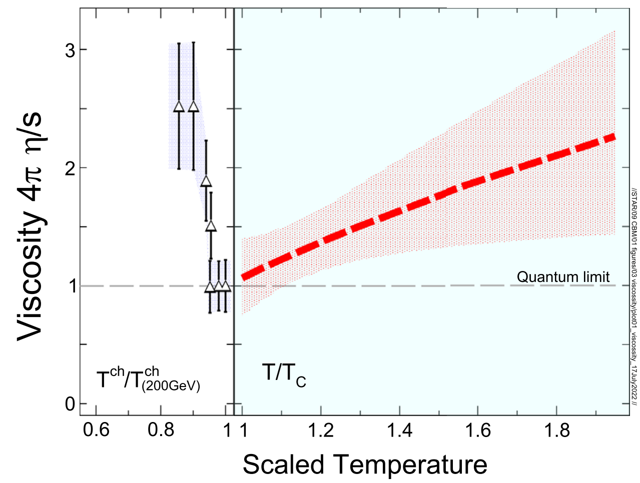

Fig. 15 (Color online) The effective values of shear viscosity-to-entropy ratio, $4\pi\eta/s$, shown as a function of the scaled temperature. The horizontal dashed line indicates the quantum lower limit. Left panel: $4\pi\eta/s$ extracted from the energy dependence of the measured v_2 [107] and v_3 [102], shown as the scaled chemical freeze-out temperature $T_{\rm ch}/T_{\rm ch}$(200 GeV). Right panel: temperature evolution of $4\pi\eta/s$, extracted from Bayesian analyses [108, 109]

the ratio of shear viscosity to entropy as a function of scaled temperature [110]. In the left panel, chemical freeze-out temperature from each energy [32] is used and normalized to that from Au+Au collisions at $\sqrt{s_{\rm NN}}$ = 200 GeV. In the high-energy limit, $\sqrt{s_{\rm NN}}$ = 39 −200 GeV, the ratio, namely the quantum limit, reaches unity, implying that the medium created in such collisions is dominated by partonic interactions with a minimum value of $4\pi\eta/s$. At lower collision energies, on the other hand, hadronic interactions become dominant, and the medium shows a rapid increase in the viscosity-to-entropy ratio. The right panel shows the temperature evolution of the shear viscosity-to-entropy ratio as a function of the scaled temperature $T/T_{\rm C}$. Here, $T_{\rm C}$ represents the critical temperature in the calculation [108, 109]. The entire curve is extracted from the experimental results of $R_{\rm AA}$ and v_2 from Au+Au collisions at $\sqrt{s_{\rm NN}}$ = 200 GeV. The observed V-shaped feature is quite similar to what is described in [111] for a system dominated by electromagnetic interactions. The phase transition is universal and independent of the degrees of freedom of the medium under study. This unique feature is a clear evidence of the crossover transition in strong interactions. For a comprehensive discussion on the shear viscosity and phase transition in nucleon and quark levels, the reader is referred to a recent review [112].

3.4 Chirality

Quark interactions with topological gluon configurations can induce chirality imbalance and local parity violation in QCD [113–115]. In relativistic heavy ion collisions, this can lead to observable electric charge separation along the direction of the strong magnetic field produced primarily by spectator protons [116–118]. This is called the chiral magnetic effect (CME). A CME-induced charge separation, if observed, would confirm a fundamental property of QCD. Measurements of electric charge separations can provide a means for studying non-trivial QCD topological structures and are therefore of paramount importance. Extensive theoretical and experimental efforts have been devoted to the search for CME [118–120].

The commonly used observable to measure charge separation is the three-point correlator difference [124], $\Delta\gamma \equiv \gamma_{\rm OS} - \gamma_{\rm SS}$. Here $\gamma = \langle\cos(\alpha + \beta - 2\psi_2)\rangle$, α, and β are the azimuthal angles of the two charged particles and ψ_2 is that of the second-order harmonic plane; $\gamma_{\rm OS}$ denotes the γ of opposite electric charge sign (OS), and $\gamma_{\rm SS}$ denotes that of the same sign pairs (SS). The first γ measurements were carried out by the STAR collaboration in Au+Au collisions

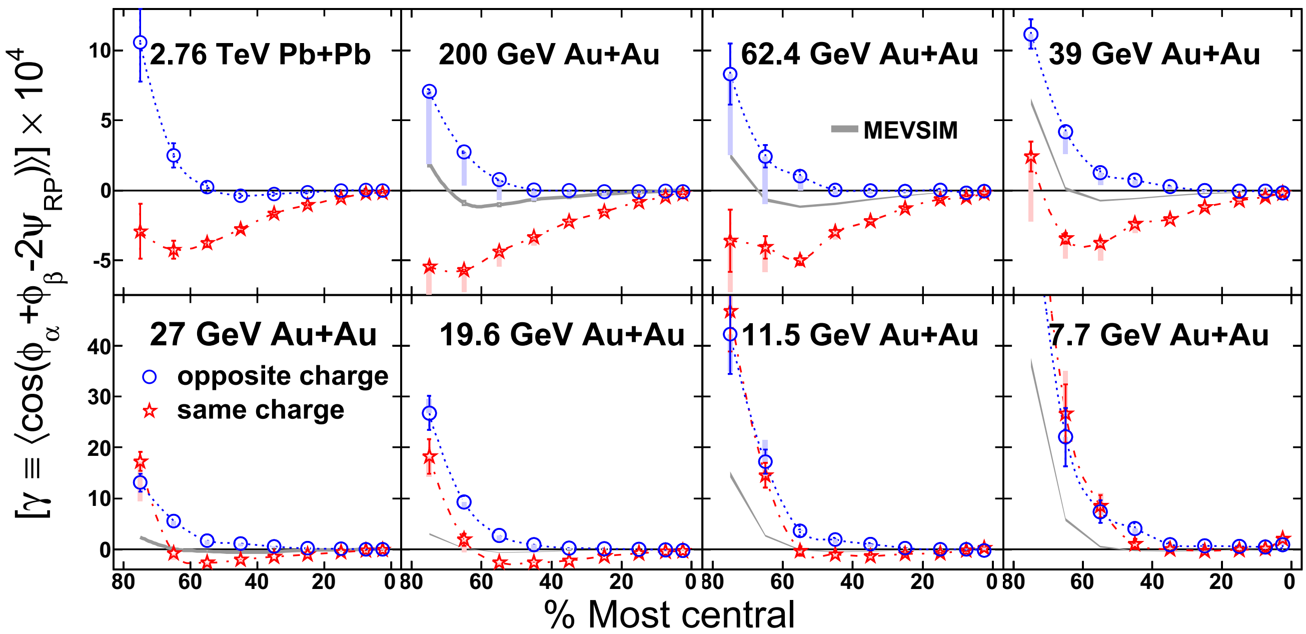

Fig. 16 (Color online) γ correlators as functions of centrality in Au+Au collisions at $\sqrt{s_{NN}} = 7.7 - 200$ GeV from STAR [121, 122] and in Pb+Pb collisions at $\sqrt{s_{NN}} = 2.76$ TeV from ALICE [123]

at top RHIC energy in 2009 [121], which resulted in significant $\Delta\gamma$ observations. Further measurements were made at lower RHIC energies by STAR [122] and at higher LHC energies by ALICE [123]. Figure 16 shows the γ_{OS} and γ_{SS} correlators as a function of the collision centrality in Au+Au collisions at $\sqrt{s_{NN}} = 7.7 - 200$ GeV at RHIC and in Pb+Pb collisions at 2.76 TeV at LHC. At high collision energies, charge-dependent signals are observed, and γ_{OS} is larger than γ_{SS}. The difference between γ_{OS} and γ_{SS}, i.e. $\Delta\gamma$, decreases with increasing centrality, which is consistent with the expectation of a magnetic field strength decrease with increasing centrality. At the low collision energy of $\sqrt{s_{NN}} = 7.7$ GeV, the difference between γ_{OS} and γ_{SS} disappears, which is consistent with the disappearance of the CME in the presumably hadronic dominant interactions at this energy. Thus, these results are qualitatively consistent with the CME expectation.

One of the difficulties in interpreting the positive $\Delta\gamma$ is whether the CME is the major charge-dependent background contribution to the observable [125–127], such as those from resonance decays and jets. The $\Delta\gamma$ variable is ambiguous between differentiating an OS pair from the CME back-to-back perpendicular to ψ_2 and an OS pair from a resonance decay along ψ_2. More resonances are produced along the ψ_2 than perpendicular to it, with the relative difference quantified by the elliptical anisotropy parameter v_2 of the resonances. (Jet correlations also exhibit azimuthal anisotropy because of jet quenching effects in heavy ion collisions [128].) The CME background arises from the coupling of this elliptical anisotropy and genuine particle correlations from resonance decays and jets, among others. Calculations using the blast wave parameterizations of the measured particle production data can essentially reproduce the entirety of the measured γ correlations [127].

The CME and the v_2-related background are driven by different physics: the CME is sensitive to the magnetic field which is mostly perpendicular to the spectator plane, whereas the v_2-related background is connected to the participant plane. In non-central heavy ion collisions, the participant plane is generally aligned with the reaction plane, and the $\Delta\gamma$ measurement is thus entangled by the two contributions of possible CME and v_2-induced background. In small-system p+A or d+A collisions, the participant plane is determined purely by geometry fluctuations that are uncorrelated with the magnetic field direction [129]. As a result, any CME signal would average to zero in small-system collisions. Background sources, on the other hand, contribute similarly to small-system collisions and heavy ion collisions. In Fig. 17 (left), the first $\Delta\gamma$ measurements in small system p+A collisions from CMS [129] are displayed. Within a margin of uncertainty, the results of p+Pb and Pb+Pb collisions exhibit the same magnitude and trend as a function of multiplicity. Figure 17 (right) shows the $\Delta\gamma$ measurements in

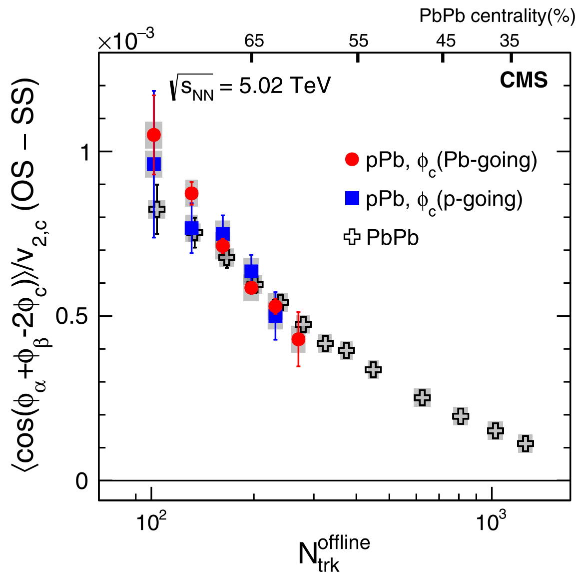

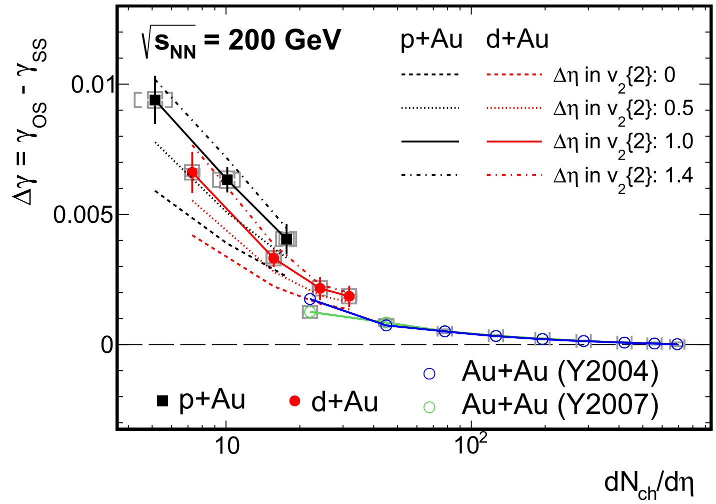

Fig. 17 (Color online) The $\Delta\gamma$ correlators as functions of multiplicity in p+Pb and Pb+Pb collisions from the LHC compact moon solenoid (CMS) [129] (left) and in p/d+Au and Au+Au collisions from RHIC STAR [130] (right)

small system p/d+A collisions from STAR [130]. The trends of the magnitudes are similar, decreasing with increasing multiplicity. These results indicate that strong correlations are present in small systems, contributing to the γ correlators. The nature of these correlations may be attributable to genuine three-particle correlations, which would explain the peripheral heavy ion data but would be insufficient for mid-central heavy ion data as they are strongly diluted by event multiplicity. The nature of some of the correlations may be from flow as there are indications of collective flow in these small systems [131, 132], especially at LHC energies [133]. Nevertheless, the small system results suggest the complex nature of the backgrounds which must be rigorously removed before addressing the important physics of the chiral magnetic effect.

Since the major background is induced by v_2, examining the $\Delta\gamma$ observable with varying v_2 while holding the expected CME signal constant, is of interest. The event shape engineering (ESE) method is performed based on the magnitude of the flow vector to possibly access the geometry of the initial participant. The ESE selection of events is not expected to affect the magnetic field when restricted to a specified narrow centrality. The different dependencies of the CME signal and background on v_2 (q_2) can possibly be used to disentangle the CME signal from the background. Using the ESE method, the ALICE experiment showed that the CME fraction in the measured $\Delta\gamma$ is consistent with zero [134].

Examining the $\Delta\gamma$ observable with varying magnetic field while keeping the v_2 relatively constant is also of interest. To gauge the differences in the magnetic field relative to v_2, isobaric and U+U collisions have been proposed [138]. Isobaric collisions were proposed to study two systems with similar v_2 but different magnetic field strengths [138], such as $^{96}_{44}$Ru and $^{96}_{40}$Zr, which have the same mass number but different charge (proton) number. One would thus expect that v_2 would be very similar at midrapidity in $^{96}_{44}$Ru $+^{96}_{44}$ Ru and $^{96}_{40}$Zr $+^{96}_{40}$ Zr collisions, but the magnetic field, proportional to the nuclei electric charge, could vary by 10%. The variation of the magnetic field strength between $^{96}_{44}$Ru $+^{96}_{44}$ Ru and $^{96}_{40}$Zr $+^{96}_{40}$ Zr collisions provides an ideal way to disentangle the signal of the chiral magnetic effect from v_2 related background, as v_2 related backgrounds are expected to be very similar between these two systems.

Figure 18 shows the ratio of $\Delta\gamma/v_2$ in Ru+Ru over Zr+Zr collisions from the isobar analysis [135–137], as an observable. The CME-sensitive observable ratios lie below unity leading to the conclusion that no predefined CME signatures, such as a larger than unity Ru+Ru over Zr+Zr ratio of $\Delta\gamma/v_2$, are observed in this blind analysis. This is rather counterintuitive at a first glance but can be explained using nuclear structure considerations. In fact, the ^{96}Zr nucleus was predicted to be larger than ^{96}Ru because of its thicker neutron skin, resulting in a slightly smaller energy density and fewer particles being produced in Zr+Zr than in Ru+Ru collisions [139–141]. The larger ^{96}Zr nucleus also provides smaller eccentricity at a given centrality and thus smaller v_2 [139, 140]. Although the non-identical v_2 is properly considered in the blind analysis observable $\Delta\gamma/v_2$, non-identical event multiplicities are not. After properly factoring

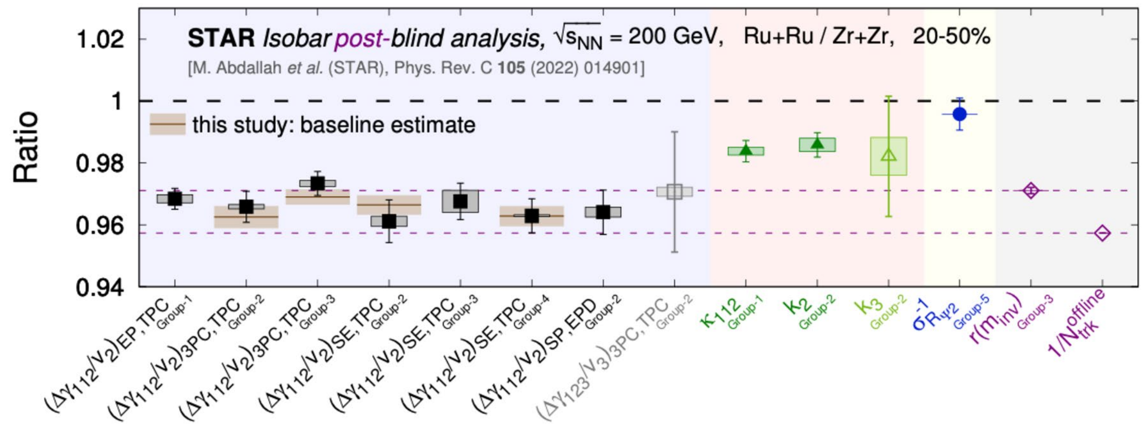

Fig. 18 (Color online) Compilation of results from isobar analysis. Only contrasting results from the two isobar systems are shown. The results are expressed in terms of Ru+Ru over Zr+Zr collision measurement ratios. Solid dark symbols indicate CME-sensitive measures, whereas open light symbols indicate their counterpart insensitive to CME. The vertical lines indicate statistical uncertainties whereas boxes indicate systematic uncertainties. The colors in the background are intended to separate different types of measures. The fact that CME-sensitive observable ratios lie below unity leads to the conclusion that no predefined CME signatures are observed in this blind analysis [135]. The estimated background baselines from non-flow contamination for the four cumulant measurements of the isobar $\Delta\gamma/v_2$ ratios are indicated by horizontal bars (central values) and shaded areas (total uncertainties, the quadratic sum of the statistical and systematic uncertainties on the background baseline estimates) [136, 137]

in the multiplicity, the isobar ratios of $N\Delta\gamma/v_2$ from various analyses shown in Fig. 18 indicate a positive signal of a few standard deviations [135, 142]. However, non-flow contamination exists in the $\Delta\gamma/v_2$ ratio variable [143]. One such contamination is the aforementioned genuine three-particle correlations because $\Delta\gamma$ is measured by the three-particle correlator in STAR TPC. Another contamination is attributed to the fact that two-particle v_2 cumulant measurements are contaminated by non-flow correlations and such v_2 values are used to compute the $\Delta\gamma$ from the three-particle correlator measurement. Rigorous studies of non-flow contamination have been conducted in post-blind analyses, and improved background baselines are derived [136, 137]. Figure 18 shows the measured isobar ratios of $\Delta\gamma/v_2$ from the blind analysis along with the estimated background baselines from the post-blind analysis. The results show that the isobar ratios are consistent with the baselines, indicating that no statistically significant CME signals have been observed in the isobar data.

The STAR isobar data, without any clear evidence for a possible CME-related signal difference possibly arising from the charge difference (44 in Ru versus 40 in Zr), have provided important lessons in the experimental search for CME. First, the difference in nuclear shape and/or neutron skin between isobaric nuclei can induce percent-level background variations, which cannot be easily estimated using theoretical calculations or controlled with experimental constraints. Thus, searches for small differences in the CME signal arising from the magnetic field variation in isobar collisions is extremely challenging. Second, the strength of the magnetic field plays a critical role in the CME signal; therefore, larger nuclei would be preferable in the search for a possible CME-induced signal in $\Delta\gamma$ correlations. Third, a better understanding of the background sources in the $\Delta\gamma$ correlator is required to suppress this background from elliptic flow and non-flow correlations.

The major background source in the CME observable $\Delta\gamma$ is induced by elliptic flow (v_2). The original event shape engineering approach [134, 144, 145] uses particles from separate rapidity or pseudorapidity regions to define event classes. This approach can select event shapes sensitive to the eccentricity of the initial overlapping participants and the corresponding geometrical fluctuations. However, for particles of interest used for measuring the CME-sensitive observable $\Delta\gamma$ in a different rapidity region, the event-by-event v_2 background has contributions from both eccentricity and particle emission pattern fluctuations. Petersen and Muller [146] pointed out that emission pattern fluctuations dominate the event-by-event v_2 fluctuations. Recently, Xu et al. proposed a novel event shape selection (ESS) approach to suppress the background in the CME $\Delta\gamma$ measurement [147]. They found that to suppress the apparent flow-induced background in $\Delta\gamma$, the combined event-by-event information from eccentricity and emission pattern fluctuations from particles of interest should be used to select azimuthally round shape events for correlator measurements. With this ESS approach, the suppression of the flow-related background becomes possible. Using a multi-phase transport (AMPT) [148] and anomalous viscous fluid dynamics (AVFD) [149] model simulations, Xu et al. [147] showed that the most effective ESS approach is to use particle pairs to construct the event shape variable, thereby forming event shape classes for the CME-sensitive correlator to calculate the zero elliptic flow at the limit for particles of interest. This is consistent with the expectation that the background in $\Delta\gamma$ has significant contributions from particle pair emissions coupled with elliptic flow.

The RHIC BES-II also provides a unique venue for the CME search, covering the center-of-mass energies from 7.7 to 27 GeV. At these beam energies, the STAR event plane detector (EPD), added during the BES-II program, can register spectator protons from the colliding beams. This capability allows an accurate estimation of the reaction plane, enhancing the sensitivity to the magnetic field direction and suppressing non-flow contributions to the background. For Au+Au collisions at the top RHIC energy, spectator neutrons may be detected by the zero-degree calorimeter (ZDC) although the corresponding event plane resolution is not as good as that in the BES-II data. Theoretical calculations expect the initial magnetic field to be smaller in Au+Au collisions from BES-II than that from the top RHIC energy. However, the dynamics of the QGP formation and time evolution of the magnetic field in QGP as a function of collision energy have not been fully understood. Recent STAR measurements of the deflection of charged particles by the magnetic field in heavy ion collisions indicate significant imprints of magnetic field effects at these BES-II energies [150]. The STAR collaboration reported preliminary results on the CME search from the RHIC BES-II data at the 2023 Quark Matter Conference, demonstrating a promising approach for focusing on Au+Au collisions using an innovative experimental technique for background suppression [151].

As aforementioned, the $\Delta\gamma$ measurement in heavy ion collisions is entangled by two contributions, one from the CME and the other from the v_2 induced background. These are sensitive to differences in planes, allowing the measurement of $\Delta\gamma$. The background is related to v_2, as determined by the participant geometry, and therefore is the largest with respect to the participant plane (ψ_{PP}). The CME-driven charge separation is along the magnetic field direction (ψ_B), unlike ψ_{PP}. The ψ_B and ψ_{PP} are generally correlated with the impact parameter direction, ψ_{RP}, and therefore correlated among themselves. While the magnetic field is mainly produced by spectator protons, their positions fluctuate, thus ψ_B is not always perpendicular to ψ_{RP}. The position fluctuations of participant nucleons and spectator protons are independent, whereby ψ_{PP} and ψ_B fluctuate independently about ψ_{RP}. Notably, a new approach has been proposed to measure $\Delta\gamma$ with respect to ψ_{SP} and ψ_{PP} to disentangle the CME signal from the v_2 background [152, 153]. This is exploited by STAR in measuring $\Delta\gamma$ with respect to the first-order harmonic plane from the ZDC and second-order harmonic plane from the TPC. Because the former aligns better with the spectator plane and the latter aligns better with the participant plane, these measurements contain different amounts of sensitive flow backgrounds and magnetic field-sensitive CME signal in the harmonic plane, enabling the extraction of a possible CME.

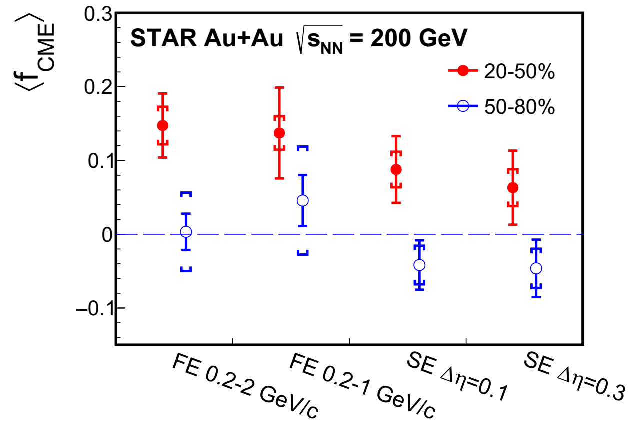

Fig. 19 (Color online) The flow background removed CME signal fraction $\langle f_{\mathrm{CME}} \rangle$ in 50–80% (open markers) and 20–50% (solid markers) centrality Au+Au collisions at $\sqrt{s_{\mathrm{NN}}} = 200$ GeV [154]. Results are shown for the full-event (FE) analysis method with two $p_\perp$ ranges and sub-event (SE) analysis method with two $\Delta\eta$ gaps. Error bars show statistical uncertainties; the caps indicate systematic uncertainties

STAR reported such measurements in Au+Au collisions at $\sqrt{s_{\mathrm{NN}}} = 200$ GeV [154], as shown in Fig. 19. The charge separation, with the flow background removed, is consistent with zero in peripheral collisions. In mid-central collisions, on the other hand, an intriguing indication of finite CME signals is observed on the order of 1–3σ standard deviations.

In RHIC 2023–2025, STAR is expected to collect approximately 20 B events, which is about a factor of 10 more compared to the data used for Fig. 19. More precise results are expected in the near future. New analyses utilizing event shape engineering with particle pair anisotropy and invariant mass are ongoing, and results are expected soon.

3.5 Criticality

In high-energy nuclear collisions where the baryon density is vanishingly small, the transition from QGP to hadronic matter is a smooth crossover [155]. At finite density and lower temperatures, the transition is speculated to be first order, with an associated phase boundary. The point that connects the smooth crossover and first-order phase boundary is

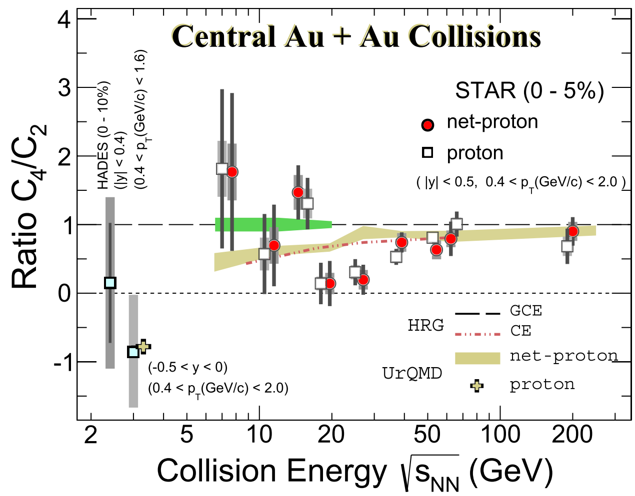

Fig. 20 (Color online) Collision energy dependence of the ratios of cumulants, C_4/C_2, for proton (squares) and net-proton (red circles) for top 0–5% Au+Au collisions at RHIC [38]. The points for protons are shifted horizontally for clarity. The new result for proton from $\sqrt{s_{\mathrm{NN}}} = 3.0\,\mathrm{GeV}$ collisions is shown as a filled square. High acceptance dielectron spectrometer (HADES) data of $\sqrt{s_{\mathrm{NN}}} = 2.4\,\mathrm{GeV}$ 0–10% collisions is also shown. Results from HRG and transport model UrQMD [76, 77] are shown

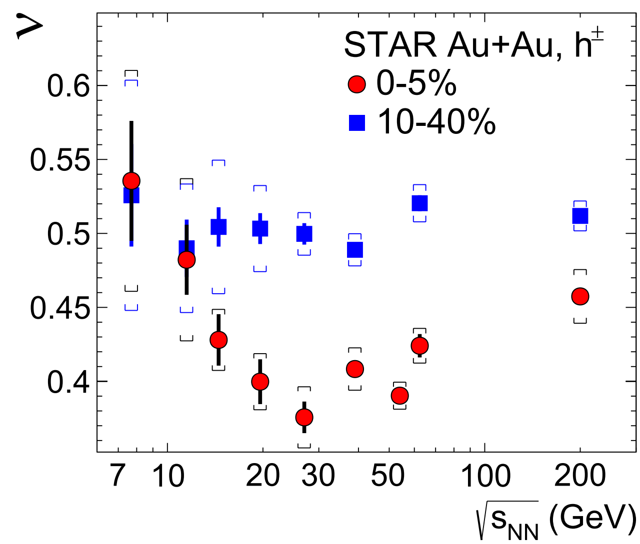

Fig. 21 (Color online) Energy dependence of the scaling exponent (ν) for identified charged hadrons ($h^{\pm}$) in Au+Au collisions at $\sqrt{s_{\mathrm{NN}}} = 7.7 - 200$ GeV [161]. Red circles and blue squares represent ν in the most central collisions (0–5%) and mid-central collisions (10–40%), respectively. The statistical and systematic errors are shown in bars and brackets, respectively

the QCD critical point [156]. Since 2010, RHIC has conducted two rounds of beam energy scan campaigns primarily aimed at investigating the QCD critical point. The BES programs cover an energy range from $\sqrt{s_{\mathrm{NN}}} = 200\,\mathrm{GeV}$ to 3.0 GeV, corresponding to a baryonic chemical potential of $20\,\mathrm{MeV} \leq \mu_{\mathrm{B}} \leq 750\,\mathrm{MeV}$. As of the summer of 2022, both BES-I and BES-II have been completed.

High-order cumulants of protons and net-protons (event-by-event number: net-p = p − p̄) distributions are used in the search for the QCD critical point [157] because of their high sensitivity to correlation length. The experimental results shown as a function of the collision energy are depicted in Fig. 20. Overall, the ratios of C_4/C_2 for net-protons from collider mode ($\sqrt{s_{\mathrm{NN}}} \geq 7.7\,\mathrm{GeV}$) [38, 158] and protons from the fixed-target mode decrease as collision energy decreases as dictated by the baryon number conservation. Both the hadronic resonance gas model and hadronic transport model UrQMD [76, 77] calculations reproduce this trend. As a function of collision energy, a rise and then fall of the net-proton C_4/C_2 (or $\kappa\sigma^2$) is expected to indicate the critical behavior near the critical point in the QCD phase diagram. While results of C_4/C_2 ratios from BES-I have shown dip like energy dependence around 20 GeV, the statistics at lower collision energies are too poor to draw any conclusions regarding this prediction. Note that at low energies, or equivalently, in the high baryon density region, both the HADES ($\sqrt{s_{\mathrm{NN}}} = 2.4\,\mathrm{GeV}$) and STAR ($\sqrt{s_{\mathrm{NN}}} = 3.0\,\mathrm{GeV}$ [159, 160]) high moment proton results are below the Poisson baseline, and the non-critical hadronic transport model calculations reproduce the data at the high baryon density region. This implies that this energy regime is dominated by hadronic interactions. To look for an oscillation pattern in the energy dependence of the ratio of C_4/C_2, the second phase of the beam energy scan (BES-II) was conducted at RHIC. The BES-II data analyses are under way.

In addition, it is predicted that density fluctuations near the QCD critical point can be probed via an intermittency analysis in relativistic heavy ion collisions [162, 163]. Figure 21 shows the energy dependence of the scaling exponent (ν) for identified charged hadrons in Au+Au collisions for two different collision centralities (0–5% and 10–40%) [161]. In the most central collisions, ν exhibits a non-monotonic behavior as a function of collision energy, reaching a minimum around $\sqrt{s_{\mathrm{NN}}} = 20 - 30$ GeV. In contrast, for 10–40% central collisions, ν remains approximately constant with increasing $\sqrt{s_{\mathrm{NN}}}$. The observed non-monotonic energy dependence of ν in the most central collisions can indicate the density fluctuations induced by the QCD critical point. However, at $\sqrt{s_{\mathrm{NN}}} \leq 11.5$ GeV, large systematic and statistical uncertainties exist for ν. Higher statistics data are required from the BES-II program to confirm this energy dependence. The measured value of ν is significantly smaller than the theoretical predictions of $\nu = 1.30$ from the Ginzburg–Landau (GL) theory and $\nu = 1.0$ from the 2D Ising model. These theoretical values are derived from calculations over the entire phase space without constraints on acceptance, whereas the experimental measurements are limited to the available transverse momentum space; ν is anticipated to increase if measured over the entire phase space, particularly when including higher p_T regions. Therefore, theoretical calculations that consider a reduced transverse momentum phase space and equivalent experimental acceptance, are required to understand the measured scaling exponent. The transport-based UrQMD model is unable to calculate ν because of the absence of power-law scaling of $\Delta F_q(M) \propto \Delta F_2(M)^{\beta_q}$. Consequently, models that exhibit such power-law scaling are required to produce a non-critical baseline for comparison with experimental data.

Recently, a study was conducted on the information entropy [164] of the net-proton multiplicity distribution using the hybrid model of ideal fluid dynamics plus UrQMD [165]. The ratios of the net-proton information entropies of the UrQMD result with EoS:CH (chiral+hadronic gas EoS with first-order transition and critical endpoint) were compared with those of UrQMD with EoS:BM (bag model EoS with strong first-order phase transition between QGP and hadronic phase), STAR experimental data, and UrQMD results without hydrodynamic EOS. The comparisons show that the STAR experimental data extracted from [38] display an enhancement in collision at 20 GeV with respect to the baseline entropy without hydrodynamics, which is consistent with the minimum $\kappa\sigma^2$ value reported in [158]. On the other hand, the UrQMD simulations with the EoS:BM and EoS:CH EOS also show slightly pronounced enhancements, at energies higher than approzimately 30 GeV, consistent with recent observations of $N_t N_p / N_d^2$ [166] and the analysis of the intermittency scaling exponent [161], with a peak or dip around $\sqrt{s_{NN}} = 20 - 30\,\text{GeV}$, which could indicate the presence of a critical end point (CEP) in these collisions. Thus, the information entropy can also be regarded as an indication of an alternative observable for studying the QGP phase transition.

3.6 Global polarization of QCD matter

In non-central relativistic heavy ion collisions, huge orbital angular momenta (OAM) and vorticity fields are produced in QGP [167]. These can lead to hadron polarization and spin alignment along the direction of the system OAM through spin-orbit couplings [168–170] or spin–vorticity couplings [171, 172], a phenomenon known as global polarization. Such polarization phenomena in relativistic heavy ion collisions possess some unique features which are different from those of conventional observations. For example, the measurement is not mediated by a magnetic field, as in the well-known Barnett effect of magnetization due to rotation [173]. The global spin polarization of particles is directly observed in relativistic heavy ion collisions, which is not possible in ordinary matter. Also, QGP at very high energies is almost neutral by charge conjugation. However, if it were precisely neutral, the observation of polarization by magnetization would be impossible because particles and antiparticles would have opposite magnetic moments. In fact, Λ and $\bar{\Lambda}$ in relativistic heavy ion collisions at high energy have almost the same mean polarization, suggesting that polarization is a strong interaction driven phenomenon. If the electromagnetic field were responsible for this effect, the signs of its mean spin vector components would be opposite. Hence, for non-relativistic matter, the fact that it is impossible to resolve polarization by rotation and magnetization, is at the very heart of the Barnett effect [173] and its reverse Einstein-de Hass effect [174]. In relativistic matter, because of the existence of antiparticles, the rotation and magnetization effects can be distinguished, and QGP is the first relativistic system through which this distinction has been observed [175].

The global polarization of hyperons can be determined from the angular distribution of hyperon decay products in hyperon's rest frame with respect to the system OAM:

$$\frac{\mathrm{d}N}{\mathrm{d}\cos\theta^*} \propto 1 + \alpha_{\mathrm{H}} P_{\mathrm{H}} \cos\theta^*, \tag{1}$$

where α_{H} is the hyperon decay parameter; P_{H} is the hyperon polarization; and θ^* is the angle between the polarization vector and direction of the daughter nucleon momentum in the hyperon rest frame. Since the system OAM is

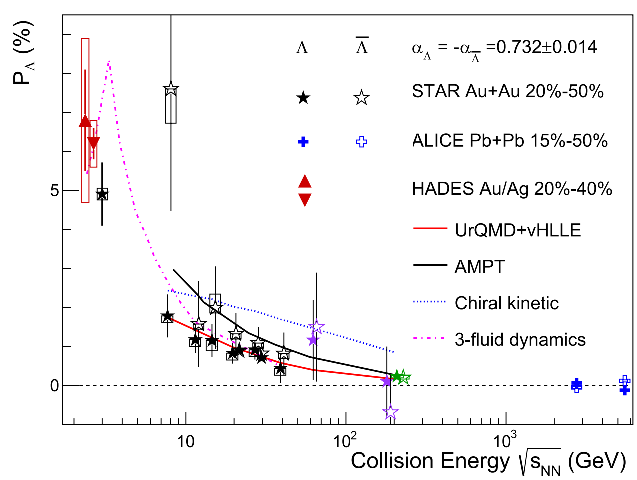

Fig. 22 (Color online) Global Λ and $\bar{\Lambda}$ polarization as a function of $\sqrt{s_{NN}}$ in mid-central heavy ion collisions [175, 177, 179–183]. For clarity, data points of the same collision energy from updated measurements are slightly shifted along the x-axis. Calculations using the hybrid (UrQMD+vHLLE) [184], chiral kinetic transport (Chiral kinetic) [185], and multi-phase transport models [186] are comparable to the higher $\sqrt{s_{NN}}$ data, whereas the hydrodynamics 3-fluid model with different equations of state predicts a sharply rising P_Λ at lower $\sqrt{s_{NN}}$ [187]

perpendicular to the reaction plane, the global polarization can be measured via the distribution of the azimuthal angle of the hyperon decay nucleon in the hyperon rest frame with respect to the reaction plane. The reaction plane is defined by the direction of the incoming nuclei (beam direction) and impact parameter vector ($\hat{b}$) [176]. The reader is referred to [177, 178] for the analysis details and focus on the results presented here.

Figure 22 shows the first measurement of P_{H} at $\sqrt{s_{\mathrm{NN}}} = 62.4$ GeV and 200 GeV in the STAR experiment, which are consistent with zero [179]. The later STAR measurements at $\sqrt{s_{\mathrm{NN}}} = 3$ GeV, 7.7 GeV–39 GeV [175, 181], with higher statistics at $\sqrt{s_{\mathrm{NN}}} = 200$ GeV [177], indicate statistically significant global polarization $P_{\mathrm{H}} > 0$, whereas high-statistics ALICE measurements at $\sqrt{s_{\mathrm{NN}}} = 2.76$ TeV and 5.02 TeV demonstrate a P_{H} consistent with zero at the LHC energies [180]. The P_{H} is observed to increase with collision centrality, in agreement with the increasing system OAM from central to peripheral collisions. Figure 22 also shows a measurement of Λ polarization shifting to lower energies of Au+Au collisions at $\sqrt{s_{\mathrm{NN}}} = 2.4$ GeV and Ag+Ag collisions at $\sqrt{s_{\mathrm{NN}}} = 2.55$ GeV in the HADES experiment [182]. An increasing trend of P_{H} with decreasing $\sqrt{s_{\mathrm{NN}}}$ is observed. The collision energy dependence of experimental data can be reasonably described by theoretical calculations, as displayed in the figure, including hydrodynamic [184, 187], transport [186], and chiral kinetic simulations [185]. Some models also predict that P_{H} would vanish at $\sqrt{s_{\mathrm{NN}}} = 2m_{\mathrm{N}}$, and thus P_{H} may peak around 3.0 GeV [187, 188]. Investigating the dependencies of P_{H} on the hyperon transverse momentum p_{T} and rapidity y is also interesting, as different models display opposite trends for the high rapidity region [185, 189]. The available measurements mostly cover midrapidity, and the observed P_{H} versus p_{T} and y is constant within a margin of uncertainty. Future measurements in the large rapidity region would be of special interest, particularly after the STAR forward detector upgrade. There are also discussions on the collision system dependence of P_{H}, for example in smaller colliding systems [190]. Recently, the STAR experiment measured the Λ global polarization in isobar Ru+Ru and Zr+Zr collisions at $\sqrt{s_{\mathrm{NN}}} = 200$ GeV and observed Λ polarization along the beam direction relative to the second and third harmonic event planes originating from the local vorticity [191].

All particles and antiparticles of the same spin should have the same global polarization assuming that OAM is the only driving source of polarization. A difference can arise from the effects of the initial magnetic field, given the fact that particles and their antiparticles have opposite magnetic moments. In addition, different particles can be produced at different times or regions as the system freezes out, or through meson-baryon interactions. The measurements of

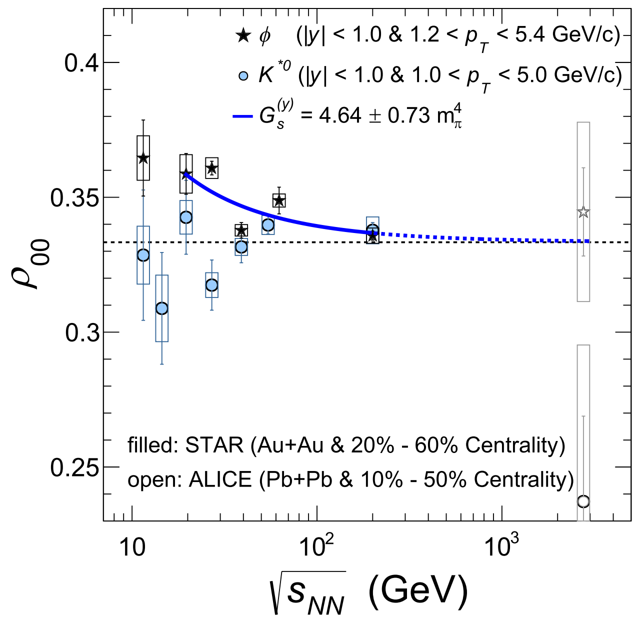

Fig. 23 (Color online) Global spin alignment of ϕ and K^{*0} vector mesons in heavy ion collisions. The measured matrix element ρ_{00} as a function of beam energy for the ϕ and K^{*0} vector mesons within the indicated windows of centrality, transverse momentum (p_{T}), and rapidity (y). The open symbols indicate the ALICE results [194] for Pb+Pb collisions at 2.76 TeV and p_{T} values of 2.0 GeV/c and 1.4 GeV/c for the ϕ and K^{*0} mesons, respectively. The blue solid curve is a fit to the data in the range of $\sqrt{s_{\mathrm{NN}}} = 19.6$ GeV to 200 GeV, based on a theoretical calculation using the ϕ-meson field [195]. Parameter sensitivity of ρ_{00} to the ϕ-meson field is shown in [196]. The blue dashed line is an extension of the solid curve for the fitted parameter $G_s^{(y)}$. The black dashed line represents $\rho_{00} = 1/3$

Λ and $\bar{\Lambda}$ polarization in $\sqrt{s_{\mathrm{NN}}} = 7.7 - 39$ GeV show no difference within current uncertainties. Therefore, to establish the global nature of the polarization, it is very important to measure the polarization of different particles, and if possible, particles of different spins.

Global polarization leaves its imprint on vector mesons such as $\phi(1020)$ and $K^{*0}(892)$. Unlike Λ and $\bar{\Lambda}$ hyperons that can undergo weak decay with parity violation, the polarization of vector mesons cannot be directly measured since they mainly decay through the strong interaction, in which parity is conserved. Nevertheless, the spin state of a spin-1 vector meson can be described by a 3×3 spin density matrix with unit trace [192]. The diagonal elements of this matrix, namely, ρ_{11}, ρ_{00} and ρ_{-1-1}, are probabilities of the spin component and take on the values of 1, 0, and -1, respectively, along a quantization axis, which is selected for the projection of OAM to have well-determined values. When the three spin states have equal probability of being occupied, all three elements are 1/3, and there is no spin alignment. If $\rho_{00} \neq 1/3$, the spin of the vector meson is aligned with the spin quantization direction. For a vector meson decaying into two spin-0 daughters, the angular distribution of one of its decay products in the vector meson rest frame can be written as

$$\frac{\mathrm{d}N}{\mathrm{d}\cos\theta^*} \propto (1-\rho_{00}) + (3\rho_{00}-1)\cos^2\theta^*, \tag{2}$$

where θ^* is defined as in Eq. (1), that is, by the polar angle between the quantization axis and momentum direction of one of the decay products. For our study of global spin alignment, the quantization axis was chosen to be the direction of the system OAM, which is perpendicular to the reaction plane. By fitting the angular distribution of decay products using Eq. (2), one can infer the ρ_{00} value.

The search for global spin alignment of $\phi(1020)$ and $K^{*0}(892)$ mesons for Au+Au collisions at $\sqrt{s_{\mathrm{NN}}} = 200$ GeV started in parallel with the search for Λ polarization. Due to limited statistics at that time, no significant results were reported [193].

Figure 23 presents the $\phi(1020)$ meson spin alignments in Au+Au collisions at beam energies between $\sqrt{s_{\mathrm{NN}}} = 11.5$ GeV and 200 GeV [197]. The STAR measurements presented in Fig. 23 are for centralities between 20% and 60% where a maximum OAM of the collision system is expected. The quantization axis is the normal to the 2nd-order event plane [176] (a proxy for the reaction plane), determined using STAR charged particle information. The ϕ-meson results are presented for transverse momentum 1.2 GeV/$c < p_{\mathrm{T}} <$ 5.4 GeV/c, and ρ_{00} which are significantly above 1/3 for collision energies of 62 GeV and below for this species, indicating finite global spin alignment. The ρ_{00} for ϕ mesons, averaged over beam energies of 62 GeV and below, is 0.3512 $\pm$ 0.0017 (stat.) $\pm$ 0.0017 (syst.). Taking the total uncertainty as the quadrature sum of statistical and systematical uncertainties, our results indicate that the ϕ-meson ρ_{00} is above 1/3 with a significance of 7.4 σ [197].

Figure 23 also presents the beam energy dependence of ρ_{00} for K^{*0} within 1.0 GeV/$c < p_{\mathrm{T}} <$5.0 GeV/c. We observe that the ρ_{00} for K^{*0} is largely consistent with 1/3, in marked contrast to the case for ϕ. The ρ_{00} for K^{*0}, averaged over beam energies of 54.4 GeV and below, is 0.3356 $\pm$ 0.0034 (stat.) $\pm$ 0.0043 (syst.), and the deviation from 1/3 has a $\sim$ 0.42 σ significance [197]. Measurements from the ALICE collaboration for Pb+Pb collisions at $\sqrt{s_{\mathrm{NN}}} =$ 2.76 TeV [194], taken from the data points [194] closest to the mean p_{T} for the range of 1.0 GeV/$c < p_{\mathrm{T}} <$5.0 GeV/c, are also shown for comparison in Fig. 23. They are consistent with 1/3 considering the large statistical uncertainties.

According to the quark coalescence for hadron production in heavy ion collisions, the Λ polarization depends linearly on the quark polarization, whereas the vector meson polarization displays a quadratic dependence [168, 169]. One would therefore expect the polarization for ϕ to be smaller than the one measured for Λ. However, the measured ρ_{00} of ϕ is orders of magnitude larger than the expected from the same vorticity that caused the measured Λ and $\bar{\Lambda}$ polarizations in the same collisions. Contributions from electromagnetic fields and other possible conventional mechanisms are also orders of magnitude smaller than expected from the data [195, 198–200]. However, a new mechanism of vector meson spin alignment due to a strong force field is capable of describing both the ρ_{00} of ϕ and K^{*0} [196], pointing out that the difference of Λ polarization and vector meson spin alignment can be understood as follows. The Λ polarization provides information on the mean values of quark polarization, whereas the ρ_{00} provides information on the correlation of quark and antiquark polarization inside the vector meson [201]. Thus measurements of vector meson spin alignment provide a novel way for probing the quark spin correlations. This information may also be accessible via the measurements of hyperon–hyperon and hyperon-antihyperon spin correlations [201]. These different scenarios open an exciting discovery potential for the spin polarization measurements. For example, the strong force correlation may be expected to provide new information about the short distance structure of QGP and the nature of QCD phase diagram [202, 203].

3.7 Light cluster formation

Light nuclei and hypernuclei are loosely bound objects of nucleons and hyperons with binding energies of several MeV. Their formation in heavy ion collisions provides important information on the properties of nuclear matter at high densities and temperatures, such as the nucleon–nucleon/hyperon interactions. The equation of state may offer insights into the inner structure of compact stars.

The production of light nuclei in relativistic nucleus-nucleus collisions has been studied since the early 1960s [204], and their production mechanisms are still being debated [205–207]. The thermal/statistical and nucleon coalescence models are two widely recognized and effective methods for explaining the production of light nuclei in high-energy heavy ion collisions. In the thermal model, the formation of light nuclei is similar to that of hadrons, with the yields calculated based on particle masses and the thermodynamic properties near the chemical freeze-out of the collision system [205, 206]. The coalescence model assumes that light nuclei emerge through a combination of nucleons coming close to each other at the time of kinetic freeze-out [208–210].

Based on the coalescence model, the compound yield ratio $N_{\mathrm{t}} \times N_{\mathrm{p}}/N_{\mathrm{d}}^2$ of tritons (N_{t}), deuterons (N_{d}), and protons (N_{p}) is predicted to be sensitive to the neutron density fluctuations, making it a promising observable to search for

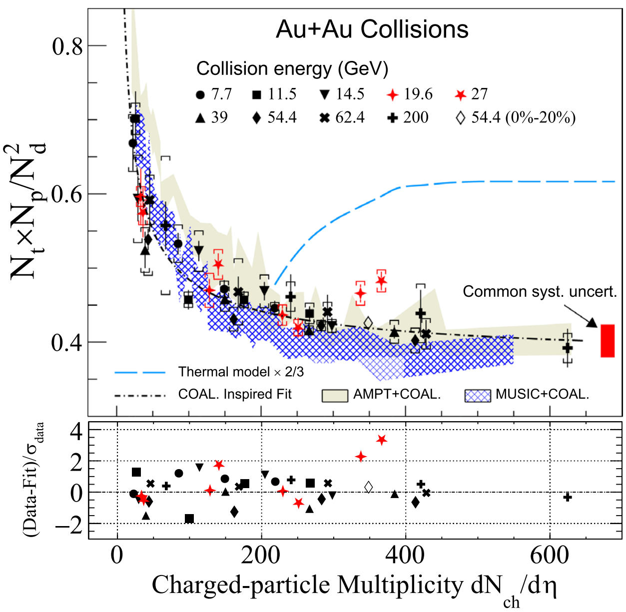

Fig. 24 (Color online) The yield ratio $N_{\mathrm{t}} \times N_{\mathrm{p}}/N_{\mathrm{d}}^2$ as a function of charged particle multiplicity $\mathrm{d}N_{\mathrm{ch}}/\mathrm{d}\eta$ ($|\eta| < 0.5$) in Au+Au collisions at $\sqrt{s_{\mathrm{NN}}} = 7.7 - 200$ GeV for various collision centralities [166]. The black dot-dashed line denotes the coalescence-inspired fit. The significance of the deviation relative to the fit is shown in the lower panel. The results calculated from the thermal model are shown as the blue long-dashed line. Calculations from AMPT and MUSIC+UrQMD hybrid models are shown as shaded bands [211]

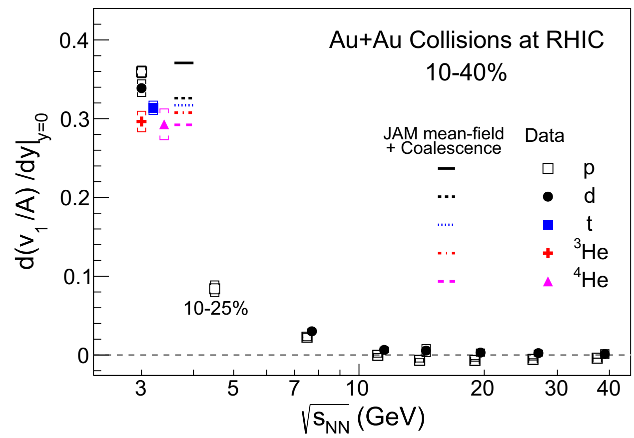

Fig. 25 (Color online) Light nucleus v_1 slopes $\mathrm{d}v_1/\mathrm{d}y|_{y=0}$ scaled by the atomic mass number as a function of collision energy in 10–40% mid-central Au+Au collisions [216–218]. For clarity, the data points are shifted horizontally. Results of the JAM model in the mean field mode plus coalescence calculations are shown as color bars

in the signature of CEP and/or a first-order phase transition in heavy ion collisions [212–215]. The expected signature of CEP is its non-monotonic variation as a function of collision energy.

Figure 24 shows the charged particle multiplicity $\mathrm{d}N_{\mathrm{ch}}/\mathrm{d}\eta$ ($|\eta| < 0.5$) dependence of the yield ratio $N_{\mathrm{t}} \times N_{\mathrm{p}}/N_{\mathrm{d}}^2$ in Au+Au collisions at $\sqrt{s_{\mathrm{NN}}} = 7.7 - 200$ GeV, combining all centrality bins [166]. The yield ratio exhibits a charge-particle multiplicity scaling, regardless of collision energy and centrality. The shaded bands are the corresponding results from the calculations of hadronic transport AMPT and MUSIC+UrQMD hybrid models, in which neither critical point nor first-order phase transition is included. These two models are employed to generate the nucleon phase space at kinetic freeze-out, with light nuclei forming via nucleon coalescence. The overall trend of the experimental data is well described by the model calculations. The light blue dashed line is the result calculated from the thermal model at chemical freeze-out ($T_{\mathrm{ch}} = 157$ MeV at 200 GeV) for central Au+Au collisions, which overestimates the experimental data by more than a factor of two at $\mathrm{d}N_{\mathrm{ch}}/\mathrm{d}\eta \sim 600$ which could be due to the effects of hadronic rescattering during hadronic expansion. The black dot-dashed line is a fit to the data based on the coalescence model. The lower panel of Fig. 24 shows that most of the measurements are within a significance of 2 σ from the coalescence baseline, except for the enhancements observed for the yield ratios from the 0–10% most central Au+Au collisions at 19.6 GeV and 27 GeV with a significance of 2.3 σ and 3.4 σ, respectively. Notably, in the net-proton higher moments and charged particle intermittency measurements, non-monotonic behaviors are observed around a collision energy of $\sqrt{s_{\mathrm{NN}}} = 20$ GeV. Further studies on dynamical modeling of heavy ion collisions based on a realistic equation of state are required to confirm that the enhancements are due to large baryon density fluctuations near the critical point. These systematic measurements of triton yields and yield ratios over a broad energy range provide important insights into the production dynamics of light nuclei, enhancing our understanding of the QCD phase diagram.

Similar to the number of constituent quark scaling of hadron flow, the light nuclei flow is expected to exhibit an approximate scaling with the mass number A scaling under the coalescence assumption [97]

$$v_n^A(p_{\mathrm{T}}, y)/A \approx v_n^p(p_{\mathrm{T}}/A, y). \tag{3}$$

However, unlike quarks, whose flow cannot be directly measured, both proton and light nuclei flow can be directly measured in experiments to validate the coalescence model. Figure 25 shows the light nucleus v_1 slopes $\mathrm{d}v_1/\mathrm{d}y|_{y=0}$, which are utilized to characterize the strength of v_1, scaled by the atomic mass number, as a function of collision energy from the $\sqrt{s_{\mathrm{NN}}} = 3 - 40$ GeV STAR experiment [216–218]. Overall, the $\mathrm{d}v_1/\mathrm{d}y|_{y=0}$ decreases monotonically with increasing collision energy for both protons and light nuclei. At $\sqrt{s_{\mathrm{NN}}} = 3.0$ GeV, the $\mathrm{d}v_1/\mathrm{d}y|_{y=0}$ follow an approximate scaling with the atomic mass number A. The transport model calculation with a baryon mean field and a coalescence afterburner qualitatively reproduces the measurements for both protons and light nuclei, as indicated by the short lines near the data points. The results indicate that the light nuclei are likely formed via the coalescence of nucleons in $\sqrt{s_{\mathrm{NN}}} = 3.0\,\mathrm{GeV}$ Au+Au collisions, with the baryonic interactions dominating the collision dynamics [216]. At $\sqrt{s_{\mathrm{NN}}} = 7.7\,\mathrm{GeV}$, the A scaling still holds for v_1 of the deuteron. However, in moving to higher energies, the $\mathrm{d}v_1/\mathrm{d}y|_{y=0}$ values for protons become negative, while the corresponding value for deuterons is still positive albeit with larger uncertainties [217]. This discrepancy in the scaling behavior of light nuclei $\mathrm{d}v_1/\mathrm{d}y|_{y=0}$ at energies below 7.7 GeV and above 11.5 GeV may indicate a different production mechanism or system evolution, as the QGP is expected to form at higher energies, and interactions occur at the partonic level [91, 92].

Hypernuclei are nuclei containing at least one hyperon. As such, they are excellent experimental probes to study the hyperon–nucleon (Y–N) interaction [219, 220], an important ingredient in the EOS of dense nuclear matter [221, 222]. Similar to light nuclei production in heavy ion collisions, statistical thermal hadronization [205] and coalescence models [221] have been proposed to describe hypernuclei formation. Although thermal model calculations primarily depend only on the freeze-out temperature and the baryon chemical potential, the Y–N interaction plays an important role in the coalescence approach through its influence on the dynamics of hyperon transportation in the nuclear medium, as well as its connection to the coalescence criterion for hypernuclei formation from hyperons and nucleons [221].

Figure 26 shows the ${}^{3}_{\Lambda}\mathrm{H}$ and ${}^{4}_{\Lambda}\mathrm{H}$ midrapidity yields for central Au+Au collisions of $\sqrt{s_{\mathrm{NN}}} = 3.0\,\mathrm{GeV}$ in comparison with the measurements at LHC, with the insets showing the $\mathrm{d}N/\mathrm{d}y \times$B.R. as a function of B.R.. We observe that the ${}^{3}_{\Lambda}\mathrm{H}$ yield in Au+Au collisions at $\sqrt{s_{\mathrm{NN}}} = 3.0\,\mathrm{GeV}$ is significantly enhanced compared to the yield at LHC, likely driven by the increase in baryon density at low energies. Calculations from the thermal model [205], which adopt the canonical ensemble for strangeness, mandatory at low beam energies, are compared with the experimental data. Interestingly, while the ${}^{3}_{\Lambda}\mathrm{H}$ yields at 3.0 GeV and 2.76 TeV are well described by the model, the ${}^{4}_{\Lambda}\mathrm{H}$ yield is underestimated by approximately a factor of four. Coalescence calculations using the Dubna cascade model (DCM), which is an intra-nuclear cascade model for describing the dynamical stage of the reaction [221], are consistent with the ${}^{3}_{\Lambda}\mathrm{H}$ yield while underestimating the ${}^{4}_{\Lambda}\mathrm{H}$ yield, whereas coalescence using JAM calculations is consistent with both. Note that in the DCM model, the same coalescence parameters are assumed for two hypernuclei, whereas in the JAM model, parameters are tuned separately for ${}^{3}_{\Lambda}\mathrm{H}$ and ${}^{4}_{\Lambda}\mathrm{H}$ to fit the data. The calculated hypernuclei yields are expected to depend on the choice of the coalescence parameters [221]. The

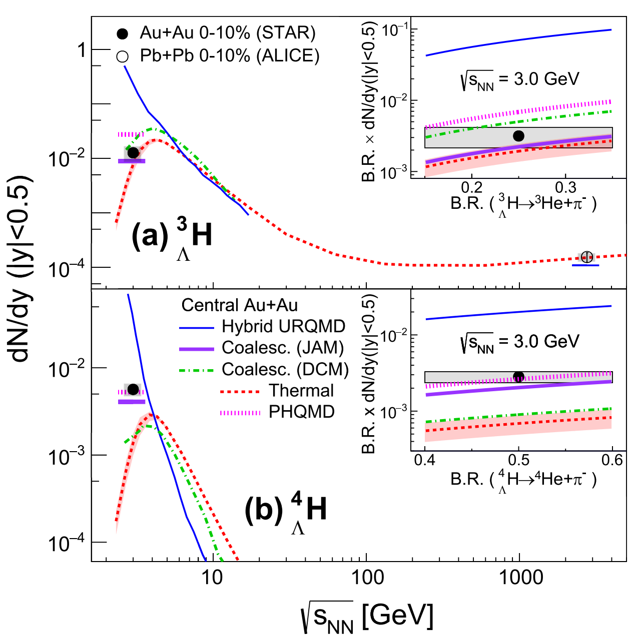

Fig. 26 (Color online) Beam energy dependent **a** ${}^{3}_{\Lambda}\mathrm{H}$ and **b** ${}^{4}_{\Lambda}\mathrm{H}$ yields at $|y| < 0.5$ in central heavy ion collisions compared to theoretical model calculations. The data points assume a branching ratio (B.R.) of 25(50)% for ${}^{3}_{\Lambda}\mathrm{H}$ (${}^{4}_{\Lambda}\mathrm{H}$) $\rightarrow$ ${}^{3}\mathrm{He}$ (${}^{4}\mathrm{He}$) + π^-. The insets show their yields at $|y| < 0.5$ times the B.R. as a function of B.R. [223]

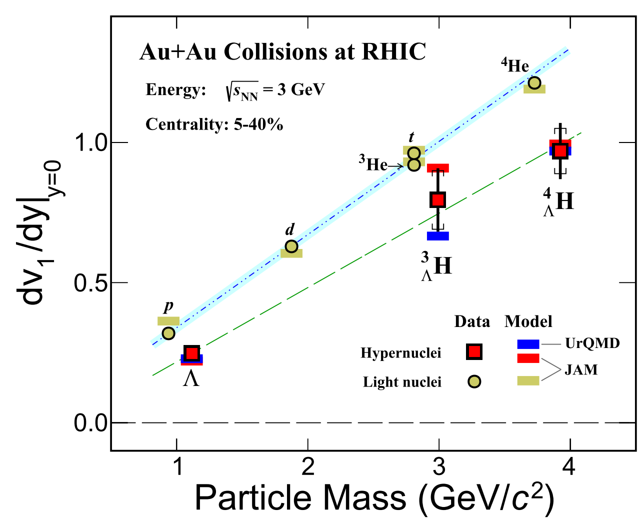

Fig. 27 (Color online) Mass dependence of light nuclei and hypernuclei v_1 slopes $\mathrm{d}v_1/\mathrm{d}y|_{y=0}$ from the $\sqrt{s_{\mathrm{NN}}} = 3\,\mathrm{GeV}$ 5%-40% centrality Au+Au collisions [225].The dashed lines are the results of a linear fit to the measured light nuclei and hypernuclei $\mathrm{d}v_1/\mathrm{d}y|_{y=0}$, respectively. The calculations of transport models plus coalescence afterburner are shown as gold and red bars for the JAM model, and blue bars for the UrQMD model

recent calculations from parton-hadron-quantum-molecular-dynamics (PHQMD) [224], a microscopic transport model which utilizes a dynamical description of hypernuclei formation, are consistent with the measured yields within a margin of uncertainty. Compared to the JAM model which adopts a baryonic mean field approach, baryonic interactions in PHQMD are modeled by density-dependent 2-body baryonic potentials. Meanwhile, the UrQMD-hydro hybrid model overestimates the yields at 3.0 GeV by an order of magnitude [223]. STAR measurements possess the capability to distinguish between different production models and provide new baselines for the strangeness canonical volume in thermal models and coalescence parameters in transport plus coalescence models. Such constraints can be utilized to improve the model estimation of the production of exotic strange matter in the high baryon density region.

The STAR experiment reported the first observation of the v_1 of hypernuclei ${}^{3}_{\Lambda}$H and ${}^{4}_{\Lambda}$H in 3.0 GeV Au+Au collisions [225], as shown in Fig. 27. The mass dependence of $\mathrm{d}v_1/\mathrm{d}y|_{y=0}$ for Λ and hypernuclei is similar to that of light nuclei, increasing linearly with the particle mass, following a baryon mass number scaling. Although the $\mathrm{d}v_1/\mathrm{d}y|_{y=0}$ values for hypernuclei are systematically lower compared to those for nuclei of equivalent mass numbers, this discrepancy may be attributed to the fact that the $\mathrm{d}v_1/\mathrm{d}y|_{y=0}$ for Λ is lower than that for protons. The calculations using the transport model plus an afterburner qualitatively reproduce the data within uncertainties, suggesting that the hypernuclei are produced via coalescence of hyperon and light nuclei core in such heavy ion collisions. If hypernuclei are formed through the coalescence process, both their v_1 and yield can be affected by the interactions involving hyperons and nucleons (*Y*-*N*), which are essential for understanding the inner structure of compact stellar objects. The linear fits to the extracted $\mathrm{d}v_1/\mathrm{d}y|_{y=0}$ in Fig. 27 show comparable slopes considering uncertainties for both light nuclei and hypernuclei, but their central values are slightly different. This difference may originate from the differences in nucleon–nucleon and *Y*-*N* interactions. Thus, more precise measurements with increased statistics, especially at high baryon density, will be crucial in elucidating the hypernuclei production mechanisms and hyperon-nucleon interactions in the future.

3.8 Heavy flavor hadron production

Heavy flavor hadrons are hadrons with at least one constituent heavy flavor quark. They are penetrating probes of QGP. Heavy flavor quarks are predominantly produced through initial hard scattering processes in heavy ion collisions owing to their large masses. These initial hard processes occur before the formation of QGP. Consequently, heavy flavor quarks experience the entire evolution of QGP created in heavy ion collisions. Heavy flavor quarks interact with the deconfined quarks, mainly light flavor quarks, and gluons when they transit QGP and approach thermalization. Their thermal relaxation time is expected to be comparable to or longer than the lifetime of the QGP created in heavy ion collisions. Heavy flavor quarks may acquire collectivity from the collectively expanding hot medium. The collectivity of heavy flavor quarks is sensitive to the hot medium transport properties, especially to the parameter known as the heavy flavor diffusion coefficient $\mathcal{D}_s$ [226].

Significant elliptic flow (v_2) was observed for charmed meson D^0 in Au+Au collisions at $\sqrt{s_{\mathrm{NN}}} = 200$ GeV by the STAR collaboration [96]. The D^0s are fully reconstructed via the two-body decay of charged pions and kaons with a branching ratio of $(3.95 \pm 0.03)\%$. The random combinatorial background of pions and kaons originating from primary vertices are significantly suppressed by precise measurements of the distance of closest approach (DCA) between tracks and primary vertex owing to the relatively large $c\tau$ of D^0 mesons (≈ 123 μm). The precise measurements of DCA were provided by the heavy flavor tracker installed in STAR during 2014 and 2016. The v_2 results for D^0 mesons in 10–40% central Au+Au collisions at $\sqrt{s_{\mathrm{NN}}} = 200\,\mathrm{GeV}$ are compared with those of light flavor hadrons ($\mathrm{K_S}$, Λ, Ξ^-) [227]. At $p_\mathrm{T} < 2$ GeV/c, the v_2 for D^0 mesons is found to be smaller than that of light flavor hadrons, exhibiting the mass-ordering behavior expected from hydrodynamics. At $p_\mathrm{T} > 2$ GeV/c, D^0 v_2 is consistent with that of light flavor mesons such as $\mathrm{K_S}$. The comparison of v_2/n_q as a function of $(m_\mathrm{T} - m_0)/n_q$, where n_q is the number of constituent quarks in a hadron, shows that among these hadrons D^0 elliptic flow follows the universal trend as in light hadrons. These comparisons indicate that charm quarks acquire significant flow through interaction with the strongly coupled QGP created in 10–40% Au+Au collisions at the top energy RHIC. Recent phenomenological models constrained by the D^0 v_2 measurement as well as measurements of heavy flavor quarks v_2 using single electrons from heavy flavor hadron decays (HFE) suggest that the dimensionless charm quark spatial diffusion coefficient $2\pi T\mathcal{D}_s$ falls within the range of 2–5 in the vicinity of the critical temperature ([228] and references therein). This value is consistent with theoretical calculations from the quenched lattice QCD within large uncertainties. The dependence of the heavy flavor quarks diffusion coefficient D_s on heavy flavor quark momentum, as well as on temperature and baryon chemical potential of QGP is yet to be determined. The measurements of heavy flavor quarks collectivity in Au+Au collisions at energies below the RHIC top energy enabled by the RHIC BES program can shed new light on the temperature and baryon chemical potential dependence of the QGP transport parameter $\mathcal{D}_s$.

The elliptic flow of heavy flavor hadrons from RHIC BES program was measured in Au+Au collisions at

$\sqrt{s_{NN}}$ = 27 GeV, 39 GeV, 54.4 GeV, and 62.4 GeV [229, 230]. The 39 GeV and 62.4 GeV data were collected in 2010 during the first phase of the RHIC BES program. The number of events used for the analyses were 87 and 38 million, respectively. The 27 GeV and 54.4 GeV data were collected in 2017 and 2018 between the first and second phases of the RHIC BES program. The number of events passing the event-level criterion were 240 and 570 million, respectively. With an order of magnitude difference of the number of events, combined with the significant energy dependence of heavy flavor hadron production cross section, the precision of the measurements at different energies varies considerably. The results from the 54.4 GeV collisions have the best precision. While the full reconstruction of heavy flavor hadrons in these data is not possible because of a lack of silicon vertex devices, the electrons from heavy flavor hadron decays are used as proxy for the heavy flavor hadrons. Electrons are identified using the inverse velocity calculated from the path length measured by the STAR TPC, with the TOF measured by the vertex position detector providing the start time measurement and the TOF detector providing stop time measurement. The electron candidates are further selected by the ionization energy loss in the TPC gas. The number of electrons are corrected for purity. Photonic electrons (PE) are the dominant source of background for heavy flavor decay electrons. These photonic electrons are produced via Dalitz decay of light mesons such as π^0 and η and photon conversion in the detector material. The yield of non-photonic electrons (NPE) is calculated as follows:

$$N^{\mathrm{NPE}} = N^{\mathrm{INC}} - N^{\mathrm{PE}}, \tag{4}$$

where N^{INC} and N^{PE} represent the yield of inclusive and photonic electrons, respectively. The PE candidates are selected via the invariant mass distribution of inclusive electron candidates and partner electrons from the same event. The yield of photonic electrons can be expressed as:

$$N^{\mathrm{PE}} = \left(N^{\mathrm{UL}} - N^{\mathrm{LS}}\right)/\varepsilon, \tag{5}$$

where N^{UL} and N^{LS} are the raw yield of unlike- and like-sign pairs, respectively, and ε is the partner electron acquiring efficiency. The v_2 of inclusive electron and photonic electrons is extracted using the event plane η-sub method. The v_2 of NPE is calculated by:

$$N^{\mathrm{NPE}} v_2^{\mathrm{NPE}} = N^{\mathrm{INC}} v_2^{\mathrm{INC}} - N^{\mathrm{PE}} v_2^{\mathrm{PE}} - \sum f_{\mathrm{h}} \times N^{\mathrm{INC}} v_2^{h}, \tag{6}$$

where v_2^{INC}, v_2^{PE}, and v_2^{h} are the v_2 of inclusive electrons, photonic electrons, and hadrons contaminated by inclusive electron candidates, respectively; f_{h} is the hadron contamination fraction.

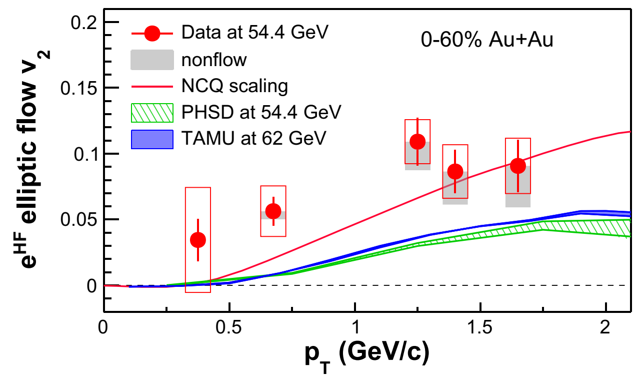

Fig. 28 (Color online) v_2 as a function of p_{T} for heavy flavor decay electrons at midrapidity in Au+Au collisions at $\sqrt{s_{\mathrm{NN}}}$ = 54.4 GeV [229], compared with TAMU [231] and PHSD [232, 233] model calculations

In addition to photonic electrons, other major background sources for heavy flavor decay electrons are from the decay of kaons (K_{e3}) and vector mesons (ρ, ω, and ϕ), which are eliminated using the following equation:

$$v_2^{\mathrm{HFE}} = v_2^{\mathrm{NPE}}(1 + f_{\mathrm{K}_{e3}} + f_{\mathrm{VM}}) - f_{K_{e3}} \times v_2^{K_{e3}} + f_{\mathrm{VM}} \times v_2^{\mathrm{VM}}, \tag{7}$$

where $f_{\mathrm{K}_{e3}}$ and f_{VM} are the estimated yield ratios of electron decays of kaons and vector mesons, respectively, with respect to HFE. The residual non-flow contribution is estimated according to the HFE-hadron correlation in p+p collisions and hadron multiplicity in Au+Au collisions.

Figure 28 shows the elliptic flow coefficient v_2 of heavy flavor decay electrons as a function of p_{T} at midrapidity ($|y| < 0.8$) in Au+Au collisions at $\sqrt{s_{\mathrm{NN}}}$ = 54.4 GeV. The error bars and boxes depict statistical and systematic uncertainties, respectively. The hatched areas indicate the estimated non-flow contributions. Significant v_2 is observed at 0.5 GeV/c < p_{T} < 2 GeV/c; the average v_2 in the p_{T} range of 1.2 GeV/c to 2.0 GeV/c is 0.094 ± 0.008 (stat.) ± 0.014 (syst.), whereas the estimated upper limit of non-flow is only 0.02. The red curve represents the projected charm quark decay v_2 assuming that open charm hadron v_2 follows NCQ scaling along with other light hadrons. Because charm quark is the dominant contributor of HFE in this p_T range, the significant v_2 and the consistency between the data and the red curve indicate that charm quarks interact with the hot medium and may reach local thermal equilibrium in Au+Au collisions even though the center-of-mass energy is nearly a factor of four lower than the RHIC top energy.

The two bands shown in Fig. 28 are calculated using two phenomenological models, TAMU [231] and PHSD [232, 233]. Both models assume that heavy flavor quarks interact with the QGP medium elastically. This assumption is generally accepted in the low p_T region. The elastic scattering is implemented in different ways in the two models. In the TAMU model, the microscopic elastic interaction between heavy flavor quarks and quarks/gluons in the hot, dense medium are evaluated using non-perturbative T-matrix calculations. The heavy flavor quark transport coefficient calculated is then fed into macroscopic Langevin simulation of heavy quark diffusion through the background medium and modeled by ideal 2+1D hydrodynamics. In the PHSD model, heavy flavor quarks interact with the off-shell massive partons in the QGP medium. The masses and widths of the partons in the QGP medium and the scattering probability are provided by the dynamical quasi-particle model. In both models, the heavy flavor quarks hadronize through both coalescence and fragmentation. In the PHSD model, the hadronized heavy flavor hadrons subsequently interact with other hadrons in the hadronic phase. Although the calculations from both TAMU and PHSD models are systematically lower than the measurements, the deviation is only $1-2\,\sigma$ at $p_T > 0.5$ GeV/c when considering the estimated upper limit of non-flow contribution. Furthermore, neither model considers the contribution from charm baryons, whose yield is measured to be evenly enhanced in heavy ion collisions relative to that of mesons [234]. This contribution will slightly increase HFE v_2 at $p_T > 1$ GeV/c.

Heavy quarkonium is a bound state of heavy flavor quark and its antiquark. The pairs of heavy flavor quark and its antiquark are produced predominantly by the initial scattering in heavy ion collisions and are tightly bound together, which makes them less sensitive to interactions with other particles. However, it is believed that the color potential of the bound states is subject to modification when QGP is formed, resulting in the dissociation of heavy quarkonium [242–245]. The suppression of quarkonium yield in heavy ion collisions arising from a modification of the potential is considered as the 'smoking-gun' signature of deconfinement in QGP. This suppression is sensitive to the temperature profile of QGP because the modification of the potential between a heavy quark and its antiquark in QGP is sensitive to the temperature of the medium.

The suppression of J/ψ in heavy ion collisions was extensively studied in experiments at CERN SPS [246]. The production yield of quarkonium in heavy ion collisions was found to be affected by cold nuclear matter (CNM) effects. Suppression of the J/ψ yield beyond the expected CNM effects was observed in central Pb+Pb collisions at 17.3 GeV based on the results from proton and nucleus collisions and was considered as evidence of deconfinement in QGP [235].

However, the first quarkonium measurement in heavy ion collisions at RHIC was very puzzling. The J/ψ suppression, quantified by the nuclear modification factors, and its centrality dependence measured in Au+Au collisions at $\sqrt{s_{NN}} = 200$ GeV [247] was found to be consistent with that observed in Pb+Pb collisions at $\sqrt{s_{NN}} = 17.3$ GeV. However, J/ψ suppression is expected to be stronger at higher collision energies where the initial temperature is believed to be systematically higher. Furthermore, the suppression was observed to be significantly stronger at forward rapidity than at midrapidity, where the energy density is believed to be higher compared with that of forward rapidity. An additional production mechanism, (re)combination of charm quark and anticharm quark in the QGP medium, was proposed to solve this problem [248, 249]. Unlike the static and dynamic screening of the potential between heavy quark and its antiquark, the (re)combination mechanism can enhance quarkonium yield in heavy ion collisions. Because the yield of quarkonium from the (re)combination mechanism is approximately proportional to the square of total heavy quark cross section, which exhibits a significantly increasing trend as the energy of collisions increases, the contribution from (re)combination mechanism should display a clear center-of-mass energy dependence. The RHIC BES program provides a unique opportunity for varying the initial temperature and number of charm quark pairs in an event, which should shed new light on the production mechanism of quarkonium in heavy ion collisions.

The data for the J/ψ production study were collected during the RHIC BES in 2010 by the STAR experiment at $\sqrt{s_{NN}} = 39$ GeV and 62.4 GeV [236]. The total number of minimum bias triggered events are 182 million and 94 million, respectively. The J/ψs are reconstructed considering their decays into electron-positron pairs. The electron daughters are identified by combining the information from the STAR TPC and TOF. The random combinatorial background is reconstructed using the mixed-event technique. The invariant mass spectrum for unlike-sign pairs from mixed-events are normalized to that for like-sign pairs and subtracted from that for unlike-sign pairs. The combinatorial background-subtracted invariant mass spectrum is fit to the J/ψ template using Monte Carlo simulations plus a linear function for the residual background to extract the J/ψ yields. The nuclear modification factors (R_{AA}) are calculated as follows:

$$R_{AA} = \frac{1}{T_{AA}} \frac{\mathrm{d}^2N_{AA}/\mathrm{d}p_T\mathrm{d}y}{\mathrm{d}^2\sigma_{pp}/\mathrm{d}p_T\mathrm{d}y}, \tag{8}$$

where $\mathrm{d}^2N_{AA}/\mathrm{d}p_T\mathrm{d}y$ is the efficiency and acceptance-corrected J/ψ p_T spectrum measured in A+A collisions; T_{AA} is the nuclear overlap function from Glauber Monte Carlo simulations; and $\mathrm{d}^2\sigma_{pp}/\mathrm{d}p_T\mathrm{d}y$ is the J/ψ production cross section in p+p collisions at the same energy as that of A+A collisions. The cross sections of J/ψ in p+p collisions at $\sqrt{s} = 39$ GeV and 62.4 GeV are derived by interpolating

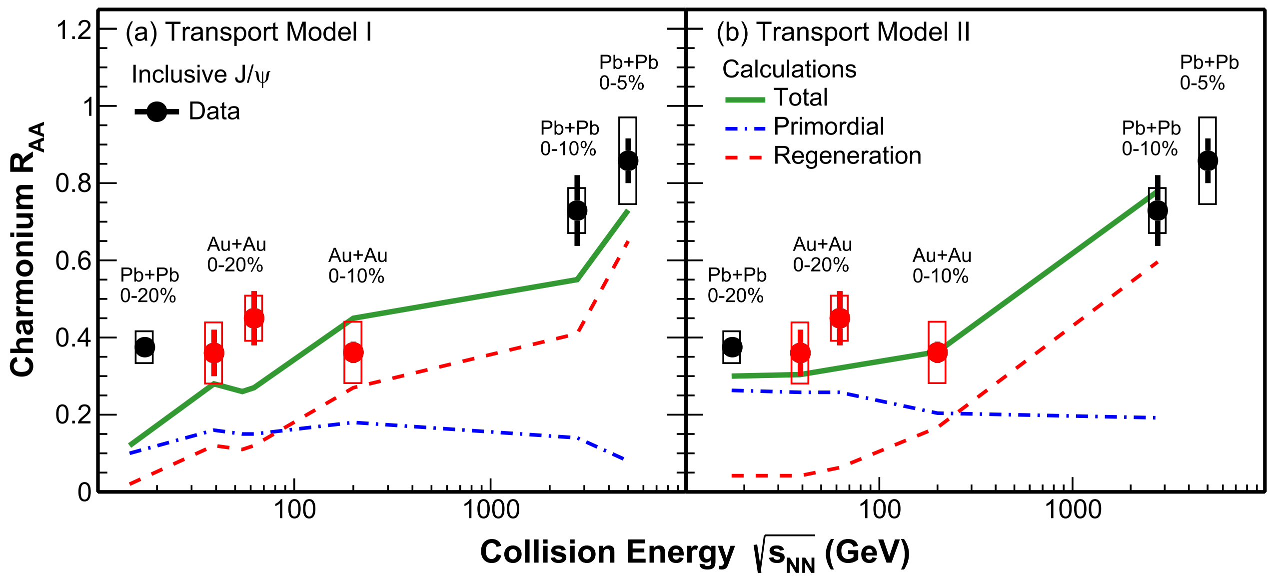

Fig. 29 (Color online) J/ψ nuclear modification factors (R_{AA}) as a function of center-of-mass energy in central heavy ion collisions. The solid circles represent the measurements at SPS, RHIC, and LHC [235–239], and the curves in the left (right) panel reflect the calculations from transport model I [240] (II [241])

J/ψ data worldwide because there are no measurements available for p+p collisions at $\sqrt{s} = 39$ GeV and 62.4 GeV, and previous measurements near these two energies from the Intersecting Storage Ring collider experiments show discrepancies [250].

Figure 29 shows the center-of-mass energy dependence of J/ψ nuclear modification factors measured at midrapidity in central heavy ion collisions from SPS, RHIC, and LHC. The data from RHIC were measured in Au+Au collisions, whereas the data from SPS and LHC were measured in Pb+Pb collisions [235–239]. The error bars and boxes representing statistical and systematic uncertainties indicate that the J/ψ R_{AA} remains constant from $\sqrt{s_{\mathrm{NN}}} = 17.3$ GeV to 200 GeV and substantially increases from RHIC top energy to LHC.

The curves in the left and right panels of Fig. 29 depict the calculations from two transport models [240, 241]. The dot-dashed lines represent the contribution from primordial J/ψs which are affected by the static/dynamic color-screening of the potential in QGP medium and CNM effects, whereas the dashed lines represent the contribution from (re)combination. The solid lines represent the sum of the two components. Although both transport models can describe the data, except for the transport model I at SPS energy, the decomposed contributions from primordial and (re)combination are quite different, further indicating the limitations on the understanding of J/ψ production mechanisms in heavy ion collisions, which should be urgently addressed before extracting the properties of QGP. STAR has collected considerably more data samples at different energies during the second phase of the RHIC BES program. Preliminary results show that J/ψ suppression can be precisely measured in Au+Au collisions at 54.4 GeV, and the suppression measurements can be extended to energies down to 14.6 GeV, an energy below the SPS top energy. These new data will shed new light on the production mechanism of J/ψ in heavy ion collisions.

3.9 Dilepton production

Photons and dileptons (e^+e^- or $\mu^+\mu^-$) emerge at various stages throughout the space-time evolution of the nuclear medium formed in ultra-relativistic heavy ion collisions. As penetrating electromagnetic probes, dileptons remain unaffected by strong interactions, preserving undistorted information on their sources. These sources are manifested differently in various lepton-pair invariant mass (M_{ll}) regions, which are typically categorized into three classes. In the low-mass region (LMR), below the ϕ mass ($M_{ll} < 1.1$ GeV/c^2), contributions predominantly arise from decays of light mesons (π^0, η, ρ^0, ω, ϕ). Investigation of ρ^0 spectra modifications allows probing the in-medium hadronic properties, which are particularly sensitive to mechanisms of chiral symmetry restoration in QCD matter [251]. The expected modifications in dilepton yields within the LMR provide insights into the medium's lifetime and transition from hadronic to partonic degrees of freedom [252]. In the intermediate-mass region (IMR), which lies between the ϕ and J/ψ

masses ($M_{ll} \simeq 1.2 - 3$ GeV$/c^2$), the invariant mass spectrum appears as a continuum arising from both heavy flavor decays and QGP thermal radiation. This provides an opportunity to directly measure the average temperature of the QGP [253] by extracting the inverse slope of the mass spectra, which remain unaffected by the blue shift of the expanding system. In the high mass region (HMR), defined as $M_{ll} \geq 3$ GeV/c^2, primary sources contributing to the dielectron spectrum are heavy flavor/quarkonium decays and the Drell-Yan process. Detailed discussions on the associated physics for HMR have been provided in the preceding section and are not reiterated here.

To achieve precise measurements of the aforementioned dileptons, detectors with large, uniform acceptance and excellent lepton identification capabilities are crucial. The integration of the TOF detector has paved the way for dilepton measurements at STAR. Specifically, by combining timing measurements from the TOF detector with momentum and ionization energy loss ($\langle dE/dx \rangle$) measurements from the TPC, robust identification of electrons over a wide p_T range is achieved. This identification is characterized by high efficiency and purity, facilitating comprehensive dielectron analysis. The identified electron and positron candidates are paired by opposite and same sign charges, called unlike-sign and like-sign pairs, respectively. The like-sign pairs are used to statistically model both the combinatorial and correlated backgrounds. Moreover, the subtraction of decay products from light mesons (known as the "cocktail") is achieved through simulations. These dielectron spectra are of particular interest, as they are anticipated to carry radiation signatures from various stages of heavy ion collisions prior to freeze-out.

The acceptance-corrected excess dielectron mass spectra, following the careful removal of background contributions, have been thoroughly measured by the STAR collaboration across various collision energies [254, 255], as illustrated in Fig. 30. Accompanying these measurements are model calculations [252, 253, 256] depicting the total thermal radiation (solid lines), which consider contributions from both in-medium hadronic processes (dashed lines) and the QGP phase (dotted lines). Remarkably, the model predictions provide a coherent framework for interpreting the measured dielectron spectra across a wide energy range and invariant mass regions. In the low-mass region, the predominant hadronic radiation is primarily attributed to the in-medium ρ broadening, stemming from its interactions with the hadronic medium, particularly baryons. Notably, this model also yields a consistent description of the invariant mass spectrum of dimuon pairs measured by the NA60 experiment at the SPS [257]. The observed in-medium ρ broadening serves as a compelling indicator of the partial restoration of chiral symmetry within the hot QCD medium [258]. However, in the intermediate-mass region, contribution from QGP radiation is anticipated although current measurements still lack precision in this regime. Consequently, the search for and exploration of QGP thermal radiation remain pivotal future endeavors in dilepton experiments at both RHIC and LHC.

To quantitatively compare the excess in the LMR, the integrated excess yield of dielectrons in the mass region

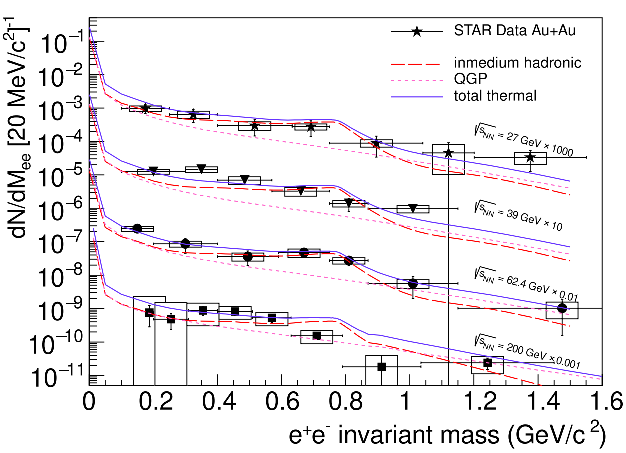

Fig. 30 (Color online) The dielectron invariant mass spectra in Au+Au collisions at $\sqrt{s_{NN}} = 27$ GeV, 39 GeV, 62.4 GeV, and 200 GeV measured by the STAR collaboration [254, 255]. The spectra are shown after subtracting the hadronic background contributions (cocktail), and compared with theoretical model calculations [252, 253, 256]. The theoretical predictions represent the total thermal radiation (blue solid lines), including contributions from both in-medium hadronic processes (red dashed lines) and QGP thermal radiation (red dotted lines). The figure is sourced from [254]

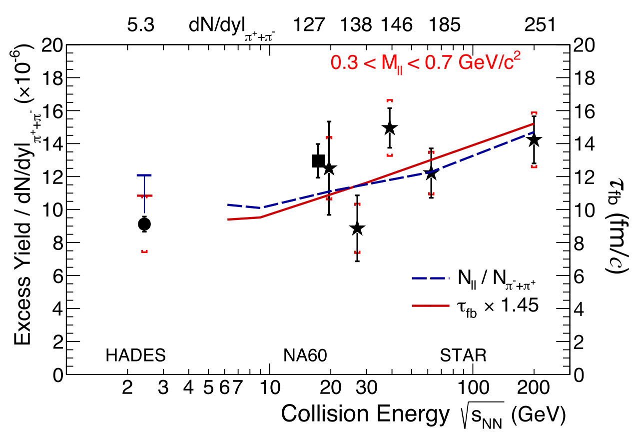

Fig. 31 (Color online) The collision energy dependence of the integrated dielectron yield, normalized by the charged pion yield dN/dy, in the mass region 0.3 GeV/c^2 < M_{ll} < 0.7 GeV/c^2, as measured by HADES [259], NA60 [257], and STAR collaborations [254, 255, 260]. This comparative analysis is supplemented by model calculations of dielectron yields (dashed blue lines) and fireball lifetime (solid red lines) [253]. The figure is sourced from [5]

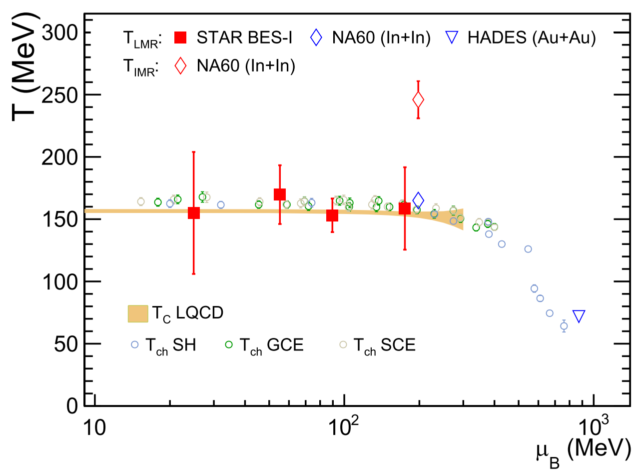

Fig. 32 (Color online) Temperatures versus baryon chemical potential, with temperatures extracted from the in-medium ρ mass spectra of LMR. The earlier QGP stage region from NA60 [261] (diamonds) and LMR from HADES data [259] (inverted triangle) are also depicted. Chemical freeze-out temperatures extracted from statistical thermal models (SH, GCE, SCE) [32, 54] are represented as open circles. The QCD critical temperature T_C at finite μ_B, predicted by LQCD calculations [262], is shown as a yellow band. The figure is adapted from STAR [263]

$0.3\ \mathrm{GeV}/c^2 < M_{ll} < 0.7\ \mathrm{GeV}/c^2$ is normalized to the charged pion yield dN/dy to cancel out the volume effect. Figure 31 shows the collision energy dependence of the integrated dielectron yield, as measured by HADES [259], NA60 [257], and STAR [254, 255, 260] collaborations. The figure also includes theoretical model calculations depicting the dielectron yields (dashed blue lines) and the fireball lifetime (solid red lines) [253]. Impressively, the model provides a commendable description of the energy dependence, illustrating a modest increase from the SPS to the top RHIC energy. This observed increase effectively tracks the fireball lifetime over a broad spectrum of collision energies. Notably, the STAR measurements presented here pertain to BES phase I. However, the subsequent analyses of BES-II data extend these measurements from 19.6 GeV down to 7.7 GeV, providing fresh insights into the properties of the hot medium within the high baryon density regime.

Traditionally, LMR dileptons have been used to explore the in-medium broadening of the ρ meson and its association with chiral symmetry restoration. The impact on the invariant mass distribution of dileptons is often overlooked, as it is considered a trivial thermal factor incorporated into models for data comparison [252, 253]. Recent observations by STAR [263] indicate that the broadening of the ρ meson are so extensive that the LMR dileptons can be used to determine the temperature of the thermal source responsible for LMR radiation. To extract this temperature, a fitting function that combines the in-medium resonance structure with the continuum thermal distribution is applied to the measured mass spectrum. In a vacuum, the mass line shape of the ρ decaying into dileptons is represented by a relativistic Breit–Wigner function, $f^{\mathrm{BW}}(M)$. Within a hot QCD medium, this line shape is modified, multiplied by the Boltzmann factor, $e^{-M/T}$, to account for phase space effects [263]. Furthermore, if ρ is completely dissolved in the medium, its mass spectral structure spreads out and approaches a smooth distribution similar to the dielectron continuum from QGP thermal radiation, described by $M^{3/2}e^{-M/T}$[253]. Figure 32 illustrates temperatures derived from BES-I dielectron data as a function of the baryon chemical potential μ_{B}. The chemical freeze-out temperature T_{ch} and μ_{B} are determined by applying statistical thermal models to the yields of hadron production. T_{ch} from several statistical thermal models and the QCD critical temperature T_{C} from lattice QCD [32, 54, 262] are shown in Fig. 32 as open circles and a shaded band, respectively. Similarly, temperatures extracted from previously published low-mass thermal dielectron spectra [259, 261] are presented. Notably, temperatures extracted from BES-I and SPS LMR closely align with T_{ch} from statistical thermal models and T_{C} from lattice QCD. This alignment suggests that dielectron emission at LMR is mainly influenced by ρ broadening during the phase transition (or mixed phase), and the chemical freeze-out temperature at RHIC BES energies lies at the phase transition boundary. Recent analyses by the STAR collaboration have extracted temperatures from IMR thermal dileptons for Au+Au collisions at $\sqrt{s_{\mathrm{NN}}} = 27$ GeV and 54 GeV, as reported in [263]. The extracted temperatures are significantly higher than those from statistical thermal models and lattice QCD calculations, indicating that IMR dileptons primarily originate from the earlier partonic stage of the collisions. Further details can be found in [263].

In relativistic heavy ion collisions, dileptons emerge not only from hadronic processes but also through the interaction of the intense electromagnetic fields accompanying the colliding ions, known as the Breit–Wheeler process [264, 265]. These fields can be treated as a spectrum of equivalent photons, with the photon flux being proportional to the square of the particle's charge (Z^2), resulting in dilepton production scaling with Z^4. Initially, dilepton production from the two-photon process was studied in ultra-peripheral collisions, where the impact parameter is large enough to avoid hadronic interactions. However, recent observations have shown that such photo-production also occurs in hadronic heavy ion collisions [266, 267], prompting theoretical advancements to describe these processes [268–270]. In events with hadronic overlap, dilepton photo-production occurs alongside hadronic interactions, offering a new method to probe the QGP, especially its electromagnetic properties. Data from peripheral collisions show discrepancies in the p_T^2 distribution between experimental results and theoretical models that do not consider the impact parameter dependence of photon kinematics, suggesting potential alternative origins of p_T^2 broadening, possibly linked to a postulated, trapped magnetic field or Coulomb scattering in the hot and dense medium [266, 267]. However, theoretical calculations that account for impact parameter dependence can explain the observed broadening [271–275], indicating the significant influence of the initial electromagnetic field strength, which were subsequently confirmed by the CMS measurements [276]. Future precision measurements at a toroidal LHC apparatus (ATLAS), STAR, and CMS will further explore these effects, potentially revealing medium induced modifications in dilepton kinematics.

4 Summary and outlook

Since the discovery of the strongly coupled QGP [3] created in high-energy nuclear collisions in the early 2000, scientists have been asking: "What is the structure of the QCD phase diagram in the high baryon density region?" and "Is there a QCD critical point?" Model studies have shown that a first-order phase boundary is expected at the finite baryon density, whereas at vanishing μ_B the transition between the QGP and the hadronic matter is a smooth

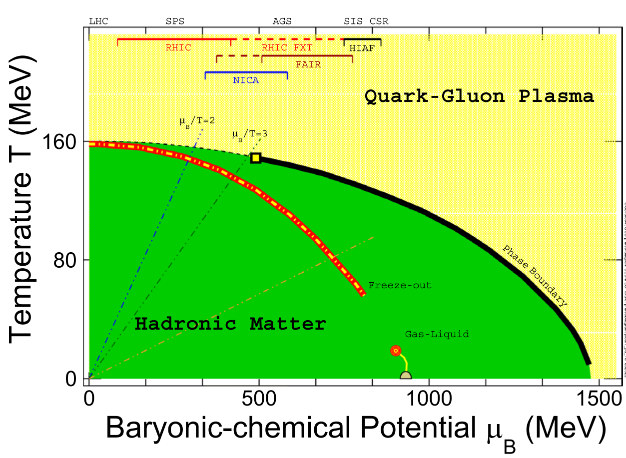

Fig. 33 (Color online) Sketch of the QCD phase diagram. The dashed line represents the smooth crossover region up to $\mu_B/T \leq 3$. The black solid line represents the speculated first-order phase boundary. The empirical thermal freeze-out results from global hadron yield data are shown as the red-yellow line [53]. The liquid–gas transition region that features a second-order critical point is shown by the red-circle, and a first-order transition line is shown by the yellow line, which connects the critical point to the ground state of nuclear matter. The coverage of the RHIC BES program, STAR fixed-target program (FXT), future high-intensity heavy ion accelerator facility (HIAF), and facility for antiproton and ion research (FAIR) are indicated at the top of the figure

crossover. In such a scenario, the first-order phase transition line must end at a critical point and in a finite system such as nuclear collisions, the critical point may turn into a critical region (Fig. 33). More discussions on experimental results and lattice calculations can be found in [4, 277]. The energy scan program at RHIC offers unprecedented high-statistics data on nuclear collisions from the center-of-mass energy of $\sqrt{s_{NN}} = 3$ GeV[1] to 200 GeV, corresponding to the baryonic chemical potential of $\mu_B = 750$ MeV to 20 MeV. Measured data of net-proton high moments from $200 - 39$ GeV, i.e., $\mu_B/T \leq 2$, are consistent with the smooth crossover transition [38] as predicted by the first-principal LGT calculations (Fig. 33). In the lower energy region or at larger net-baryon densities, the collected data allow us to probe the possible QCD critical region.

With the growth of the high-energy heavy ion physics scientific community and the development of state-of-the-art detector technologies boosted by the joint RHIC STAR-China research program, the Chinese scientific program on high baryon density physics will continue to flourish at a number of domestic facilities, from the Heavy Ion Research Facility in Lanzhou-Cooling Storage Ring (HIRFL-CSR) [278] to the HIAF in Huizhou [279]. The RHIC BES program revealed exciting physical dynamics and scientific opportunities in the high baryon density regime. Future investigations of properties of nuclear matter at moderate T and μ_B, created in the heavy ion collisions from sub-GeV/u (at HIRFL) to a few GeV/u (at HIAF) beam energies, are expected to shed new insight on QCD at extreme conditions.

The HIRFL-CSR external-target experiment is a spectrometer covering a wide range of solid angles in the center-of-mass reference frame, currently under construction with support from NSFC and CAS. With promising performance in tracking and particle identification for charged particles, CEE foresees plenty of opportunities in the studies of collision dynamics and nuclear matter properties at densities ranging from ρ_0 to 2.5 ρ_0, with ρ_0 corresponding to the nuclear saturation density [280, 281]. For instance, systematic measurements with CEE can include production of pions, kaons, strangeness baryons, and collective flow to probe the nuclear matter EOS. In parallel, the study of the medium effect of baryon-baryon interactions in the cold nuclear matter near saturation density can be performed using proton-induced collisions at CEE. In addition, measurements of the quark effect by the short-range correlation of nucleons in nuclei can be extended at CEE in the near future [282].

[1] The STAR fixed-target program became a viable scientific endeavor due to the endcap TOF detector constructed by Chinese colleagues for the CBM experiment at FAIR.

The Chinese team is also well positioned in the international community of heavy ion physics. At LHC, we are playing an important role in all experiments including ALICE [99], ATLAS [267], CMS [283], and LHC beauty (LHCb) [284], in exploring the properties of the QCD matter at vanishing net-baryon density. At the high baryon density, the Chinese team has made substantial investments in both CBM experiments at FAIR [285] and multi-purpose detector (MPD) experiments at nuclotron-based ion collider facility (NICA) [286]. Part of the TOF detector successfully employed in STAR BES-II program was constructed in China, with partial support from NSFC, and will be used for the CBM experiment [287] at FAIR. It should be underscored that understanding nuclear matter at high baryon densities offers unique opportunities for studying dynamics related to the inner structure of compact stars [5].

Acknowledgements We are grateful to the STAR collaboration at RHIC. This review is dedicated to Professor Wenqing Shen on the occasion of celebrating his leadership of the Chinese STAR collaboration that led to the development and production of the STAR MRPC TOF detector in China and many physics analyses. All authors contributed equally to this work.

Postscript: This review is dedicated to Professor Wenqing Shen on the occasion of his 80th birthday. Elected as an academician to the Chinese Academy of Sciences in 1999, Prof. Shen served in many academic leadership roles including President of the Shanghai Branch of the Chinese Academy of Sciences, Deputy Director of the National Natural Science Foundation of China, and Chairman of the Shanghai Association of Science and Technology. His research areas range from low-energy nuclear physics to heavy ion physics. In 2000, he led six Chinese institutions to join the RHIC STAR collaboration. Since then, Chinese research teams have participated in a number of RHIC detector upgrades and have led to many outstanding physics analyses [288]. Owing to his leadership, the Chinese nuclear physics community has expanded from traditional low-energy to high-energy nuclear physics. In the two decades after 2000, the Chinese high-energy nuclear physics community has achieved remarkable success. This review article partially reflects the topics covered by the Chinese high-energy nuclear physics team research in the exploration of QCD matter. As we celebrate Professor Shen's 80th birthday, we focus on his leadership and scientific achievements and also reflect on how international collaborations can bring people with diverse cultural backgrounds together and collaborative teams can achieve greater scientific goals than individuals alone. In retrospect, the key elements for the successful RHIC STAR-China project were all present in 2000, as expressed by the Chinese wisdom, "at the right time, in the right place, and with the right people", "天时、地利、人和", in Chinese. We note that Dr. Timothy Hallman, then deputy spokesperson of the STAR collaboration, and Professor Wenqing Shen played critical roles in initiating and fostering the STAR-China project. Over the past 25 years, the project has grown, in hardware contributions to STAR from a small time-of-flight patch to a full-scale time-of-flight detector and time-project-chamber upgrade, along with physics analyses from studies on light hadron spectra to dileptons, quarkonia, hypernuclei, proton spin, and global alignments. The Chinese heavy ion physics community has become one of the most vigorous international communities on studies of the strong interaction and QCD at high temperature and densities. We are grateful to Professor Shen's leadership and vision. We sincerely wish him many happy returns and 寿比南山、福如东海！

References

1. D.J. Gross, F. Wilczek, Ultraviolet behavior of nonabelian gauge theories. Phys. Rev. Lett. **30**, 1343–1346 (1973). https://doi.org/10.1103/PhysRevLett.30.1343
2. H.D. Politzer, Reliable perturbative results for strong interactions? Phys. Rev. Lett. **30**, 1346–1349 (1973). https://doi.org/10.1103/PhysRevLett.30.1346
3. J. Adams, M.M. Aggarwal, Z. Ahammed et al., Experimental and theoretical challenges in the search for the quark gluon plasma: the STAR collaboration's critical assessment of the evidence from RHIC collisions. Nucl. Phys. A **757**, 102–183 (2005). https://doi.org/10.1016/j.nuclphysa.2005.03.085
4. A. Bzdak, S. Esumi, V. Koch et al., Mapping the phases of quantum chromodynamics with beam energy scan. Phys. Rep. **853**, 1–87 (2020). https://doi.org/10.1016/j.physrep.2020.01.005
5. X. Luo, Q. Wang, N. Xu et al. (eds.), *Properties of QCD Matter at High Baryon Density* (Springer, 2022). https://doi.org/10.1007/978-981-19-4441-3
6. M.M. Aggarwal, Z. Ahammed, A.V. Alakhverdyants et al., An experimental exploration of the QCD phase diagram: The search for the critical point and the onset of de-confinement. arXiv:1007.2613
7. E. Cerron Zeballos, I. Crotty, D. Hatzifotiadou et al., A new type of resistive plate chamber: the multigap RPC. Nucl. Instrum. Meth. A **374**, 132–136 (1996). https://doi.org/10.1016/0168-9002(96)00158-1
8. C. Li, J. Wu, H.F. Chen et al., A prototype of the high time resolution MRPC. Chin. Phys. C **25**, 933–936 (2001)
9. J. Adams, M.M. Aggarwal, Z. Ahammed et al., Pion, kaon, proton and anti-proton transverse momentum distributions from p + p and d + Au collisions at $\sqrt{s_{\rm NN}} = 200$ GeV. Phys. Lett. B **616**, 8–16 (2005). https://doi.org/10.1016/j.physletb.2005.04.041
10. J. Adams, M.M. Aggarwal, Z. Ahammed et al., Open charm yields in d + Au collisions at $\sqrt{s_{\rm NN}} = 200$ GeV. Phys. Rev. Lett. **94**, 062301 (2005). https://doi.org/10.1103/PhysRevLett.94.062301
11. J. Adams, C. Adler, M.M. Aggarwal et al., Distributions of charged hadrons associated with high transverse momentum particles in pp and Au + Au collisions at $\sqrt{s_{\rm NN}} = 200$ GeV. Phys. Rev. Lett. **95**, 152301 (2005). https://doi.org/10.1103/PhysRevLett.95.152301
12. F. Geurts, M. Shao, B. Bonner et al., Performance of the prototype MRPC detector for STAR. Nucl. Instrum. Meth. A **533**, 60–64 (2004). https://doi.org/10.1016/j.nima.2004.07.001

13. J. Wu, B. Bonner, H.F. Chen et al., The performance of the TOFr tray in STAR. Nucl. Instrum. Meth. A **538**, 243–248 (2005). https://doi.org/10.1016/j.nima.2004.08.105
14. M. Shao, O. Barannikova, X. Dong et al., Extensive particle identification with TPC and TOF at the STAR experiment. Nucl. Instrum. Meth. A **558**, 419–429 (2006). https://doi.org/10.1016/j.nima.2005.11.251
15. T. Zou, X.L. Wang, M. Shao et al., Quality control of MRPC mass production for STAR TOF. Nucl. Instrum. Meth. A **605**, 282–292 (2009). https://doi.org/10.1016/j.nima.2009.03.239
16. Y. Wang, J.B. Wang, J.P. Cheng et al., Production and quality control of STAR-TOF MRPC. Nucl. Instrum. Meth. A **613**, 200–206 (2009). https://doi.org/10.1016/j.nima.2009.11.045
17. W.J. Llope, Multigap RPCs in the STAR experiment at RHIC. Nucl. Instrum. Meth. A **661**, S110–S113 (2012). https://doi.org/10.1016/j.nima.2010.07.086
18. H. Agakishiev et al., Observation of the antimatter helium-4 nucleus. Nature **473**, 353 (2011). [Erratum: Nature 475, 412 (2011)]. https://doi.org/10.1038/uure10079
19. M. Anderson, J. Berkovitz, W. Betts et al., The star time projection chamber: a unique tool for studying high multiplicity events at RHIC. Nucl. Instrum. Meth. A **499**, 659–678 (2003). https://doi.org/10.1016/S0168-9002(02)01964-2
20. Y.J. Sun, C. Li, M. Shao et al., New prototype multi-gap resistive plate chambers with long strips. Nucl. Instrum. Meth. A **593**, 307–313 (2008). https://doi.org/10.1016/j.nima.2008.05.042
21. L. Ruan, G. Lin, Z. Xu et al., Perspectives of a midrapidity dimuon program at RHIC: a novel and compact muon telescope detector. J. Phys. G: Nucl. Part. Phys. **36**, 095001 (2009). https://doi.org/10.1088/0954-3899/36/9/095001
22. C. Yang, X.J. Huang, C.M. Du et al., Calibration and performance of the STAR muon telescope detector using cosmic rays. Nucl. Instrum. Meth. A **762**, 1–6 (2014). https://doi.org/10.1016/j.nima.2014.05.075
23. P. Cao, H. Chen, M. Chen et al., Design and construction of the new BESIII endcap time-of-flight system with MRPC technology. Nucl. Instrum. Meth. A **953**, 163053 (2020). https://doi.org/10.1016/j.nima.2019.163053
24. J. Wang, Y. Wang, X.L. Zhu et al., Development of multi-gap resistive plate chambers with low-resistive silicate glass electrodes for operation at high particle fluxes and large transported charges. Nucl. Instrum. Meth. A **621**, 151–156 (2010). https://doi.org/10.1016/j.nima.2010.04.056
25. J. Wang, Y. Wang, D. Gonzalez-Diaz et al., Development of high-rate MRPCs for high resolution time-of-flight systems. Nucl. Instrum. Meth. A **713**, 40–51 (2013). https://doi.org/10.1016/j.nima.2013.02.036
26. B. Wang, D. Han, Y. Wang et al., The CEE-eTOF wall constructed with new sealed MRPC. JINST **15**, C08022 (2020)
27. E. Oberla, J.-F. Genat, H. Grabas et al., A 15 GSa/s, 1.5 GHz bandwidth waveform digitizing ASIC. Nucl. Instrum. Meth. A **735**, 452–461 (2013). https://doi.org/10.1016/j.nima.2013.09.042
28. J. Liu, L. Zhao, L.J. Yan et al., Design of a prototype readout electronics with a few picosecond time resolution for MRPC detectors. Nucl. Instrum. Meth. A **925**, 53–59 (2019). https://doi.org/10.1016/j.nima.2019.01.084
29. Y. Wang, Q. Zhang, H. Dong et al., Time of flight technology based on multi-gap resistive plate chamber. Acta Phys. Sin. **68**, 102901 (2019). https://doi.org/10.7498/aps.68.20182192
30. F. Wang, D. Han, Y. Wang, Improving the time resolution of the MRPC detector using deep-learning algorithms. JINST **15**, C09033 (2020). https://doi.org/10.1088/1748-0221/15/09/C09033
31. J. Xu, C.M. Ko, Chemical freeze-out in relativistic heavy-ion collisions. Phys. Lett. B **772**, 290–293 (2017). https://doi.org/10.1016/j.physletb.2017.06.061
32. L. Adamczyk, J.K. Adkins, G. Agakishiev et al., Bulk properties of the medium produced in relativistic heavy-ion collisions from the beam energy scan program. Phys. Rev. C **96**, 044904 (2017). https://doi.org/10.1103/PhysRevC.96.044904
33. J. Adam, L. Adamczyk, J.R. Adams et al., Strange hadron production in Au+Au collisions at $\sqrt{s_{NN}}$ =7.7, 11.5, 19.6, 27, and 39 GeV. Phys. Rev. C **102**, 034909 (2020). https://doi.org/10.1103/PhysRevC.102.034909
34. L. Adamczyk, J.K. Adkins, G. Agakishiev et al., Probing parton dynamics of QCD matter with Ω and ϕ production. Phys. Rev. C **93**, 021903 (2016). https://doi.org/10.1103/PhysRevC.93.021903
35. J. Adam, L. Adamczyk, J.R. Adams et al., Beam energy dependence of (anti-)deuteron production in Au + Au collisions at the BNL relativistic heavy ion collider. Phys. Rev. C **99**, 064905 (2019). https://doi.org/10.1103/PhysRevC.99.064905
36. E. Schnedermann, J. Sollfrank, U.W. Heinz, Thermal phenomenology of hadrons from 200 A/GeV S+S collisions. Phys. Rev. C **48**, 2462–2475 (1993). https://doi.org/10.1103/PhysRevC.48.2462
37. K. Fukushima, B. Mohanty, N. Xu, Little-bang and femto-nova in nucleus-nucleus collisions. AAPPS Bull. **31**, 1 (2021). https://doi.org/10.1007/s43673-021-00002-7
38. J. Adam et al., Nonmonotonic energy dependence of net-proton number fluctuations. Phys. Rev. Lett. **126**, 092301 (2021). https://doi.org/10.1103/PhysRevLett.126.092301
39. I.G. Bearden, D. Beavis, C. Besliu et al., Nuclear stopping in Au + Au collisions at $\sqrt{s_{\mathrm{NN}}}$ = 200 GeV. Phys. Rev. Lett. **93**, 102301 (2004). https://doi.org/10.1103/PhysRevLett.93.102301
40. B.I. Abelev, M.M. Aggarwal, Z. Ahammed et al., Systematic measurements of identified particle spectra in p p, d Au and Au+Au collisions from star. Phys. Rev. C **79**, 034909 (2009). https://doi.org/10.1103/PhysRevC.79.034909
41. K. Aamodt, N. Abel, U. Abeysekara et al., Midrapidity antiproton-to-proton ratio in pp collisions at $\sqrt{s}$ = 0.9 and 7 TeV measured by the ALICE experiment. Phys. Rev. Lett. **105**, 072002 (2010). https://doi.org/10.1103/PhysRevLett.105.072002
42. E. Abbas, B. Abelev, J. Adam et al., Mid-rapidity anti-baryon to baryon ratios in pp collisions at $\sqrt{s}$ = 0.9, 2.76 and 7 TeV measured by ALICE. Eur. Phys. J. C **73**, 2496 (2013). https://doi.org/10.1140/epjc/s10052-013-2496-5
43. D. Kharzeev, Can gluons trace baryon number? Phys. Lett. B **378**, 238–246 (1996). https://doi.org/10.1016/0370-2693(96)00435-2
44. N. Lewis, W. Lv, M.A. Ross et al., Search for baryon junctions in photonuclear processes and isobar collisions at RHIC. Eur. Phys. J. C **84**, 590 (2024). https://doi.org/10.1140/epjc/s10052-024-12834-2
45. I.C. Arsene, I.G. Bearden, D. Beavis et al., Nuclear stopping and rapidity loss in Au+Au collisions at $\sqrt{s_{\mathrm{NN}}}$ = 62.4 GeV. Phys. Lett. B **677**, 267–271 (2009). https://doi.org/10.1016/j.physletb.2009.05.049
46. C. Adler, Z. Ahammed, C. Allgower et al., Midrapidity anti-proton to proton ratio from Au + Au collisions at $\sqrt{s_{\mathrm{NN}}}$ = 130 GeV. Phys. Rev. Lett. **86**, 4778 (2001). [Erratum: Phys. Rev. Lett. 90, 119903 (2003)]. https://doi.org/10.1103/PhysRevLett.86.4778
47. C. Shen, B. Schenke, Longitudinal dynamics and particle production in relativistic nuclear collisions. Phys. Rev. C **105**, 064905 (2022). https://doi.org/10.1103/PhysRevC.105.064905
48. V. Topor Pop, M. Gyulassy, J. Barrette et al., Baryon junction loops in HIJING / B anti-B v2.0 and the baryon /meson

anomaly at RHIC. Phys. Rev. C **70**, 064906 (2004). https://doi.org/10.1103/PhysRevC.70.064906
49. G.H. Arakelyan, C. Merino, C. Pajares et al., Midrapidity production of secondaries in pp collisions at RHIC and LHC energies in the quark–gluon string model. Eur. Phys. J. C **54**, 577–581 (2008). https://doi.org/10.1140/epjc/s10052-008-0554-1
50. A. Shor, Phi meson production as a probe of the quark gluon plasma. Phys. Rev. Lett. **54**, 1122–1125 (1985). https://doi.org/10.1103/PhysRevLett.54.1122
51. P. Koch, B. Muller, J. Rafelski, Strangeness in relativistic heavy ion collisions. Phys. Rep. **142**, 167–262 (1986). https://doi.org/10.1016/0370-1573(86)90096-7
52. J. Rafelski, B. Muller, Strangeness production in the quark–gluon plasma. Phys. Rev. Lett. **48**, 1066 (1982). [Erratum: Phys.Rev.Lett. 56, 2334 (1986)]. https://doi.org/10.1103/PhysRevLett.48.1066
53. J. Cleymans, H. Oeschler, K. Redlich et al., Comparison of chemical freeze-out criteria in heavy-ion collisions. Phys. Rev. C **73**, 034905 (2006). https://doi.org/10.1103/PhysRevC.73.034905
54. A. Andronic, P. Braun-Munzinger, K. Redlich et al., Decoding the phase structure of QCD via particle production at high energy. Nature **561**, 321–330 (2018). https://doi.org/10.1038/s41586-018-0491-6
55. A. Andronic, P. Braun-Munzinger, J. Stachel, Hadron production in central nucleus-nucleus collisions at chemical freeze-out. Nucl. Phys. A **772**, 167–199 (2006). https://doi.org/10.1016/j.nuclphysa.2006.03.012
56. J.H. Chen, Y.G. Ma, G.L. Ma et al., Elliptic flow of phi mesons and strange quark collectivity. Phys. Rev. C **74**, 064902 (2006). https://doi.org/10.1103/PhysRevC.74.064902
57. J. Adams et al., Transverse momentum and collision energy dependence of high p(T) hadron suppression in Au+Au collisions at ultrarelativistic energies. Phys. Rev. Lett. **91**, 172302 (2003). https://doi.org/10.1103/PhysRevLett.91.172302
58. J. Adams, M.M. Aggarwal, Z. Ahammed et al., Scaling properties of hyperon production in Au+Au collisions at $\sqrt{s_{\mathrm{NN}}}$ = 200 GeV. Phys. Rev. Lett. **98**, 062301 (2007). https://doi.org/10.1103/PhysRevLett.98.062301
59. B.I. Abelev, M.M. Aggarwal, Z. Ahammed et al., Partonic flow and phi-meson production in Au + Au collisions at $\sqrt{s_{\mathrm{NN}}}$ = 200 GeV. Phys. Rev. Lett. **99**, 112301 (2007). https://doi.org/10.1103/PhysRevLett.99.112301
60. L. Adamczyk, J.R. Adams, J.K. Adkins et al., Beam energy dependence of jet-quenching effects in Au+Au collisions at $\sqrt{s_{\mathrm{NN}}}$ = 7.7, 11.5, 14.5, 19.6, 27, 39, and 62.4 GeV. Phys. Rev. Lett. **121**, 032301 (2018). https://doi.org/10.1103/PhysRevLett.121.032301
61. R.C. Hwa, C.B. Yang, Production of strange particles at intermediate pT in central Au+Au collisions at high energies. Phys. Rev. C **75**, 054904 (2007). https://doi.org/10.1103/PhysRevC.75.054904
62. R.J. Fries, B. Muller, C. Nonaka et al., Hadronization in heavy ion collisions: recombination and fragmentation of partons. Phys. Rev. Lett. **90**, 202303 (2003). https://doi.org/10.1103/PhysRevLett.90.202303
63. V. Greco, C.M. Ko, P. Levai, Parton coalescence and antiproton/pion anomaly at RHIC. Phys. Rev. Lett. **90**, 202302 (2003). https://doi.org/10.1103/PhysRevLett.90.202302
64. S. Ahmad et al., Lambda production by 11.6 A GeV/c Au beam on Au target. Phys. Lett. B **382**, 35–39 (1996). [Erratum: Phys. Lett.B 386, 496–496 (1996)]. https://doi.org/10.1016/0370-2693(96)00642-9
65. S. Ahmad, B.E. Bonner, S.V. Efremov et al., Nuclear matter expansion parameters from the measurement of differential multiplicities for lambda production in central Au+Au collisions at AGS. Nucl. Phys. A **636**, 507–524 (1998). https://doi.org/10.1016/S0375-9474(98)00218-8
66. B.B. Back, R.R. Betts, J. Chang et al., Anti-lambda production in Au+Au collisions at 11.7 A GeV/c. Phys. Rev. Lett. **87**, 242301 (2001). https://doi.org/10.1103/PhysRevLett.87.242301
67. S. Albergo, R. Bellwied, M. Bennett et al., Lambda spectra in 11.6 A GeV/c Au Au collisions. Phys. Rev. Lett. **88**, 062301 (2002). https://doi.org/10.1103/PhysRevLett.88.062301
68. J. Adams, C. Adler, M.M. Aggarwal et al., Multistrange baryon production in Au-Au collisions at $\sqrt{s_{\mathrm{NN}}}$ = 130 GeV. Phys. Rev. Lett. **92**, 182301 (2004). https://doi.org/10.1103/PhysRevLett.92.182301
69. C. Adler, Z. Ahammed, C. Allgower et al., Midrapidity lambda and anti-lambda production in Au + Au collisions at $\sqrt{s_{\mathrm{NN}}}$ = 130 GeV. Phys. Rev. Lett. **89**, 092301 (2002). https://doi.org/10.1103/PhysRevLett.89.092301
70. G. Agakishiev, M.M. Aggarwal, Z. Ahammed et al., Strangeness enhancement in Cu+Cu and Au+Au collisions at $\sqrt{s_{\mathrm{NN}}}$ = 200 GeV. Phys. Rev. Lett. **108**, 072301 (2012). https://doi.org/10.1103/PhysRevLett.108.072301
71. F. Antinori, P. Bacon, A Badalà et al., Enhancement of hyperon production at central rapidity in 158 A GeV/c Pb-Pb collisions. J. Phys. G **32**, 427–442 (2006). https://doi.org/10.1088/0954-3899/32/4/003
72. F. Antinori, P.A Bacon, A Badalà et al., Energy dependence of hyperon production in nucleus nucleus collisions at SPS. Phys. Lett. B **595**, 68–74 (2004). https://doi.org/10.1016/j.physletb.2004.05.025
73. C. Alt, T. Anticic, B. Baatar et al., Energy dependence of Λ and Ξ production in central Pb+Pb collisions at 20A, 30A, 40A, 80A, and 158A GeV measured at the CERN Super Proton Synchrotron. Phys. Rev. C **78**, 034918 (2008). https://doi.org/10.1103/PhysRevC.78.034918
74. S.V. Afanasiev, T. Anticic, D. Barna et al., Energy dependence of pion and kaon production in central Pb + Pb collisions. Phys. Rev. C **66**, 054902 (2002). https://doi.org/10.1103/PhysRevC.66.054902
75. C. Alt, T. Anticic, B. Baatar et al., Pion and kaon production in central Pb + Pb collisions at 20 A and 30 A GeV: evidence for the onset of deconfinement. Phys. Rev. C **77**, 024903 (2008). https://doi.org/10.1103/PhysRevC.77.024903
76. S.A. Bass, M. Belkacem, M. Bleicher et al., Microscopic models for ultrarelativistic heavy ion collisions. Prog. Part. Nucl. Phys. **41**, 255–369 (1998). https://doi.org/10.1016/S0146-6410(98)00058-1
77. M. Bleicher, E Zabrodin, C. Spieles et al., Relativistic hadron hadron collisions in the ultrarelativistic quantum molecular dynamics model. J. Phys. G **25**, 1859–1896 (1999). https://doi.org/10.1088/0954-3899/25/9/308
78. M.S. Abdallah et al., Probing strangeness canonical ensemble with K^-, $\phi(1020)$ and Ξ^- production in Au+Au collisions at $\sqrt{s_{\mathrm{NN}}}$ = 3 GeV. Phys. Lett. B **831**, 137152 (2022). https://doi.org/10.1016/j.physletb.2022.137152
79. K. Redlich, A. Tounsi, Strangeness enhancement and energy dependence in heavy ion collisions. Eur. Phys. J. C **24**, 589–594 (2002). https://doi.org/10.1007/s10052-002-0983-1
80. C. Alt, T. Anticic, B. Baatar et al., Energy dependence of phi meson production in central Pb+Pb collisions at $\sqrt{s_{\mathrm{NN}}}$ = 6 to 17 GeV. Phys. Rev. C **78**, 044907 (2008). https://doi.org/10.1103/PhysRevC.78.044907
81. J. Adamczewski-Musch et al., Deep sub-threshold ϕ production in Au+Au collisions. Phys. Lett. B **778**, 403–407 (2018). https://doi.org/10.1016/j.physletb.2018.01.048

82. J. Steinheimer, M. Bleicher, Sub-threshold ϕ and Ξ^- production by high mass resonances with UrQMD. J. Phys. G **43**, 015104 (2016). https://doi.org/10.1088/0954-3899/43/1/015104
83. T. Shao, J. Chen, C.M. Ko et al., Probing QCD critical fluctuations from the yield ratio of strange hadrons in relativistic heavy-ion collisions. Phys. Lett. B **801**, 135177 (2020). https://doi.org/10.1016/j.physletb.2019.135177
84. J. Aichelin, C.M. Ko, Subthreshold kaon production as a probe of the nuclear equation of state. Phys. Rev. Lett. **55**, 2661–2663 (1985). https://doi.org/10.1103/PhysRevLett.55.2661
85. Y.G. Ma, The colective flow from the degree of fredom of nucleons to quarks. J Fudan Univ (Nat Sci) **62**, 273 (2023). https://doi.org/10.15943/j.cnki.fdxb-jns.20230525.001
86. Y.G. Ma, S. Zhang, α-clustering effects in relativistic heavy-ion collisions. Sci Sin-Phys Mech Astron **50**, 013002 (2024). https://doi.org/10.1360/SSPMA-2024-0013. (**in Chinese**)
87. L. Adamczyk et al., Observation of an energy-dependent difference in elliptic flow between particles and antiparticles in relativistic heavy ion collisions. Phys. Rev. Lett. **110**, 142301 (2013). https://doi.org/10.1103/PhysRevLett.110.142301
88. L. Adamczyk et al., Centrality dependence of identified particle elliptic flow in relativistic heavy ion collisions at $\sqrt{s_{\rm NN}}$=7.7-62.4 GeV. Phys. Rev. C **93**, 014907 (2016). https://doi.org/10.1103/PhysRevC.93.014907
89. B.I. Abelev et al., Centrality dependence of charged hadron and strange hadron elliptic flow from $\sqrt{s_{\rm NN}}$ = 200 GeV Au + Au collisions. Phys. Rev. C **77**, 054901 (2008). https://doi.org/10.1103/PhysRevC.77.054901
90. X. Dong, S. Esumi, P. Sorensen et al., Resonance decay effects on anisotropy parameters. Phys. Lett. B **597**, 328–332 (2004). https://doi.org/10.1016/j.physletb.2004.06.110
91. L. Adamczyk et al., Elliptic flow of identified hadrons in Au+Au collisions at $\sqrt{s_{\rm NN}}$ = 7.7–62.4 GeV. Phys. Rev. C **88**, 014902 (2013). https://doi.org/10.1103/PhysRevC.88.014902
92. L. Adamczyk et al., Centrality and transverse momentum dependence of elliptic flow of multistrange hadrons and ϕ meson in Au+Au collisions at $\sqrt{s_{\rm NN}}$ = 200 GeV. Phys. Rev. Lett. **116**, 062301 (2016). https://doi.org/10.1103/PhysRevLett.116.062301
93. L. Adamczyk et al., Beam-energy dependence of directed flow of λ, $\bar{\Lambda}$, K$^{\pm}$, k_s^0 and ϕ in Au+Au collisions. Phys. Rev. Lett. **120**, 062301 (2018). https://doi.org/10.1103/PhysRevLett.120.062301
94. J.C. Dunlop, M.A. Lisa, P. Sorensen, Constituent quark scaling violation due to baryon number transport. Phys. Rev. C **84**, 044914 (2011). https://doi.org/10.1103/PhysRevC.84.044914
95. D. Molnar, S.A. Voloshin, Elliptic flow at large transverse momenta from quark coalescence. Phys. Rev. Lett. **91**, 092301 (2003). https://doi.org/10.1103/PhysRevLett.91.092301
96. L. Adamczyk et al., Measurement of D^0 azimuthal anisotropy at midrapidity in Au+Au collisions at $\sqrt{s_{NN}}$=200 GeV. Phys. Rev. Lett. **118**, 212301 (2017). https://doi.org/10.1103/PhysRevLett.118.212301
97. T.Z. Yan, Y.G. Ma, X.Z. Cai et al., Scaling of anisotropic flow and momentum-space densities for light particles in intermediate energy heavy ion collisions. Phys. Lett. B **638**, 50 (2006). https://doi.org/10.1016/j.physletb.2006.05.018
98. L. Adamczyk et al., Measurement of elliptic flow of light nuclei at $\sqrt{s_{\rm NN}}$ = 200, 62.4, 39, 27, 19.6, 11.5, and 7.7 GeV at the BNL Relativistic Heavy Ion Collider. Phys. Rev. C **94**, 034908 (2016). https://doi.org/10.1103/PhysRevC.94.034908
99. K. Aamodt et al., Higher harmonic anisotropic flow measurements of charged particles in Pb-Pb collisions at $\sqrt{s_{\rm NN}}$ = 2.76 TeV. Phys. Rev. Lett. **107**, 032301 (2011). https://doi.org/10.1103/PhysRevLett.107.032301
100. L.X. Han, G.L. Ma, Y.G. Ma et al., Initial fluctuation effect on harmonic flows in high-energy heavy-ion collisions. Phys. Rev. C **84**, 064907 (2011). https://doi.org/10.1103/PhysRevC.84.064907
101. M. Abdallah et al., Centrality and transverse momentum dependence of higher-order flow harmonics of identified hadrons in Au+Au collisions at $\sqrt{s_{\rm NN}}$ = 200 GeV. Phys. Rev. C **105**, 064911 (2022). https://doi.org/10.1103/PhysRevC.105.064911
102. L. Adamczyk et al., Beam energy dependence of the third harmonic of azimuthal correlations in Au+Au collisions at RHIC. Phys. Rev. Lett. **116**, 112302 (2016). https://doi.org/10.1103/PhysRevLett.116.112302
103. J. Tian, J.H. Chen, Y.G. Ma et al., Breaking of the number-of-constituent-quark scaling for identified-particle elliptic flow as a signal of phase change in low-energy data taken at the BNL relativistic heavy ion collider (RHIC). Phys. Rev. C **79**, 067901 (2009). https://doi.org/10.1103/PhysRevC.79.067901
104. Y. Nara, N. Otuka, A. Ohnishi et al., Study of relativistic nuclear collisions at AGS energies from p + Be to Au + Au with hadronic cascade model. Phys. Rev. C **61**, 024901 (2000). https://doi.org/10.1103/PhysRevC.61.024901
105. L. Adamczyk et al., Beam-energy dependence of the directed flow of protons, antiprotons, and pions in Au+Au collisions. Phys. Rev. Lett. **112**, 162301 (2014). https://doi.org/10.1103/PhysRevLett.112.162301
106. R.J.M. Snellings, H. Sorge, S.A. Voloshin et al., Novel rapidity dependence of directed flow in high-energy heavy ion collisions. Phys. Rev. Lett. **84**, 2803–2805 (2000). https://doi.org/10.1103/PhysRevLett.84.2803
107. L. Adamczyk et al., Inclusive charged hadron elliptic flow in Au + Au collisions at $\sqrt{s_{\rm NN}}$ = 7.7 − −39 GeV. Phys. Rev. C **86**, 054908 (2012). https://doi.org/10.1103/PhysRevC.86.054908
108. J.E. Bernhard, J.S. Moreland, S.A. Bass, Bayesian estimation of the specific shear and bulk viscosity of quark–gluon plasma. Nat. Phys. **15**, 1113–1117 (2019). https://doi.org/10.1038/s41567-019-0611-8
109. Y. Xu, J.E. Bernhard, S.A. Bass et al., Data-driven analysis for the temperature and momentum dependence of the heavy-quark diffusion coefficient in relativistic heavy-ion collisions. Phys. Rev. C **97**, 014907 (2018). https://doi.org/10.1103/PhysRevC.97.014907
110. H.Z. Huang, F. Liu, X. Luo et al., Collective excitation in high-energy nuclear collisions-in memory of professor Lianshou Liu. Symmetry **15**, 499 (2023). https://doi.org/10.3390/sym15020499
111. L.P. Csernai, J.I. Kapusta, L.D. McLerran, On the strongly-interacting low-viscosity matter created in relativistic nuclear collisions. Phys. Rev. Lett. **97**, 152303 (2006). https://doi.org/10.1103/PhysRevLett.97.152303
112. X.G. Deng, D.Q. Fang, Y.G. Ma, Shear viscosity of nucleonic matter. Prog. Part. Nucl. Phys. **136**, 104095 (2024). https://doi.org/10.1016/j.ppnp.2023.104095
113. T.D. Lee, G.C. Wick, Vacuum stability and vacuum excitation in a spin 0 field theory. Phys. Rev. D **9**, 2291–2316 (1974). https://doi.org/10.1103/PhysRevD.9.2291
114. D. Kharzeev, R.D. Pisarski, M.H.G. Tytgat, Possibility of spontaneous parity violation in hot QCD. Phys. Rev. Lett. **81**, 512–515 (1998). https://doi.org/10.1103/PhysRevLett.81.512
115. D. Kharzeev, R.D. Pisarski, Pionic measures of parity and CP violation in high-energy nuclear collisions. Phys. Rev. D **61**, 111901 (2000). https://doi.org/10.1103/PhysRevD.61.111901
116. K. Fukushima, D.E. Kharzeev, H.J. Warringa, The chiral magnetic effect. Phys. Rev. D **78**, 074033 (2008). https://doi.org/10.1103/PhysRevD.78.074033
117. B. Muller, A. Schafer, Charge fluctuations from the chiral magnetic effect in nuclear collisions. Phys. Rev. C **82**, 057902 (2010). https://doi.org/10.1103/PhysRevC.82.057902
118. D.E. Kharzeev, J. Liao, S.A. Voloshin et al., Chiral magnetic and vortical effects in high-energy nuclear collisions—a status

report. Prog. Part. Nucl. Phys. **88**, 1–28 (2016). https://doi.org/10.1016/j.ppnp.2016.01.001
119. J. Zhao, F. Wang, Experimental searches for the chiral magnetic effect in heavy-ion collisions. Prog. Part. Nucl. Phys. **107**, 200–236 (2019). https://doi.org/10.1016/j.ppnp.2019.05.001
120. W. Li, G. Wang, Chiral magnetic effects in nuclear collisions. Ann. Rev. Nucl. Part. Sci. **70**, 293–321 (2020). https://doi.org/10.1146/annurev-nucl-030220-065203
121. B.I. Abelev et al., Azimuthal charged-particle correlations and possible local strong parity violation. Phys. Rev. Lett. **103**, 251601 (2009). https://doi.org/10.1103/PhysRevLett.103.251601
122. L. Adamczyk et al., Beam-energy dependence of charge separation along the magnetic field in Au+Au collisions at RHIC. Phys. Rev. Lett. **113**, 052302 (2014). https://doi.org/10.1103/PhysRevLett.113.052302
123. B. Abelev et al., Charge separation relative to the reaction plane in Pb-Pb collisions at $\sqrt{s_{\mathrm{NN}}} = 2.76$ TeV. Phys. Rev. Lett. **110**, 012301 (2013). https://doi.org/10.1103/PhysRevLett.110.012301
124. S.A. Voloshin, Parity violation in hot QCD: How to detect it. Phys. Rev. C **70**, 057901 (2004). https://doi.org/10.1103/PhysRevC.70.057901
125. F. Wang, Effects of cluster particle correlations on local parity violation observables. Phys. Rev. C **81**, 064902 (2010). https://doi.org/10.1103/PhysRevC.81.064902
126. A. Bzdak, V. Koch, J. Liao, Remarks on possible local parity violation in heavy ion collisions. Phys. Rev. C **81**, 031901 (2010). https://doi.org/10.1103/PhysRevC.81.031901
127. S. Schlichting, S. Pratt, Charge conservation at energies available at the BNL Relativistic Heavy Ion Collider and contributions to local parity violation observables. Phys. Rev. C **83**, 014913 (2011). https://doi.org/10.1103/PhysRevC.83.014913
128. X.N. Wang, M. Gyulassy, Energy and centrality dependence of rapidity densities at RHIC. Phys. Rev. Lett. **86**, 3496–3499 (2001). https://doi.org/10.1103/PhysRevLett.86.3496
129. V. Khachatryan et al., Observation of charge-dependent azimuthal correlations in p-Pb collisions and its implication for the search for the chiral magnetic effect. Phys. Rev. Lett. **118**, 122301 (2017). https://doi.org/10.1103/PhysRevLett.118.122301
130. J. Adam et al., Charge-dependent pair correlations relative to a third particle in p + Au and d + Au collisions at RHIC. Phys. Lett. B **798**, 134975 (2019). https://doi.org/10.1016/j.physletb.2019.134975
131. L. Adamczyk et al., Long-range pseudorapidity dihadron correlations in d+Au collisions at $\sqrt{s_{\mathrm{NN}}}$=200 GeV. Phys. Lett. **747**, 265–271 (2015). https://doi.org/10.1016/j.physletb.2015.05.075
132. M.I. Abdulhamid et al., Measurements of the elliptic and triangular azimuthal anisotropies in central ^{3}He + Au, d+Au and p+Au collisions at $\sqrt{s_{\mathrm{NN}}}$ =200 GeV. Phys. Rev. Lett. **130**, 242301 (2023). https://doi.org/10.1103/PhysRevLett.130.242301
133. V. Khachatryan et al., Observation of long-range near-side angular correlations in proton-proton collisions at the LHC. JHEP **1009**, 091 (2010). https://doi.org/10.1007/JHEP09(2010)091
134. S. Acharya et al., Constraining the magnitude of the chiral magnetic effect with event shape engineering in Pb-Pb collisions at $\sqrt{s_{\mathrm{NN}}} = 2.76$ TeV. Phys. Lett. B **777**, 151–162 (2018). https://doi.org/10.1016/j.physletb.2017.12.021
135. M. Abdallah, B.E. Aboona, J. Adam et al., Search for the chiral magnetic effect with isobar collisions at $\sqrt{s_{\mathrm{NN}}}$=200 GeV by the STAR Collaboration at the BNL relativistic heavy ion collider. Phys. Rev. C **105**, 014901 (2022). https://doi.org/10.1103/PhysRevC.105.014901
136. M. Abdallah, B.E. Aboona, J. Adam et al., Upper limit on the chiral magnetic effect in isobar collisions at the relativistic heavy-ion collider. Phys. Rev. Res. **6** L032005 (2024). arXiv:2308.16846
137. M. Abdallah, B.E. Aboona, J. Adam et al., Estimate of background baseline and upper limit on the chiral magnetic effect in isobar collisions at $\sqrt{s_{\mathrm{NN}}} = 200$ GeV at the relativistic heavy-ion collider. Phys. Rev. C **110**, 014905 (2024). arXiv:2310.13096
138. S.A. Voloshin, Testing the chiral magnetic effect with central U+U collisions. Phys. Rev. Lett. **105**, 172301 (2010). https://doi.org/10.1103/PhysRevLett.105.172301
139. H.J. Xu, X. Wang, H. Li et al., Importance of isobar density distributions on the chiral magnetic effect search. Phys. Rev. Lett. **121**, 022301 (2018). https://doi.org/10.1103/PhysRevLett.121.022301
140. H. Li, Hj. Xu, J. Zhao et al., Multiphase transport model predictions of isobaric collisions with nuclear structure from density functional theory. Phys. Rev. **98**, 054907 (2018). https://doi.org/10.1103/PhysRevC.98.054907
141. H. Li, Hj. Xu, Y. Zhou et al., Probing the neutron skin with ultrarelativistic isobaric collisions. Phys. Rev. Lett. **125**, 222301 (2020). https://doi.org/10.1103/PhysRevLett.125.222301
142. D.E. Kharzeev, J. Liao, S. Shi, Implications of the isobar-run results for the chiral magnetic effect in heavy-ion collisions. Phys. Rev. C **106**, L051903 (2022). https://doi.org/10.1103/PhysRevC.106.L051903
143. Y. Feng, J. Zhao, H. Li et al., Two- and three-particle nonflow contributions to the chiral magnetic effect measurement by spectator and participant planes in relativistic heavy ion collisions. Phys. Rev. C **105**, 024913 (2022). https://doi.org/10.1103/PhysRevC.105.024913
144. J. Schukraft, A. Timmins, S.A. Voloshin, Ultra-relativistic nuclear collisions: event shape engineering. Phys. Lett. B **719**, 394–398 (2013). https://doi.org/10.1016/j.physletb.2013.01.045
145. A.M. Sirunyan et al., Constraints on the chiral magnetic effect using charge-dependent azimuthal correlations in p-Pb and Pb-Pb collisions at the CERN Large Hadron Collider. Phys. Rev. C **97**, 044912 (2018). https://doi.org/10.1103/PhysRevC.97.044912
146. H. Petersen, B. Muller, Possibility of event shape selection in relativistic heavy ion collisions. Phys. Rev. C **88**, 044918 (2013). https://doi.org/10.1103/PhysRevC.88.044918
147. Z. Xu, B. Chan, G. Wang et al., Event shape selection method in search of the chiral magnetic effect in heavy-ion collisions. Phys. Lett. B **848**, 138367 (2024). https://doi.org/10.1016/j.physletb.2023.138367
148. Z.W. Lin, C.M. Ko, B.A. Li et al., A multi-phase transport model for relativistic heavy ion collisions. Phys. Rev. C **72**, 064901 (2005). https://doi.org/10.1103/PhysRevC.72.064901
149. S. Shi, Y. Jiang, E. Lilleskov et al., Anomalous chiral transport in heavy ion collisions from anomalous-viscous fluid dynamics. Ann. Phys. **394**, 50–72 (2018). https://doi.org/10.1016/j.aop.2018.04.026
150. M.I. Abdulhamid et al., Observation of the electromagnetic field effect via charge-dependent directed flow in heavy-ion collisions at the Relativistic Heavy Ion Collider. Phys. Rev. X **14**, 011028 (2024). https://doi.org/10.1103/PhysRevX.14.011028
151. Z. Xu, Search for the chiral magnetic and vortical effects using event shape approaches in Au+Au collisions at STAR. (2024). arXiv:2401.00317
152. H.J. Xu, J. Zhao, X. Wang et al., Varying the chiral magnetic effect relative to flow in a single nucleus-nucleus collision. Chin. Phys. C **42**, 084103 (2018). https://doi.org/10.1088/1674-1137/42/8/084103
153. S.A. Voloshin, Estimate of the signal from the chiral magnetic effect in heavy-ion collisions from measurements relative to the participant and spectator flow planes. Phys. Rev. C **98**, 054911 (2018). https://doi.org/10.1103/PhysRevC.98.054911

154. M.S. Abdallah et al., Search for the chiral magnetic effect via charge-dependent azimuthal correlations relative to spectator and participant planes in Au+Au collisions at $\sqrt{s_{\rm NN}} = 200$ GeV. Phys. Rev. Lett. **128**, 092301 (2022). https://doi.org/10.1103/PhysRevLett.128.092301
155. Y. Aoki, G. Endrodi, Z. Fodor et al., The order of the quantum chromodynamics transition predicted by the standard model of particle physics. Nature **443**, 675–678 (2006). https://doi.org/10.1038/nature05120
156. C.M. Ko, Searching for QCD critical point with light nuclei. Nucl. Sci. Technol. **34**, 80 (2023). https://doi.org/10.1007/s41365-023-01231-1
157. X. Luo, N. Xu, Search for the QCD critical point with fluctuations of conserved quantities in relativistic heavy-ion collisions at RHIC: an overview. Nucl. Sci. Technol. **28**, 112 (2017). https://doi.org/10.1007/s41365-017-0257-0
158. M. Abdallah, J. Adam, L. Adamczyk et al., Cumulants and correlation functions of net-proton, proton, and antiproton multiplicity distributions in Au+Au collisions at energies available at the BNL Relativistic Heavy Ion Collider. Phys. Rev. C **104**, 024902 (2021). https://doi.org/10.1103/PhysRevC.104.024902
159. M. Abdallah, B.E. Aboona, J. Adam et al., Higher-order cumulants and correlation functions of proton multiplicity distributions in $\sqrt{s_{\rm NN}} = 3$ GeV Au+Au collisions at the RHIC STAR experiment. Phys. Rev. C **107**, 024908 (2023). https://doi.org/10.1103/PhysRevC.107.024908
160. M.S. Abdallah, B.E. Aboona, J. Adam et al., Measurements of proton high order cumulants in $\sqrt{s_{\rm NN}} = 3$ GeV Au+Au collisions and implications for the QCD critical point. Phys. Rev. Lett. **128**, 202303 (2022). https://doi.org/10.1103/PhysRevLett.128.202303
161. M. Abdulhamid et al., Energy dependence of intermittency for charged hadrons in Au+Au collisions at RHIC. Phys. Lett. B **845**, 138165 (2023). https://doi.org/10.1016/j.physletb.2023.138165
162. R.C. Hwa, M.T. Nazirov, Intermittency in second order phase transition. Phys. Rev. Lett. **69**, 741–744 (1992). https://doi.org/10.1103/PhysRevLett.69.741
163. N.G. Antoniou, F.K. Diakonos, A.S. Kapoyannis et al., Critical opalescence in baryonic QCD matter. Phys. Rev. Lett. **97**, 032002 (2006). https://doi.org/10.1103/PhysRevLett.97.032002
164. Y.G. Ma, Application of information theory in nuclear liquid gas phase transition. Phys. Rev. Lett. **83**, 3617–3620 (1999). https://doi.org/10.1103/PhysRevLett.83.3617
165. X.G. Deng, Y.G. Ma, Information entropy for central ^{197}Au+^{197}Au collisions in the UrQMD model. (2024). Preprint at arXiv:2404.03424
166. M. Abdulhamid et al., Beam energy dependence of triton production and yield ratio ($\rm N_t \times N_p/N_d^2$) in Au+Au collisions at RHIC. Phys. Rev. Lett. **130**, 202301 (2023). https://doi.org/10.1103/PhysRevLett.130.202301
167. E.V. Shuryak, Quantum chromodynamics and the theory of superdense matter. Phys. Rep. **61**, 71–158 (1980). https://doi.org/10.1016/0370-1573(80)90105-2
168. Z.T. Liang, X.N. Wang, Globally polarized quark-gluon plasma in non-central A+A collisions. Phys. Rev. Lett. **94**, 102301 (2005). [Erratum: Phys. Rev. Lett.96,039901(2006)]. https://doi.org/10.1103/PhysRevLett.94.102301, 10.1103/PhysRevLett.96.039901
169. Z.T. Liang, X.N. Wang, Spin alignment of vector mesons in non-central A+A collisions. Phys. Lett. B **629**, 20–26 (2005). https://doi.org/10.1016/j.physletb.2005.09.060
170. J.H. Gao, S.W. Chen, W.T. Deng et al., Global quark polarization in non-central A+A collisions. Phys. Rev. C **77**, 044902 (2008). https://doi.org/10.1103/PhysRevC.77.044902
171. B. Betz, M. Gyulassy, G. Torrieri, Polarization probes of vorticity in heavy ion collisions. Phys. Rev. C **76**, 044901 (2007). https://doi.org/10.1103/PhysRevC.76.044901
172. F. Becattini, F. Piccinini, J. Rizzo, Angular momentum conservation in heavy ion collisions at very high energy. Phys. Rev. C **77**, 024906 (2008). https://doi.org/10.1103/PhysRevC.77.024906
173. S.J. Barnett, Magnetization by rotation. Phys. Rev. **6**, 239 (1915). https://doi.org/10.1103/PhysRev.6.239
174. A. Einstein, W.J. de Haas Verh. Phys. Gesell. **17**, 152 (1915)
175. L. Adamczyk et al., Global Λ hyperon polarization in nuclear collisions: evidence for the most vortical fluid. Nature **548**, 62–65 (2017). https://doi.org/10.1038/nature23004
176. A.M. Poskanzer, S.A. Voloshin, Methods for analyzing anisotropic flow in relativistic nuclear collisions. Phys. Rev. C **58**, 1671–1678 (1998). https://doi.org/10.1103/PhysRevC.58.1671
177. J. Adam et al., Global polarization of Λ hyperons in Au+Au collisions at $\sqrt{s_{\rm NN}} = 200$ GeV. Phys. Rev. C **98**, 014910 (2018). https://doi.org/10.1103/PhysRevC.98.014910
178. X. Sun, C.S. Zhou, J.H. Chen et al., Measurements of global polarization of QCD matter in heavy-ion collisions. Acta Phys. Sin. **72**, 072401 (2023). https://doi.org/10.7498/aps.72.20222452
179. B.I. Abelev et al., Global polarization measurement in Au+Au collisions. Phys. Rev. C **76**, 024915 (2007). [Erratum: Phys. Rev.C 95, 039906 (2017)]. https://doi.org/10.1103/PhysRevC.76.024915
180. S. Acharya et al., Global polarization of $\Lambda\bar{\Lambda}$ hyperons in Pb-Pb collisions at $\sqrt{s_{\rm NN}} = 2.76$ and 5.02 TeV. Phys. Rev. C **101**, 044611 (2020). [Erratum: Phys.Rev.C 105, 029902 (2022)]. https://doi.org/10.1103/PhysRevC.101.044611
181. M.S. Abdallah et al., Global Λ-hyperon polarization in Au+Au collisions at $\sqrt{s_{\rm NN}}$=3 GeV. Phys. Rev. C **104**, L061901 (2021). https://doi.org/10.1103/PhysRevC.104.L061901
182. R. Abou Yassine et al., Measurement of global polarization of Λ hyperons in few-GeV heavy-ion collisions. Phys. Lett. B **835**, 137506 (2022). https://doi.org/10.1016/j.physletb.2022.137506
183. M.I. Abdulhamid et al., Global polarization of Λ and Λ^- hyperons in Au+Au collisions at $\sqrt{s_{\rm NN}}$=19.6 and 27 GeV. Phys. Rev. C **108**, 014910 (2023). https://doi.org/10.1103/PhysRevC.108.014910
184. I. Karpenko, F. Becattini, Study of Λ polarization in relativistic nuclear collisions at $\sqrt{s_{\rm NN}} = 7.7 - 200$ GeV. Eur. Phys. J. C **77**, 213 (2017). https://doi.org/10.1140/epjc/s10052-017-4765-1
185. Y. Sun, C.M. Ko, Λ hyperon polarization in relativistic heavy ion collisions from a chiral kinetic approach. Phys. Rev. C **96**, 024906 (2017). https://doi.org/10.1103/PhysRevC.96.024906
186. H. Li, L.G. Pang, Q. Wang et al., Global Λ polarization in heavy-ion collisions from a transport model. Phys. Rev. C **96**, 054908 (2017). https://doi.org/10.1103/PhysRevC.96.054908
187. Y.B. Ivanov, Global Λ polarization in moderately relativistic nuclear collisions. Phys. Rev. C **103**, L031903 (2021). https://doi.org/10.1103/PhysRevC.103.L031903
188. Y. Guo, J. Liao, E. Wang et al., Hyperon polarization from the vortical fluid in low-energy nuclear collisions. Phys. Rev. C **104**, L041902 (2021). https://doi.org/10.1103/PhysRevC.104.L041902
189. Z.T. Liang, J. Song, I. Upsal et al., Rapidity dependence of global polarization in heavy ion collisions. Chin. Phys. C **45**, 014102 (2021). https://doi.org/10.1088/1674-1137/abc065
190. S. Alzhrani, S. Ryu, C. Shen, Λ spin polarization in event-by-event relativistic heavy-ion collisions. Phys. Rev. C **106**, 014905 (2022). https://doi.org/10.1103/PhysRevC.106.014905
191. M. Abdulhamid et al., Hyperon polarization along the beam direction relative to the second and third harmonic event planes in isobar collisions at $\sqrt{s_{\rm NN}}$ =200 GeV. Phys. Rev. Lett. **131**, 202301 (2023). https://doi.org/10.1103/PhysRevLett.131.202301

192. K. Schilling, P. Seyboth, G.E. Wolf, On the analysis of vector meson production by polarized photons. Nucl. Phys. B **15**, 397–412 (1970). [Erratum: Nucl. Phys.B18,332(1970)]. https://doi.org/10.1016/0550-3213(70)90295-6, 10.1016/0550-3213(70)90070-2
193. B.I. Abelev et al., Spin alignment measurements of the K^{*0}(892) and ϕ (1020) vector mesons in heavy ion collisions at $\sqrt{s_{NN}}$ = 200 GeV. Phys. Rev. C **77**, 061902 (2008). https://doi.org/10.1103/PhysRevC.77.061902
194. S. Acharya et al., Evidence of spin-orbital angular momentum interactions in relativistic heavy-ion collisions. Phys. Rev. Lett. **125**, 012301 (2020). https://doi.org/10.1103/PhysRevLett.125.012301
195. X.L. Sheng, L. Oliva, Q. Wang, What can we learn from the global spin alignment of ϕ mesons in heavy-ion collisions? Phys. Rev. D **101**, 096005 (2020). [Erratum: Phys.Rev.D 105, 099903 (2022)]. https://doi.org/10.1103/PhysRevD.101.096005
196. X.L. Sheng, L. Oliva, Z.T. Liang et al., Spin alignment of vector mesons in heavy-ion collisions. Phys. Rev. Lett. **131**, 042304 (2023). https://doi.org/10.1103/PhysRevLett.131.042304
197. M.S. Abdallah et al., Pattern of global spin alignment of ϕ and K^{*0} mesons in heavy-ion collisions. Nature **614**, 244–248 (2023). https://doi.org/10.1038/s41586-022-05557-5
198. X.L. Xia, H. Li, X.G. Huang et al., Local spin alignment of vector mesons in relativistic heavy-ion collisions. Phys. Lett. B **817**, 136325 (2021). https://doi.org/10.1016/j.physletb.2021.136325
199. J.H. Gao, Helicity polarization in relativistic heavy ion collisions. Phys. Rev. D **104**, 076016 (2021). https://doi.org/10.1103/PhysRevD.104.076016
200. B. Müller, D.L. Yang, Anomalous spin polarization from turbulent color fields. Phys. Rev. D **105**, L011901 (2022). [Erratum: Phys.Rev.D 106, 039904 (2022)]. https://doi.org/10.1103/PhysRevD.105.L011901
201. J.P. Lv, Z.H. Yu, Z.T. Liang et al., Global quark spin correlations in relativistic heavy ion collisions. arXiv:2402.13721
202. X.N. Wang, Vector meson spin alignment by the strong force field. Nucl. Sci. Technol. **34**, 15 (2023). https://doi.org/10.1007/s41365-023-01166-7
203. J. Chen, Z.T. Liang, Y.G. Ma et al., Global spin alignment of vector mesons and strong force fields in heavy-ion collisions. Sci. Bull. **68**, 874–877 (2023). https://doi.org/10.1016/j.scib.2023.04.001
204. S.T. Butler, C.A. Pearson, Deuterons from high-energy proton bombardment of matter. Phys. Rev. Lett. **7**, 69–71 (1961). https://doi.org/10.1103/PhysRevLett.7.69
205. A. Andronic, P. Braun-Munzinger, J. Stachel et al., Production of light nuclei, hypernuclei and their antiparticles in relativistic nuclear collisions. Phys. Lett. B **697**, 203–207 (2011). https://doi.org/10.1016/j.physletb.2011.01.053
206. P. Braun-Munzinger, B. Dönigus, Loosely-bound objects produced in nuclear collisions at the LHC. Nucl. Phys. A **987**, 144–201 (2019). https://doi.org/10.1016/j.nuclphysa.2019.02.006
207. J. Chen, D. Keane, Y.G. Ma et al., Antinuclei in heavy-ion collisions. Phys. Rep. **760**, 1–39 (2018). https://doi.org/10.1016/j.physrep.2018.07.002
208. H. Sato, K. Yazaki, On the coalescence model for high energy nuclear reactions. Phys. Lett. B **98**, 153–157 (1981)
209. D. Oliinychenko, Overview of light nuclei production in relativistic heavy-ion collisions. Nucl. Phys. A **1005**, 121754 (2021)
210. T.H. Shao, J.H. Chen, Y.G. Ma et al., Production of light antinuclei in pp collisions by dynamical coalescence and their fluxes in cosmic rays near earth. Phys. Rev. C **105**, 065801 (2022). https://doi.org/10.1103/PhysRevC.105.065801
211. W. Zhao, K.J. Sun, C.M. Ko et al., Multiplicity scaling of light nuclei production in relativistic heavy-ion collisions. Phys. Lett. B **820**, 136571 (2021). https://doi.org/10.1016/j.physletb.2021.136571
212. X.Y. Zhao, Y.T. Feng, F.L. Shao et al., Production characteristics of light (anti-)nuclei from (anti-)nucleon coalescence in heavy ion collisions at energies employed at the RHIC beam energy scan. Phys. Rev. C **105**, 054908 (2022). https://doi.org/10.1103/PhysRevC.105.054908
213. K.J. Sun, C.M. Ko, F. Li et al., Enhanced yield ratio of light nuclei in heavy ion collisions with a first-order chiral phase transition. Eur. Phys. J. A **57**, 313 (2021). https://doi.org/10.1140/epja/s10050-021-00607-4
214. T.H. Shao, J.H. Chen, C.M. Ko et al., Yield ratio of hypertriton to light nuclei in heavy-ion collisions from $\sqrt{s_{NN}}$ = 4.9 GeV to 2.76 TeV. Chin. Phys. C **44**, 114001 (2020). https://doi.org/10.1088/1674-1137/abadf0
215. E. Shuryak, J.M. Torres-Rincon, Baryon clustering at the critical line and near the hypothetical critical point in heavy-ion collisions. Phys. Rev. C **100**, 024903 (2019). https://doi.org/10.1103/PhysRevC.100.024903
216. M.S. Abdallah et al., Light nuclei collectivity from $\sqrt{s_{NN}}$ = 3 GeV Au+Au collisions at RHIC. Phys. Lett. B **827**, 136941 (2022). https://doi.org/10.1016/j.physletb.2022.136941
217. J. Adam et al., Beam-energy dependence of the directed flow of deuterons in Au+ Au collisions. Phys. Rev. C **102**, 044906 (2020)
218. M.S. Abdallah et al., Flow and interferometry results from Au+Au collisions at $\sqrt{s_{NN}}$ = 4.5 GeV. Phys. Rev. C **103**, 034908 (2021)
219. B.I. Abelev et al., Observation of an antimatter hypernucleus. Science **328**, 58–62 (2010). https://doi.org/10.1126/science.1183980
220. Y.G. Ma, Hypernuclei as a laboratory to test hyperon-nucleon interactions. Nucl. Sci. Tech. **34**, 97 (2023). https://doi.org/10.1007/s41365-023-01248-6
221. J. Steinheimer, K. Gudima, A. Botvina et al., Hypernuclei, dibaryon and antinuclei production in high energy heavy ion collisions: thermal production versus coalescence. Phys. Lett. B **714**, 85–91 (2012). https://doi.org/10.1016/j.physletb.2012.06.069
222. J.H. Chen, X. Dong, Y.G. Ma et al., Measurements of the lightest hypernucleus ($^3_\Lambda$H): progress and perspective. Sci. Bull. **68**, 3252–3260 (2023). https://doi.org/10.1016/j.scib.2023.11.045
223. M. Abdallah et al., Measurements of $^3_\Lambda$H and $^4_\Lambda$H lifetimes and yields in Au+Au collisions in the high baryon density region. Phys. Rev. Lett. **128**, 202301 (2022). https://doi.org/10.1103/PhysRevLett.128.202301
224. S. Gläßel, V. Kireyeu, V. Voronyuk et al., Cluster and hypercluster production in relativistic heavy-ion collisions within the parton-hadron-quantum-molecular-dynamics approach. Phys. Rev. C **105**, 014908 (2022). https://doi.org/10.1103/PhysRevC.105.014908
225. B. Aboona et al., Observation of directed flow of hypernuclei $^3_\Lambda$H and $^4_\Lambda$H in $\sqrt{s_{NN}}$ =3 GeV Au+Au collisions at RHIC. Phys. Rev. Lett. **130**, 212301 (2023). https://doi.org/10.1103/PhysRevLett.130.212301
226. Y. Akiba et al., The hot QCD white paper: exploring the phases of QCD at RHIC and the LHC. Preprint at arXiv:1502.02730
227. B.I. Abelev et al., Centrality dependence of charged hadron and strange hadron elliptic flow from $\sqrt{s_{NN}}$ = 200 GeV Au + Au collisions. Phys. Rev. C **77**, 054901 (2008). https://doi.org/10.1103/PhysRevC.77.054901
228. X. Dong, Y.J. Lee, R. Rapp, Open heavy-flavor production in heavy-ion collisions. Ann. Rev. Nucl. Part. Sci. **69**, 417–445 (2019). https://doi.org/10.1146/annurev-nucl-101918-023806
229. M.I. Abdulhamid et al., Elliptic flow of heavy-flavor decay electrons in Au+Au collisions at $\sqrt{s_{NN}}$ = 27 and 54.4 GeV at RHIC.

Phys. Lett. B **844**, 138071 (2023). https://doi.org/10.1016/j.physletb.2023.138071
230. L. Adamczyk et al., Elliptic flow of electrons from heavy-flavor hadron decays in Au + Au collisions at $\sqrt{s_{\mathrm{NN}}} = 200$, 62.4, and 39 GeV. Phys. Rev. C **95**, 034907 (2017). https://doi.org/10.1103/PhysRevC.95.034907
231. M. He, R.J. Fries, R. Rapp, Modifications of heavy-flavor spectra in $\sqrt{s_{\mathrm{NN}}} = 62.4$ GeV Au-Au collisions. Phys. Rev. C **91**, 024904 (2015). https://doi.org/10.1103/PhysRevC.91.024904
232. T. Song, H. Berrehrah, D. Cabrera et al., Tomography of the quark-gluon-plasma by charm quarks. Phys. Rev. C **92**, 014910 (2015). https://doi.org/10.1103/PhysRevC.92.014910
233. T. Song, H. Berrehrah, J.M. Torres-Rincon et al., Single electrons from heavy-flavor mesons in relativistic heavy-ion collisions. Phys. Rev. C **96**, 014905 (2017). https://doi.org/10.1103/PhysRevC.96.014905
234. J. Adam et al., First measurement of Λ_c baryon production in Au+Au collisions at $\sqrt{s_{\mathrm{NN}}} = 200$ GeV. Phys. Rev. Lett. **124**, 172301 (2020). https://doi.org/10.1103/PhysRevLett.124.172301
235. M.C. Abreu et al., Evidence for deconfinement of quarks and gluons from the J/ψ suppression pattern measured in Pb + Pb collisions at the CERN SPS. Phys. Lett. B **477**, 28–36 (2000). https://doi.org/10.1016/S0370-2693(00)00237-9
236. L. Adamczyk et al., Energy dependence of J/ψ production in Au+Au collisions at $\sqrt{s_{\mathrm{NN}}} = 39$, 62.4 and 200 GeV. Phys. Lett. B **771**, 13–20 (2017). https://doi.org/10.1016/j.physletb.2017.04.078
237. J. Adam et al., Measurement of inclusive J/ψ suppression in Au+Au collisions at $\sqrt{s_{\mathrm{NN}}} = 200$ GeV through the dimuon channel at STAR. Phys. Lett. B **797**, 134917 (2019). https://doi.org/10.1016/j.physletb.2019.134917
238. B.B. Abelev et al., Centrality, rapidity and transverse momentum dependence of J/ψ suppression in Pb-Pb collisions at $\sqrt{s_{\mathrm{NN}}} =2.76$ TeV. Phys. Lett. B **734**, 314–327 (2014). https://doi.org/10.1016/j.physletb.2014.05.064
239. S. Acharya et al., Measurements of inclusive J/ψ production at midrapidity and forward rapidity in Pb-Pb collisions at $\sqrt{s_{\mathrm{NN}}} = 5.02$ TeV. Phys. Lett. B **849**, 138451 (2024). https://doi.org/10.1016/j.physletb.2024.138451
240. J. Zhao, P. Zhuang, Effects of cold and hot nuclear matter on J/ψ production at energies selected for the beam energy scan at the BNL Relativistic Heavy Ion Collider. Phys. Rev. C **105**, 064907 (2022). https://doi.org/10.1103/PhysRevC.105.064907
241. X. Zhao, R. Rapp, Charmonium in medium: from correlators to experiment. Phys. Rev. C **82**, 064905 (2010). https://doi.org/10.1103/PhysRevC.82.064905
242. T. Matsui, H. Satz, J/ψ suppression by quark-gluon plasma formation. Phys. Lett. B **178**, 416–422 (1986). https://doi.org/10.1016/0370-2693(86)91404-8
243. X.M. Xu, D. Kharzeev, H. Satz et al., J/ψ suppression in an equilibrating parton plasma. Phys. Rev. C **53**, 3051–3056 (1996). https://doi.org/10.1103/PhysRevC.53.3051
244. X. Yao, B. Müller, Quarkonium inside the quark-gluon plasma: diffusion, dissociation, recombination, and energy loss. Phys. Rev. D **100**, 014008 (2019). https://doi.org/10.1103/PhysRevD.100.014008
245. R. Sharma, I. Vitev, High transverse momentum quarkonium production and dissociation in heavy ion collisions. Phys. Rev. C **87**, 044905 (2013). https://doi.org/10.1103/PhysRevC.87.044905
246. L. Kluberg, 20 years of J/ψ suppression at the CERN SPS: results from experiments NA38, NA51 and NA50. Eur. Phys. J. C **43**, 145–156 (2005). https://doi.org/10.1140/epjc/s2005-02245-6
247. A. Adare et al., J/ψ production vs centrality, transverse momentum, and rapidity in Au+Au collisions at $\sqrt{s_{\mathrm{NN}}} = 200$ GeV. Phys. Rev. Lett. **98**, 232301 (2007). https://doi.org/10.1103/PhysRevLett.98.232301
248. P. Braun-Munzinger, J. Stachel, (Non)thermal aspects of charmonium production and a new look at J/ψ suppression. Phys. Lett. B **490**, 196–202 (2000). https://doi.org/10.1016/S0370-2693(00)00991-6
249. L. Grandchamp, R. Rapp, G.E. Brown, In medium effects on charmonium production in heavy ion collisions. Phys. Rev. Lett. **92**, 212301 (2004). https://doi.org/10.1103/PhysRevLett.92.212301
250. W. Zha, B. Huang, R. Ma et al., Systematic study of the experimental measurements on J/ψ cross sections and kinematic distributions in p+p collisions at different energies. Phys. Rev. C **93**, 024919 (2016). https://doi.org/10.1103/PhysRevC.93.024919
251. P.M. Hohler, R. Rapp, Is ρ-meson melting compatible with chiral restoration? Phys. Lett. B **731**, 103–109 (2014). https://doi.org/10.1016/j.physletb.2014.02.021
252. R. Rapp, J. Wambach, Low mass dileptons at the CERN SPS: Evidence for chiral restoration? Eur. Phys. J. A **6**, 415–420 (1999). https://doi.org/10.1007/s100500050364
253. R. Rapp, H. van Hees, Thermal dileptons as fireball thermometer and chronometer. Phys. Lett. B **753**, 586–590 (2016). https://doi.org/10.1016/j.physletb.2015.12.065
254. M.I. Abdulhamid, B.E. Aboona, J. Adam et al., Measurements of dielectron production in Au+Au collisions at $\sqrt{s_{\mathrm{NN}}} = 27$, 39, and 62.4 GeV from the STAR experiment. Phys. Rev. C **107**, L061901 (2023). https://doi.org/10.1103/PhysRevC.107.L061901
255. L. Adamczyk et al., Energy dependence of acceptance-corrected dielectron excess mass spectrum at mid-rapidity in Au+Au collisions at $\sqrt{s_{\mathrm{NN}}} = 19.6$ and 200 GeV. Phys. Lett. B **750**, 64–71 (2015). https://doi.org/10.1016/j.physletb.2015.08.044
256. H. van Hees, R. Rapp, Dilepton radiation at the CERN super proton synchrotron. Nucl. Phys. A **806**, 339–387 (2008). https://doi.org/10.1016/j.nuclphysa.2008.03.009
257. R. Arnaldi, K. Banicz, K. Borer et al., NA60 results on thermal dimuons. Eur. Phys. J. C **61**, 711–720 (2009). https://doi.org/10.1140/epjc/s10052-009-0878-5
258. A. Bazavov, T. Bhattacharya, M.I. Buchoff et al., Chiral transition and $U(1)_A$ symmetry restoration from lattice QCD using domain wall fermions. Phys. Rev. D **86**, 094503 (2012). https://doi.org/10.1103/PhysRevD.86.094503
259. J. Adamczewski-Musch et al., Probing dense baryon-rich matter with virtual photons. Nat. Phys. **15**, 1040–1045 (2019). https://doi.org/10.1038/s41567-019-0583-8
260. L. Adamczyk, J.K. Adkins, G. Agakishiev et al., Measurements of dielectron production in Au+Au collisions at $\sqrt{s_{\mathrm{NN}}} = 200$ GeV from the STAR experiment. Phys. Rev. C **92**, 024912 (2015). https://doi.org/10.1103/PhysRevC.92.024912
261. R. Arnaldi et al., Evidence for the production of thermal-like muon pairs with masses above 1 GeV/c^2 in 158 A GeV indium-indium collisions. Eur. Phys. J. C **59**, 607–623 (2009). https://doi.org/10.1140/epjc/s10052-008-0857-2
262. A. Bazavov et al., Chiral crossover in QCD at zero and non-zero chemical potentials. Phys. Lett. B **795**, 15–21 (2019). https://doi.org/10.1016/j.physletb.2019.05.013
263. STAR Collaboration, Temperature measurement of quark-gluon plasma at different stages. Preprint at arXiv:2402.01998
264. C.A. Bertulani, S.R. Klein, J. Nystrand, Physics of ultra-peripheral nuclear collisions. Ann. Rev. Nucl. Part. Sci. **55**, 271–310 (2005). https://doi.org/10.1146/annurev.nucl.55.090704.151526
265. G. Baur, K. Hencken, D. Trautmann, Electron-positron pair production in relativistic heavy ion collisions. Phys. Rep. **453**, 1–27 (2007). https://doi.org/10.1016/j.physrep.2007.09.002

266. J. Adam, L. Adamczyk, J.R. Adams et al., Low-$p_T e^+e^-$ pair production in Au+Au collisions at $\sqrt{s_{\mathrm{NN}}} = 200$ GeV and U+U collisions at $\sqrt{s_{\mathrm{NN}}} = 193$ GeV at STAR. Phys. Rev. Lett. **121**, 132301 (2018). https://doi.org/10.1103/PhysRevLett.121.132301
267. M. Aaboud, G. Aad, B. Abbott et al., Observation of centrality-dependent acoplanarity for muon pairs produced via two-photon scattering in Pb+Pb collisions at $\sqrt{s_{\mathrm{NN}}} = 5.02$ TeV with the ATLAS detector. Phys. Rev. Lett. **121**, 212301 (2018). https://doi.org/10.1103/PhysRevLett.121.212301
268. W. Zha, L. Ruan, Z. Tang et al., Coherent photo-produced J/ψ and dielectron yields in isobaric collisions. Phys. Lett. B **789**, 238–242 (2019). https://doi.org/10.1016/j.physletb.2018.12.041
269. M. Kłusek-Gawenda, A. Szczurek, Photoproduction of J/ψ mesons in peripheral and semicentral heavy ion collisions. Phys. Rev. C **93**, 044912 (2016). https://doi.org/10.1103/PhysRevC.93.044912
270. S.R. Klein, Two-photon production of dilepton pairs in peripheral heavy ion collisions. Phys. Rev. C **97**, 054903 (2018). https://doi.org/10.1103/PhysRevC.97.054903
271. W.M. Zha, J.D. Brandenburg, Z.B. Tang et al., Initial transverse-momentum broadening of Breit-Wheeler process in relativistic heavy-ion collisions. Phys. Lett. B **800**, 135089 (2020). https://doi.org/10.1016/j.physletb.2019.135089
272. S. Klein, A.H. Mueller, B.W. Xiao et al., Lepton pair production through two photon process in heavy ion collisions. Phys. Rev. D **102**, 094013 (2020). https://doi.org/10.1103/PhysRevD.102.094013
273. M. Kłusek-Gawenda, W. Schäfer, A. Szczurek, Centrality dependence of dilepton production via $\gamma\gamma$ processes from Wigner distributions of photons in nuclei. Phys. Lett. B **814**, 136114 (2021). https://doi.org/10.1016/j.physletb.2021.136114
274. R.J. Wang, S. Pu, Q. Wang, Lepton pair production in ultraperipheral collisions. Phys. Rev. D **104**, 056011 (2021). https://doi.org/10.1103/PhysRevD.104.056011
275. C. Li, J. Zhou, Y.J. Zhou, Impact parameter dependence of the azimuthal asymmetry in lepton pair production in heavy ion collisions. Phys. Rev. D **101**, 034015 (2020). https://doi.org/10.1103/PhysRevD.101.034015
276. A.M. Sirunyan, A. Tumasyan, W. Adam et al., Observation of forward neutron multiplicity dependence of dimuon acoplanarity in ultraperipheral Pb-Pb collisions at $\sqrt{s_{\mathrm{NN}}} = 5.02$ TeV. Phys. Rev. Lett. **127**, 122001 (2021). https://doi.org/10.1103/PhysRevLett.127.122001
277. M. Abdallah, J. Adam, L. Adamczyk et al., Measurement of the sixth-order cumulant of net-proton multiplicity distributions in Au+Au collisions at $\sqrt{s_{\mathrm{NN}}} = 27$, 54.4, and 200 GeV at RHIC. Phys. Rev. Lett. **127**, 262301 (2021). https://doi.org/10.1103/PhysRevLett.127.262301
278. Y.J. Yuan, D.Q. Gao, L.Z. Ma et al., Present status of HIRFL complex in Lanzhou. J. Phys. Conf. Ser. **1401**, 012003 (2020). https://doi.org/10.1088/1742-6596/1401/1/012003
279. H.W. Zhao, H.S. Xu, G.Q. Xiao et al., Huizhou accelerator complex facility and its future development. Sci. Sin. Phys. Mech. Astron. **50**, 112006 (2020). https://doi.org/10.1360/SSPMA-2020-0248
280. D. Guo, X.H. He, P.C. Li et al., Studies of nuclear equation of state with the HIRFL-CSR external-target experiment. Euro. Phys. J. A **60**, 36 (2024). https://doi.org/10.1140/epja/s10050-024-01245-2
281. L.M. Lyu, H. Yi, Z.G. Xiao et al., Conceptual design of the HIRFL-CSR external-target experiment. Sci. China Phys. Mech. Astron. **60**, 012021 (2017). https://doi.org/10.1007/s11433-016-0342-x
282. Z. Ye, H. Zhang, Y. Zhang et al., New Chinese facilities for short-range correlation physics. Eur. Phys. J. A **60**, 126 (2024). https://doi.org/10.1140/epja/s10050-024-01343-1
283. S. Chatrchyan, V. Khachatryan, A.M. Sirunyan et al., Observation of long-range near-side angular correlations in proton-lead collisions at the LHC. Phys. Lett. B **718**, 795–814 (2013). https://doi.org/10.1016/j.physletb.2012.11.025
284. C. Hadjidakis, D. Kikoła, J.P. Lansberg et al., A fixed-target programme at the LHC: physics case and projected performances for heavy-ion, hadron, spin and astroparticle studies. Phys. Rep. **911**, 1–83 (2021). https://doi.org/10.1016/j.physrep.2021.01.002
285. T. Ablyazimov, A. Abuhoza, R. P. Adak et al., Challenges in QCD matter physics—the scientific programme of the compressed baryonic matter experiment at FAIR. Eur. Phys. J. A **53**, 60 (2017). https://doi.org/10.1140/epja/i2017-12248-y
286. A. Kisiel, Status of the MPD experiment at JINR. J. Phys. Conf. Ser. **1602**, 012021 (2020). https://doi.org/10.1088/1742-6596/1602/1/012021
287. I. Deppner, N. Herrmann, D. Gonzalez-Diaz et al., The CBM time-of-flight wall. Nucl. Instrum. Meth. A **661**, S121–S124 (2012). https://doi.org/10.1016/j.nima.2010.09.165
288. W.Q. Shen, High-energy nuclear physics in China. J. Phys. G **34**, S173–S179 (2007). https://doi.org/10.1088/0954-3899/34/8/S01